VIETNAM NATIONAL UNIVERSITY, HANOI
UNIVERSITY OF ENGINEERING AND TECHNOLOGY

PHAN HOANG ANH

RESEARCH AND DEVELOPMENT OF LAB ON A CHIP (LOC) DEVICE TO DETECT AND QUANTIFY LUNG CANCER CELLS

PhD DISSERTATION IN ELECTRONIC ENGINEERING

HANOI – 2025

VIETNAM NATIONAL UNIVERSITY, HANOI

UNIVERSITY OF ENGINEERING AND TECHNOLOGY

PHAN HOANG ANH

RESEARCH AND DEVELOPMENT OF LAB ON A CHIP (LOC) DEVICE TO DETECT AND QUANTIFY LUNG CANCER CELLS

PhD DISSERTATION IN ELECTRONIC ENGINEERING

MAJOR : ELECTRONIC ENGINEERING

MAJOR CODE : 9510302.01

SUPERVISOR : ASSOC. PROF. DR. NGUYEN HOANG HAI

CO-SUPERVISOR : PROF. DR. CHU DUC TRINH

HANOI – 2025

Declaration of Authorship

I, **PHAN HOANG ANH**, hereby declare that this thesis titled **"Research and Development of Lab on a Chip (LoC) Device to Detect and Quantify Lung Cancer Cells"** and the work presented in it are my own. I confirm that:

- This work was done wholly or mainly while in candidature for a PhD degree at Vietnam National University, University of Engineering and Technology.
- Where I have consulted the published work of others, this is always clearly attributed.
- Where I have quoted from the work of others, the source is always given. With the exception of such quotations, this thesis is entirely my own work.
- I have acknowledged all main sources of help.
- Where the thesis is based on work done by myself jointly with others, I have made clear exactly what was done by others and what I have contributed myself.

Date: _____ **Signature:** _____

PHAN HOANG ANH

Acknowledgements

First and foremost, I would like to express my sincere gratitude to my supervisors, Assoc. Prof. Dr. Nguyen Hoang Hai and Prof. Dr. Chu Duc Trinh, for their invaluable guidance, continuous support, and patience throughout my PhD research. Their immense knowledge and extensive experience have encouraged me throughout my academic research and daily life.

I would like to extend my special thanks to Assoc. Prof. Dr. Bui Thanh Tung, Assoc. Prof. Dr. Do Quang Loc, and Prof. Dr. Chun-Ping Jen for their expert advice, insightful discussions, and critical suggestions which greatly improved the quality of this thesis.

I would also like to thank all members of the laboratory for their help and support during my research. The friendly and collaborative environment has been essential for the completion of this work.

I am deeply grateful to Vietnam National University, Hanoi and University of Engineering and Technology for providing me with the opportunity and resources to pursue my doctoral studies.

Special thanks to my family for their unconditional love, support, and encouragement throughout my studies. Without their understanding and patience, this work would not have been possible.

Finally, I would like to acknowledge the financial support from the Vietnam Ministry of Science and Technology under Grant ĐTĐL.CN-40/23 that made this research possible.

Hanoi, 2025

PHAN HOANG ANH

Abstract

Cancer remains a leading cause of mortality worldwide, with lung cancer accounting for the highest proportion of cancer-related deaths. Early detection of circulating tumor cells (CTCs) is crucial for timely diagnosis, prognosis assessment, and treatment monitoring. However, CTCs are extremely rare in peripheral blood, with approximately one CTC per 10^6–10^7 white blood cells, making their isolation and detection technically challenging. This thesis presents the development of an integrated Lab-on-a-Chip (LoC) platform for the isolation, detection, and counting of A549 lung cancer cells using a combination of magnetic separation, impedance measurement, and machine learning techniques.

The research objectives are: (1) to investigate and develop an integrated Lab-on-a-Chip platform by designing and fabricating a microfluidic device with optimized magnetic separation structures, and CTC detection and enumeration system; and (2) to experimentally validate the proposed system and systematically evaluate its performance in terms of capture efficiency, detection accuracy, and robustness under relevant operating conditions.

The proposed system employs superparamagnetic Fe_3O_4 nanoparticles functionalized with EpCAM-specific aptamers for selective binding to A549 cancer cells. The microfluidic chip features a serpentine channel design with optimized trap regions that generate high magnetic field gradients under an external permanent magnet. An impedance measurement circuit based on lock-in amplification technique was developed to capture cellular impedance signals. Signal processing algorithms utilizing peak detection and machine learning models were implemented for automated cell classification and counting.

Simulation results demonstrate capture efficiencies of 80%, 94%, and 100% for magnetic bead sizes of 1.36 μm, 3.00 μm, and 4.50 μm, respectively. The fabricated microfluidic chip with channel dimensions of 30 μm enables single-cell flow alignment for precise impedance measurement. The impedance measurement system successfully distinguishes cell signals characterized by bipolar peaks from background noise. Machine learning models, including IsolationForest and OneClassSVM, achieved classification accuracy exceeding 88% for cell signal recognition.

This thesis contributes to the field of cancer diagnostics by presenting a compact, cost-effective, and automated platform for CTC detection. The integration of magnetic separation, impedance sensing, and intelligent signal processing on a single microfluidic chip provides a promising approach for point-of-care cancer screening applications. Future

work will focus on clinical validation with patient blood samples and further optimization of system sensitivity and specificity.

Contents

List of Figures

List of Tables

List of Abbreviations

Abbreviation	Meaning
AC	Alternating Current
ADC	Analog-to-Digital Converter
Cks	Cytokeratins
CNN	Convolutional Neural Network
CT	Computed Tomography
CTC	Circulating Tumor Cell
ctDNA	Circulating Tumor DNA
CTM	Circulating Tumor Microemboli
DAC	Digital-to-Analog Conversion
DC	Direct Current
DEP	Dielectrophoresis
DI	Deionized
EMI	Electromagnetic Interference
EP	End Point
EpCAM	Epithelial Cellular Adhesion Molecule
ESPR1	Epithelial Splicing Regulator 1
FAST	Fiber-optic Array Scanning Technology
FTW	Frequency Control Words
IFC	Integrated Fluidic Circuit
ISET	Isolation by Size of Epithelial Tumor Cells
MACS	Magnetic-Activated Cell Sorting
MB	Magnetic Bead
MCU	Microcontroller Unit
MRI	Magnetic Resonance Imaging
NMS	Non-Maximum Suppression
NP	Negative Peak
NSCLC	Non-Small Cell Lung Cancer
PDMS	Polydimethylsiloxane

Continued on next page

Table 1 – *Continued from previous page*

Abbreviation	**Meaning**
PP	Positive Peak
RBC	Red Blood Cell
SCLC	Small Cell Lung Cancer
SP	Start Point
WBC	White Blood Cell
ZO	Zonula Occludens

Dissertation Introduction

Background and context of the research

Cancer remains a leading cause of mortality worldwide, with metastasis accounting for the majority of cancer-related deaths. Circulating Tumor Cells (CTCs), which detach from primary tumors and enter the bloodstream, are key drivers of metastasis. The detection and isolation of CTCs offer significant potential for early diagnosis, prognosis, and monitoring of cancer treatment. However, CTCs are extremely rare in peripheral blood, making their isolation a significant technical challenge. Recent advancements in microfluidic technology provide promising solutions for the efficient and label-free separation of CTCs.

Objective and significance of the research

The primary objective of this research is to develop and optimize a microfluidic system for the high-efficiency isolation and analysis of CTCs. This study aims to address the limitations of current isolation methods by integrating novel separation techniques. The significance of this research lies in its potential to provide a reliable, low-cost, and non-invasive tool for liquid biopsy, ultimately contributing to better patient outcomes through personalized medicine.

Main contributions of the dissertation

The main scientific and technological contributions of this dissertation can be summarized as follows:

1. Integration and successful fabrication of a multifunctional microfluidic Lab-on-a-Chip system capable of detecting and counting lung cancer cells. The chip combines several functional modules on a single platform, including magnetically assisted and inertial microfluidic separation, single-cell encapsulation in droplets, impedance-based cell counting, and machine-learning-based signal processing for automatic classification of measurement signals.

2. Proposal and validation of new methods for cell detection, classification, and separation that exploit electromagnetic techniques and image processing in combination with advanced machine learning models. These methods leverage magnetic forces, non-uniform electric fields, impedance cytometry, and deep-learning-based image analysis to enhance the accuracy and robustness of cancer cell isolation and analysis.

Scientific and practical significance

Scientifically, this dissertation contributes to the understanding of microfluidic dynamics and cell manipulation techniques, specifically focusing on the interaction between physical forces and biological cells. Practically, the developed system offers a tangible device that can be deployed in clinical settings for routine cancer screening and monitoring, bridging the gap between engineering innovation and medical application.

Methods and scope of the study

This study employs a combination of numerical simulation and experimental validation. The scope includes the design and fabrication of microfluidic devices, characterization of fluid flow and particle behavior, and testing with biological samples including cancer cell lines and blood samples. The research focuses on specific isolation mechanisms such as dielectrophoresis (DEP) or magnetic-activated cell sorting (MACS) within microfluidic channels.

Overview of the dissertation structure

The dissertation is organized as follows:

- **Chapter 1** provides an overview of cancer metastasis, CTCs, and existing isolation technologies.
- **Chapter 2** details the theoretical background and simulation of the proposed microfluidic methods.
- **Chapter 3** describes the material preparation, experimental setup, and fabrication processes.
- **Chapter 4** presents the results and discussion of the experimental findings.
- **Conclusion** summarizes the key contributions and suggests future research directions.

Chapter 1

OVERVIEW OF THE RESEARCH

1.1 Overview of the cancer situation

Cancer constitutes the second leading cause of death globally, following cardiovascular disease. It represents a malignant cellular disorder characterized by unlimited proliferation that circumvents the body's regulatory mechanisms. The invasive, recurrent, and metastatic nature of cancer renders complete treatment exceedingly challenging. According to the Vietnamese Ministry of Health, only 185 out of 204 countries have reported cancer incidence statistics to GLOBOCAN. Based on GLOBOCAN statistics for 2020, both cancer incidence and mortality rates worldwide demonstrate an upward trend. In Vietnam, an estimated 182,563 new cases and 122,690 cancer-related deaths were recorded (Figure 1.1). For every 100,000 individuals, 159 receive a new cancer diagnosis while 106 succumb to the disease. Vietnam ranks 91st out of 185 countries in terms of incidence rate and 50th in terms of mortality rate per 100,000 population [1]. The corresponding rankings for 2018 were 99th and 56th, respectively, out of 185 countries. These data indicate that both new cases and cancer-related deaths in Vietnam are increasing rapidly. This trend parallels that observed in numerous countries worldwide, including developed nations such as the United Kingdom, France, Italy, Japan, South Korea, Thailand, and the United States. However, cancer mortality rates in these developed countries are declining. In Vietnam, the most prevalent cancers among men include liver, lung, stomach, colorectal, and prostate cancer, accounting for approximately 65.8% of all malignancies. Among women, the most common cancers comprise breast, lung, colorectal, stomach, and liver cancer, representing approximately 59.4% of all cases. Cancers affecting both genders predominantly include liver, lung, breast, stomach, and colorectal malignancies [2]. Although lung and bronchial cancer ranks second in terms of new cases, it accounts for the highest proportion of cancer-related deaths in both genders, representing approximately 20% of all cases [1]. Typically, lung tumors measure 2–10 cm in diameter or larger at the time of detection, substantially reducing treatment efficacy. Consequently, recent re-

search endeavors have focused on developing molecular diagnostics for early-stage cancer detection, prior to metastasis. Earlier detection of cancer in general, and lung cancer in particular, enables clinicians to implement more appropriate and effective treatment strategies.

Metastasis represents the primary cause of tumor-related mortality, and the dissemination of tumor cells through the circulatory system constitutes a critical step in the metastatic cascade. Therefore, early detection and analysis of circulating tumor cells (CTCs) proves crucial for early diagnosis, prognosis determination, and facilitation of timely treatment interventions [3]. Accurate and reliable methodologies for CTC isolation and detection represent essential factors for obtaining clinical information regarding cancer progression. Over the past two decades, microfluidic technology has demonstrated substantial potential for isolating and detecting CTCs from blood specimens. This study developed advanced microfluidic technologies to establish a Lab-on-a-Chip device platform for CTC isolation and detection based on diverse biological and physical principles [4].

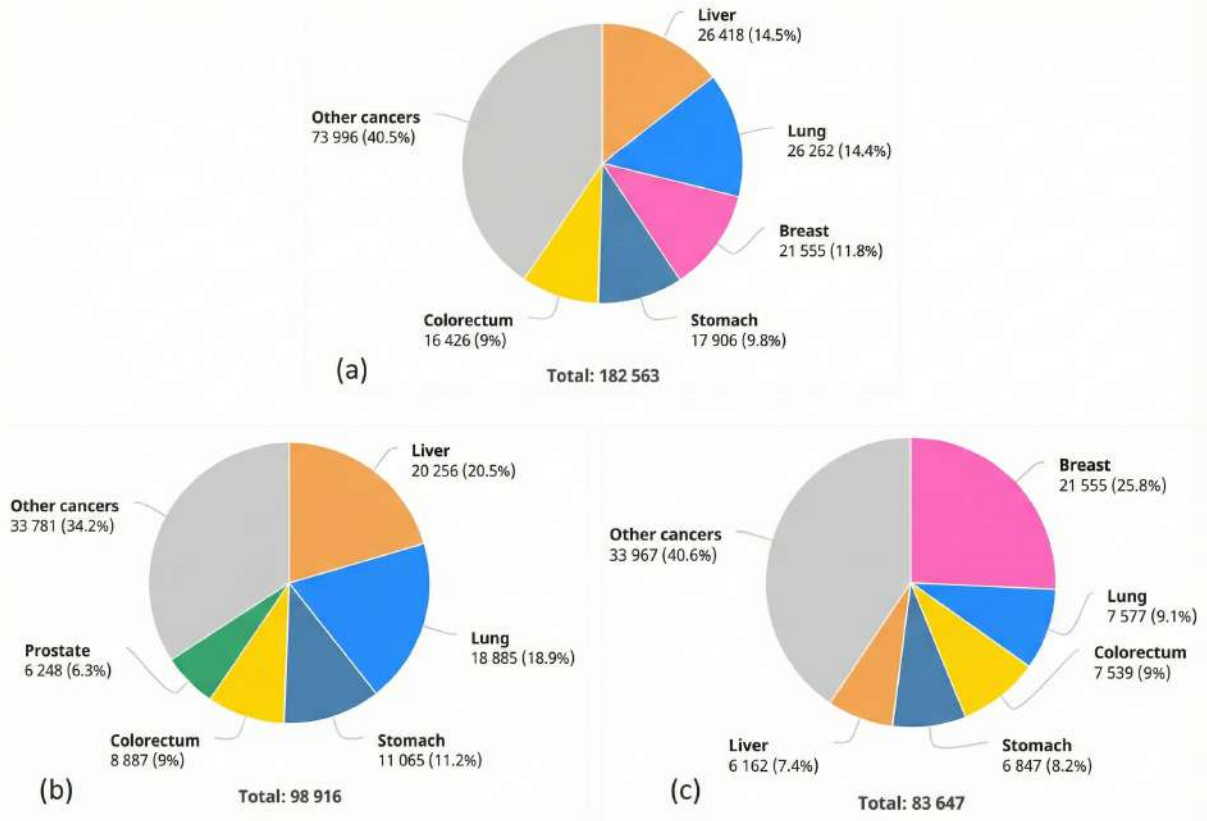

Figure 1.1: Statistical results according to GLOBOCAN 2020 on the cancer situation in Vietnam: (a) Number of new cases in both genders; (b) Number of new cases in males; (c) Number of new cases in females [5].

Over 90% of cancer-related deaths are attributable to metastasis, a complex multistep process. Initially, tumor cells escape from the primary tumor, subsequently invading blood vessels, traveling through the bloodstream, extravasating at a distant site, and ul-

timately establishing a secondary tumor. These mobile tumor cells can infiltrate adjacent blood vessels and circulate throughout the body, hence their designation as circulating tumor cells (CTCs). CTCs that survive in circulation attach to blood vessel walls and extravasate to distant sites to form secondary tumors. Some metastatic tumor cells enter a dormant state, while others disseminate to additional sites. This behavior depends on the metastatic microenvironment, wherein metastatic cells may exhibit expression patterns distinct from those of primary tumor cells. Currently, cancer incidence rates continue to rise, and the majority of patients presenting for cancer diagnosis are often in advanced stages. Therefore, screening, surveillance, and early diagnosis assume paramount importance in patient treatment. Earlier diagnosis correlates with enhanced treatment efficacy and increased probability of cure.

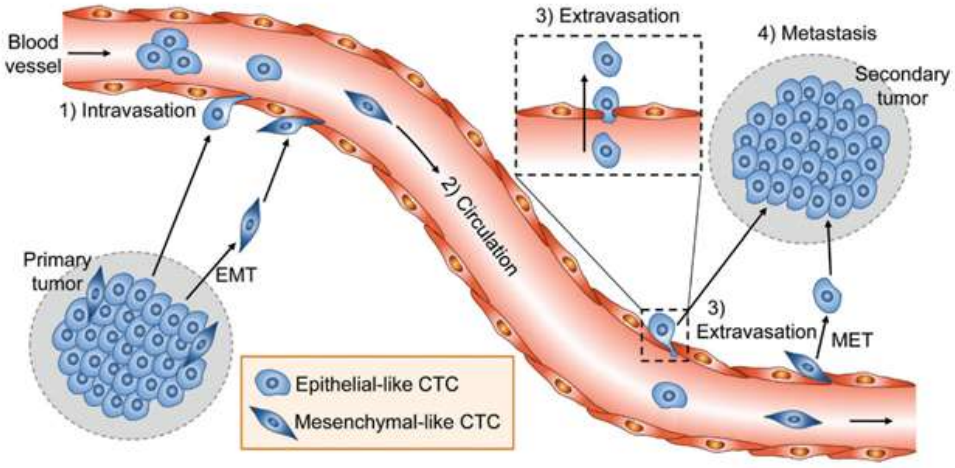

Figure 1.2: Diagram illustrating tumor metastasis via CTCs/CTM [3].

Figure 1.2 illustrates the metastatic process through circulating tumor cells (CTCs). During metastasis, tumor cells detach from the primary tumor and enter the circulatory system, thereby becoming circulating tumor cells. This process involves the epithelial-to-mesenchymal transition and marks the initial stage of metastasis [6]. During circulation in the bloodstream, the majority of CTCs undergo programmed cell death (apoptosis) and necrosis, releasing debris, cell fragments, and intracellular substances including circulating tumor microemboli (CTM) and circulating tumor DNA (ctDNA) [6]. In addition to CTCs, CTMs are also present in the blood, although their occurrence in the circulatory system is even rarer than that of CTCs. CTCs can detach from CTMs when subjected to shear forces or frequent collisions within blood flow; conversely, they can attach to tumors or other blood cells upon collision due to cellular adhesion. The microenvironment established within CTMs is unique, affording protection to the enclosed tumor cells from damage. Consequently, CTMs are considered more dangerous than individual CTCs because tumor cells can dissociate and proliferate within blood vessels and may cause vascular rupture. In contrast, individual CTCs typically must extravasate from blood

vessels to proliferate and form metastases.

The discovery of circulating tumor cells was first reported circa 1869. However, research on CTCs remained limited because circulating tumor cells are exceedingly rare in blood, with approximately one CTC per 10^6–10^7 white blood cells in the peripheral blood of cancer patients, rendering enrichment and detection challenging. Recently, with the rapid advancement of science and technology, CTC research has attracted considerable attention from research groups worldwide. In studies of CTC detection and analysis devices, the isolation and separation of CTCs to enhance their concentration plays a crucial role in improving detection and measurement performance in patient samples. This approach significantly impacts diagnostic accuracy and treatment efficacy while providing a minimally invasive method for determining patient cancer status. Two principal types of lung cancer exist: non-small cell lung cancer (NSCLC) and small cell lung cancer (SCLC) [7]. NSCLC accounts for the majority of lung cancer cases and progresses more slowly. Early detection combined with immediate treatment offers substantial potential for successful recovery. Treatment may incorporate various modalities including surgery, radiation therapy, and chemotherapy. SCLC represents a rapidly progressing form of lung cancer that frequently disseminates rapidly to other body regions through the bloodstream. SCLC is often diagnosed at an advanced stage, with chemotherapy constituting the typical treatment approach [8].

1.2 Microfluidic technology for circulating tumor cell testing

Currently, cancer diagnosis relies on a variety of methodologies. At the clinical diagnosis stage, clinicians often consider the patient's family history, personal history, medical history, and symptoms indicative of specific cancer risks before conducting clinical examinations. Clinical examination can detect tumors through visual inspection and palpation, assess tumor size and characteristics (hardness, mobility, ulceration), evaluate lymph node status, and identify other relevant phenomena. Additionally, ancillary examinations provide more detailed information regarding the patient's condition. Common clinical investigations include hematological tests such as complete blood counts and bone marrow examinations; utilization of tumor markers for screening, monitoring, treatment efficacy evaluation, recurrence detection, and prognostication; endoscopy; and imaging techniques including X-ray, ultrasound, computed tomography (CT), and magnetic resonance imaging (MRI), which can detect both superficial masses (breast, thyroid, etc.) and deep-seated masses (liver, pancreas, pelvis, etc.) [9]. Furthermore, cytological diagnosis employing cell block techniques and biopsy offers several advantages over histopathological diagnosis, including rapid results, procedural simplicity, reduced cost, fewer complications,

and compatibility with immunohistochemical staining [10]. Moreover, histopathological diagnosis is regarded as the "gold standard" for confirming cancer diagnosis using specimen collection methods such as needle biopsy, punch biopsy, endoscopic biopsy, and open surgery. Histopathological analysis enables determination of tumor nature (benign or malignant), cancer type identification, histological classification, grading, and supports additional tests including immunohistochemistry and molecular biological diagnosis [11]. However, biopsy procedures may encounter complications such as bleeding, blood clots, pain or discomfort, infection, and pneumonia.

Concurrent with advances in microfabrication technology and the integration of physical methods on microfluidic platforms, current research predominantly focuses on complete testing chips (lab-on-a-chip) applied in point-of-care diagnostics. This integration confers benefits including size reduction, cost reduction, and minimization of required chemicals. Furthermore, the microfluidic platform facilitates the integration of auxiliary components and processes such as sample pretreatment (e.g., cell lysis or cell staining) directly on the microfluidic chip. Simultaneously, the chips employed in these applications can be disposable, providing a sterile environment that eliminates the risk of cross-contamination and hazards associated with handling biological samples. The majority of methods for detecting circulating tumor cells in blood are performed using commercial equipment systems such as flow cytometers, the CellSearch system, high-quality fluorescence scanning microscopes, fiber-optic array scanning technology (FAST), isolation by size of epithelial tumor cells (ISET) [12], and laser scanning cell analyzers [13].

The integration of cell-based diagnostic systems with microfluidic platforms not only offers advantages in terms of testing time and cost but also creates new opportunities for biomedical research. The development of microfluidic flow cytometry devices [14] can disseminate this technology to laboratories, facilitating biological research including cancer studies, drug development, and genetic research. Additionally, these microfluidic devices reduce testing time for patients, minimize required sample volumes, and decrease the economic burden of testing [11].

Over the past two decades, microfluidic technologies for CTC isolation have garnered significant attention due to their integration into microfluidic structures that isolate CTCs based on various physical methods [10]. By exploiting biological differences between CTCs and normal cells, microfluidic platforms enable precise isolation of CTCs from millions of background cells. Furthermore, the low shear stress exerted on CTCs in microchannels due to laminar flow within the microfluidic structure permits intact CTCs to be isolated for subsequent testing and culture [9], [15]. Multi-step isolation processes, incorporating biological and physical isolation principles along with advanced nanotechnologies, can be integrated onto chips within microfluidic platforms to achieve higher CTC isolation efficiency [4], [16]. Microfluidic devices can also be mass-produced, enabling cost-effectiveness.

Microfluidic systems offer several advantages over alternative methods and devices due to their simplicity and rapid analysis time. Furthermore, these systems permit reduced blood sample volumes and whole blood analysis without prior sample preparation. Additionally, CTC isolation and detection based on microfluidic platforms presents several advantages:

1. The patient's peripheral blood can be directly introduced onto the microfluidic chip without prior dilution, labeling, fixation, or other processing steps;
2. The cost of microfluidic chips is considered relatively low;
3. Sensitivity is relatively high (approximately 70% of CTCs can be captured at a level of 3–5 cells/mL of blood);
4. CTCs isolated and enriched by microfluidic chips can be utilized for subsequent phenotyping and molecular analysis [9].

1.3 Research on the isolation and separation of CTCs

The majority of cancers originate from epithelial cells. Methods for enriching epithelial-derived CTCs from blood samples are based on this histological origin. For instance, blood cells belong to the connective tissue type. Connective tissue and epithelial cells differ not only in size, shape, and nuclear characteristics but also express different surface receptors, such as the absence of CD45—a marker of all leukocyte types—in epithelial cells [12]. Conversely, numerous markers typical of epithelial cells are absent in blood cells, including: EpCAM (epithelial cellular adhesion molecule), E-cadherin, Cytokeratin (Cks), Zonula occludens (ZO), and ESPR1 (Epithelial splicing regulator 1) [7], [16], [17], [18], [19]... Additionally, evaluation of receptor expression levels on the cell surface enables distinction between normal and abnormal epithelial cells. For example, EpCAM is expressed at low levels in healthy epithelial cells but is overexpressed in certain cancer cell types [3]; alternatively, increased N-Cadherin and decreased E-Cadherin serve as markers for identifying cancer cells and CTCs in blood [6] because E-Cadherin is highly expressed in epithelial cells as it participates in maintaining cell-cell junctions, whereas in cancer cells, this protein is poorly expressed; N-Cadherin is highly expressed in cells undergoing epithelial-mesenchymal transition, whereas these proteins are not abundant in normal cells. Numerous commercial devices have been continuously researched and developed in recent years for isolating and detecting CTCs from blood.

Several commercial devices utilized for CTC isolation are presented in Figure 1.3. MACS® (Miltenyi Biotec) performs cell sorting using magnetic-activated cell sorting (MACS) [20], a common method for isolating CTCs from blood employing 50 nm diameter magnetic beads. Anti-EpCAM-coated magnetic beads are utilized to directly

isolate CTCs as a positive selection method, while Anti-CD45-coated magnetic beads are employed to reduce the number of normal blood cells as a negative selection method [21]. Polymer-coated columns are utilized to generate a large gradient magnetic field from an external magnetic source. In positive isolation, CTCs are first captured on the column and subsequently retrieved by removing the external magnetic source. Conversely, in negative isolation, CTCs are enriched while normal blood cells are retained by the functionalized columns. Additional commercial products for CTC separation using magnetic methods include Dynabeads™ (ThermoFisher Scientific) [21]. Dynabeads represents an immunomagnetic capture method using magnetic beads (diameter 2.8 μm, M280-Dynabeads; or diameter 4.5 μm, M450-Dynabeads). Dynabeads can be coated with Anti-EpCAM and Anti-CD45, available for positive selection (Dynabeads™ Epithelial Enrich) and negative selection (Dynabeads™ CD45), respectively [21], [22].

Due to its simple structure and operational process, the utilization of microfluidic structures represents the most convenient approach for capturing single cells. C1 (Fluidigm) constitutes an automated system for capturing single cells into 800 individual microchambers within an integrated fluidic circuit (IFC). Although the system requires sample preparation procedures to purify target cells and cannot individually separate captured single cells, these captured single cells can be automatically stained within the IFC for viability monitoring, surface labeling, or reporter gene analysis under a microscope. Furthermore, captured cells can be automatically processed to prepare single-cell samples, which can be collected for subsequent qPCR or sequencing analysis.

Dielectrophoresis (DEP) is a liquid biopsy separation method based on the differential movement of particles with different polarities under a non-uniform electric field. Microchips employing DEP technology have been developed to isolate and capture CTCs through multiple integrated electrodes, generating a non-uniform alternating electric field within liquid structures. The Apostream™ system from ApoCell [23] represents the first commercial product utilizing DEP forces to separate CTCs and leukocytes based on their conductivity differences [24]. However, this device requires an initial enrichment step. The reported capture rate exceeds 70%, viability exceeds 97%, and processing time is 1 hour for a 10 mL blood sample; however, the obtained purity is less than 1% [25].

DEPArray (Menarini-Silicon Biosystems) is a commercial product that traps single cells into 16,000 individual electrode cages integrated into the structure of a microfluidic device based on the DEP phenomenon. After identifying trapped single cells using integrated fluorescence microscopy, the cells of interest are sequentially transferred to adjacent chambers by electric field control, encapsulated into a single droplet, and finally released into a receiving chamber as one or more cells. Similar to microfluidic devices, the DEPArray system also requires a pre-enrichment process to isolate target cells from a heterogeneous cell mixture. For example, prior to analyzing single CTCs with DEPArray, some studies have utilized the CellSearch system to enrich CTCs from blood to identify

mutations through sequencing based on patient samples from breast cancer patients [12], [26].

Figure 1.3: Selected commercial products for microfluidic systems in CTC isolation and detection from blood: (a) MACS® (Miltenyi Biotec) [20]; (b) Dynabeads™ (ThermoFisher Scientific); (c) C1 (Fluidigm) [27]; (d) DEPArray system (Menarini-Silicon Biosystems) [23] and corresponding microfluidic device.

In practice, numerous studies have integrated the principle of dielectrophoresis with microfluidic structures to isolate CTCs from mixtures containing normal cells. The research group of Chun-Ping Jen and colleagues developed a system capable of efficiently separating cervical carcinoma cells (HeLa) from peripheral blood samples. The circular microelectrodes generate a stepped electric field by switching the electric field between adjacent electrode pairs using a control relay. The magnitude of the dielectrophoretic force (DEP) acting on HeLa cells is approximately seven times greater than that on red blood cells (RBCs) under a specific electric field distribution in a sucrose medium, enabling the separation of HeLa cells from normal blood cells. Consequently, HeLa cells are concentrated at the central microelectrode and isolated from the blood sample. The experimental results demonstrate the feasibility of isolating HeLa cells from blood samples [28], [29]. Additionally, the research group proposed a microfluidic structure employing the DEP principle to separate HT29 cells from blood mixtures.

Figure 1.4 presents a block diagram of a CTC cell separation system utilizing magnetic nanoparticles and biological antibodies combined with microfluidic technology. The biochip structure comprises two parts: the first part separates white blood cells (WBCs) from the solution using a combination of magnetic nanoparticles and antibodies that specifically recognize WBCs (CD45 antibodies). The second part of this structure is the GASI region, where cells filtered in the first part pass through the GASI region to separate cells expressing the EpCAM membrane protein using EpCAM-specific antibodies functionalized on the channel walls. At this step, EpCAM-expressing cells are enriched

in the fluid channel. According to the authors' report, this μ-MACS system permits the separation of 763 cancer cells in 5 mL of blood at a flow rate of 400 μm/min. The cancer cells were classified with separation efficiencies of 10.19% and 22.91% based on the corresponding membrane proteins EpCAM or HER2 [15].

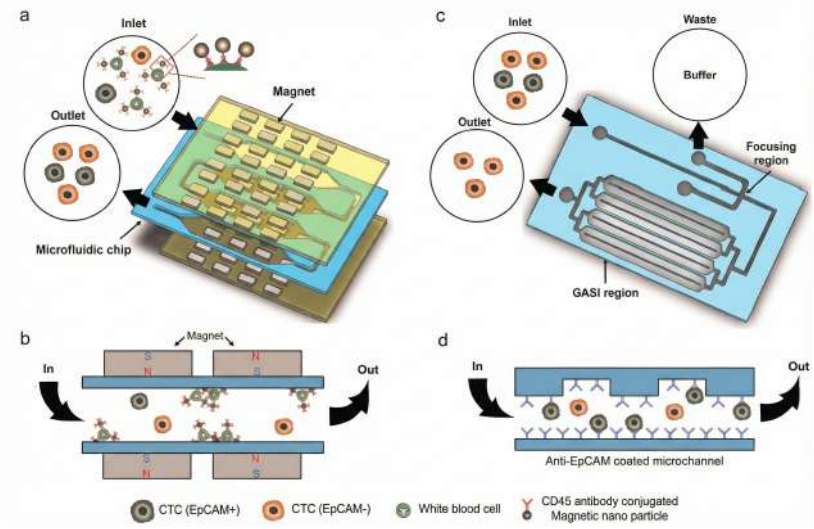

Figure 1.4: Block diagram of a CTC cell separation system utilizing magnetic nanoparticles and biological antibodies [15].

A turbulent mixer was employed to increase the probability of contact between cells and surfaces functionalized with antibodies. The herringbone (HB) pattern exemplifies a structure utilized to create turbulent mixing in microchannels where CTCs or WBCs can be captured and separated within the microfluidic structure. Recently, mixed patterns and wavy herringbone (HB) structures have been developed to improve the performance of CTC isolation. The Soper group and colleagues introduced a curved microchannel structure coated with cancer cell-specific antibodies or aptamers. The BioFluidica CTC detection system represents a modular microfluidic system for detecting CTCs, comprising three functional modules: (I) CTC capture, (II) impedance sensing, and (III) image analysis, as illustrated in Figure 1.5. Instead of the standard PDMS fabrication process, each module is produced using embossing and laser cutting with poly(methyl methacrylate) thermoplastic material. The CTC capture module contains 320 parallel curved microchannels, whose surfaces are coated with anti-EpCAM antibodies. To enhance capture efficiency, the microchannels are structured with a high aspect ratio of 30 μm width and 150 μm height, and captured CTCs are released by trypsin treatment. Compared to PDMS microfluidic devices, the rough surface of the microchannels can damage the captured CTCs during capture and release steps. In the impedance sensor module, two platinum wires (75 μm diameter) are utilized to detect the electrical signal of CTCs released from the preceding CTC capture module. The CTCs are then re-captured in the imaging module and stained with fluorescent dyes. Kamande and colleagues demonstrated that

BioFluidica can process 7.5 mL of blood within 45 minutes with high efficiency (recovery rate >90% and purity >86%).

Piezoelectric actuators are commonly employed to control individual cells by generating a pressure pulse that creates hydrodynamic forces within microchannel structures. The WOLF Cell Sorter (NanoCellect Biomedical) [27] constitutes a commercial device developed using a combination of a laser detection system and a piezoelectric-activated microfluidic device (Figure 1.5(b)). As fluorescently stained cells pass through the sensing region in the microchannel, the laser detection system identifies the cells. Subsequently, based on the signal detected from the movement of target cells, the piezoelectric actuator redirects the flow of identified cells, thereby sorting the cells in three different ways. The piezoelectric actuator exhibits a high response time of approximately 0.1 ms, enabling a high sorting throughput exceeding 1000 cells per second. This device typically requires an additional cell dispenser (N1 Single Cell Dispenser) to distribute the single cells sorted by the WOLF Cell Sorter into individual wells of 96- or 384-well plates.

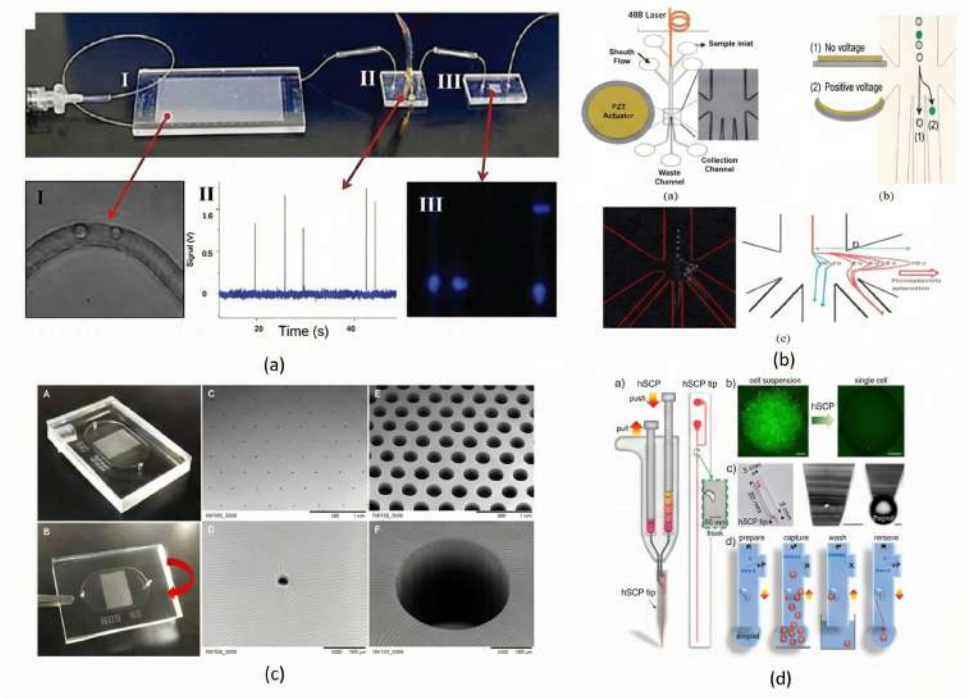

Figure 1.5: Selected recent research structures for CTC separation and isolation: (a) BioFluidica microfluidic system; (b) Microfluidic device utilizing integrated PZT membrane optical methods for isolating single CTCs; (c) Device employing dual wells and a flipping method for single-cell isolation; (d) Device utilizing a single-cell capture pipette structure.

Microstructures represent the most common approach for trapping single cells, and microarrays can be utilized to trap multiple single cells simultaneously. Lin and colleagues designed dual-well PDMS plates, each plate containing 450 micro-wells for trapping and culturing single cells (Figure 1.5(c)). When cell-containing solutions are introduced into this microfluidic structure, individual cells are retained in separate capture wells (25 μm

diameter), and any remaining uncaptured cells are removed using a wash flow with only a minimal percentage loss relative to the input cell population. Although the structure and operation of the device are simple, it can only operate with homogeneous cell populations, which necessitates careful and meticulous sample preparation.

Qin's research group introduced a single-cell pipette structure based on a microfluidic device, utilizing a microhook structure in a microchannel, as illustrated in Figure 1.5(d) [30]. While homogeneous cell populations flow through the microchannel, individual cells become trapped in individual microhooks, and the remaining cells are subsequently removed from the microchannel. Upon flow direction reversal, trapped cells are released from the microhooks, and thus the number of isolated single cells (1–10 cells) is determined by the number of microhooks. The capture rate reported by Qin (96.7%) was not affected by flow rate, which was controlled by two manual syringe plungers rather than an automatic syringe pump system. Although this represents a simple method for isolating single cells, it requires cell populations that are homogeneous at a certain concentration level (>1000 cells per μL) to maintain a high capture rate [30].

Most microfluidic-based single-cell isolation methods typically require homogenized diluted samples or complex single-cell isolation procedures, resulting in low throughput. To overcome these limitations, single-cell isolation procedures are often integrated with an additional pre-enrichment method to purify target cells from heterogeneous cell populations. In this line of research, Han and colleagues proposed a two-step hybrid microfluidic platform, comprising a magnetic micro-separation unit for enriching CTCs from whole blood and a micro-dispensing unit for isolating individual CTCs. CTCs were first enriched from whole blood and diluted fivefold using a magnetic separation method employing anti-EpCAM antibody-coated magnetic nanoparticles. In the micro-dispensing unit, enriched CTCs were identified by impedance cell measurement, and each identified CTC was encapsulated into individual droplets and dispensed into individual wells of 96- to 384-well microplates. Although this represents a label-dependent method using magnetic nanoparticles, individual CTCs can be directly isolated from fivefold diluted whole blood without losing any other CTCs through centrifugation and washing, thus achieving a high recovery rate of 99.78%, a purity of 92.45%, and a leukocyte depletion rate of 5.4 log. Using 200 μL of whole blood containing 50 MCF-7 breast cancer cells, the evaluation demonstrated that the two-step microfluidic platform can isolate single CTCs with a single-cell isolation efficiency of 82.4% and high throughput [31] (requiring only 700 ms).

1.4 Cancer cell detection and counting based on impedance signals

Following isolation of the target cancer cell population, accurate quantification of the obtained cell count represents a particularly important step in evaluating separation process effectiveness, optimizing pre-treatment conditions, and providing input for subsequent biological analyses. Reliable cell quantification facilitates determination of recovery rates and purity while supporting functional studies such as cell culture, gene-protein expression analysis, and drug response testing.

Traditional methods for detecting and counting cancer cells encompass various approaches, ranging from morphological observation to optical or biochemical signal analysis. One of the most common methods involves counting using a counting chamber (e.g., Neubauer chamber, Figure 1.6), where the sample is placed into a chamber with a standardized grid and cells are counted manually under a microscope. Although simple and cost-effective, this method is highly dependent on operator technique, prone to errors, challenging for counting low-density cells, and unsuitable for automation requirements.

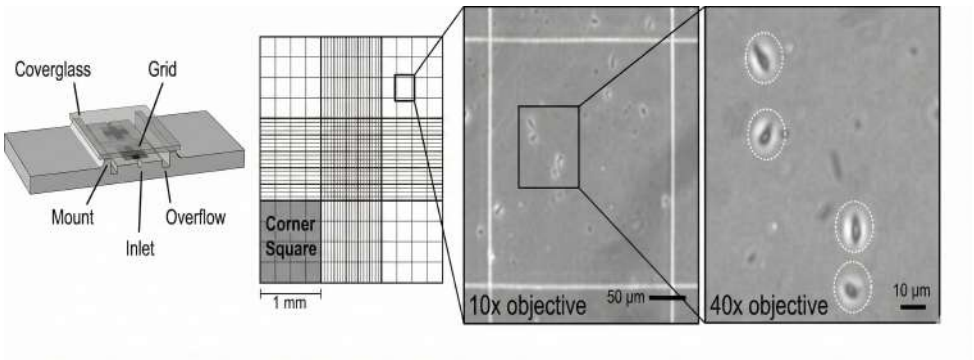

Figure 1.6: Illustration of the traditional counting method utilizing a counting chamber.

Another category of methods employs specific fluorescent labeling with antibodies or molecular probes, followed by counting using a fluorescence reader or flow cytometer (Figure 1.7). These techniques offer high sensitivity and can distinguish multiple cell populations simultaneously; however, they require complex sample processing procedures, specialized dyes and optical systems, incur high costs, and may affect cell biological activity. Other separation-detection techniques such as size-based sorting, microfluidic filtration, density gradient separation, and magnetic field separation are frequently employed to enrich cancer cells prior to counting, but they do not directly provide real-time quantitative signals.

In recent years, impedance-based cell detection and counting methods utilizing microelectrode structures (Figure 1.8) have emerged as a promising, label-free approach. As cells traverse the sensor region, impedance changes dependent on cell size, dielectric constant, and membrane properties generate characteristic signal pulses corresponding to

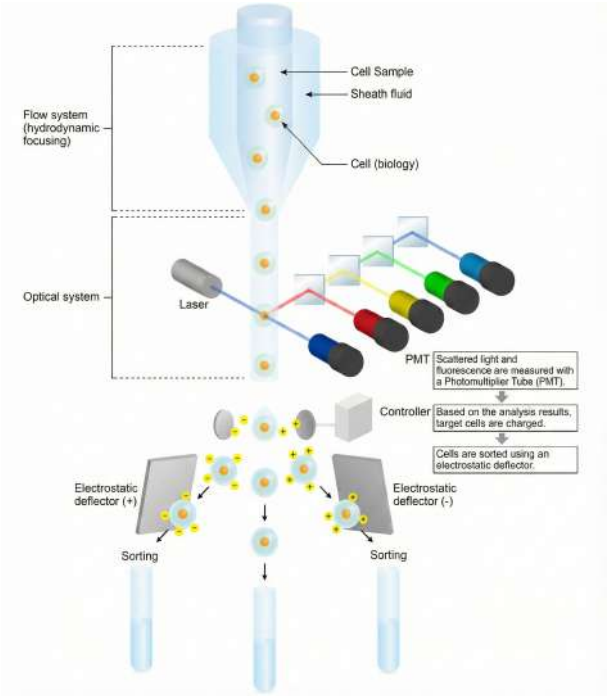

Figure 1.7: Illustration of a flow-based cell detection and quantification device.

each cell, enabling real-time counting without dyes or optical systems.

Microelectrode technology integrated into microfluidic channels represents a significant advancement in cell detection and counting. This method employs electrodes placed at multiple positions along the channel to count and classify cells based on their bioelectrical signals. One prominent application of this method involves detecting CTC cells in blood with small sample sizes, compact equipment, low cost, and rapid sample processing time, thereby improving sensitivity in early disease detection [32]. Recently, planar electrode structures have been adopted by numerous research groups worldwide for measurements of micro-particles and moving biological cells in fluid streams due to their simplicity, ease of fabrication, and suitability for various applications of fundamental microfabrication processes [33], [34], [35], [36], [37], [38]. These electrodes are employed to measure the impedance of biological cells as they traverse a fluid flow. Ayliffe and colleagues (1999) pioneered the measurement of single-cell impedance using a microdevice. They fabricated a microchannel, 10 μm wide and 4.3 μm high, using epoxy-based photoresist on a glass substrate, incorporating integrated gold electrodes 8 μm wide and 4 μm thick, as illustrated in Figure 1.9. They performed impedance measurements over a frequency range from 100 kHz to 2 MHz on human neutrophils (PMN) and fish red blood cells (RBC) suspended in different concentrations of phosphate buffer solution. This device demonstrated the ability to distinguish between different cell types, illustrating the potential of single-cell impedance analysis [38].

To date, cell impedance measurement techniques can assess numerous physiological characteristics of cells without a microscope, including cell size [32], [39], [40], morphol-

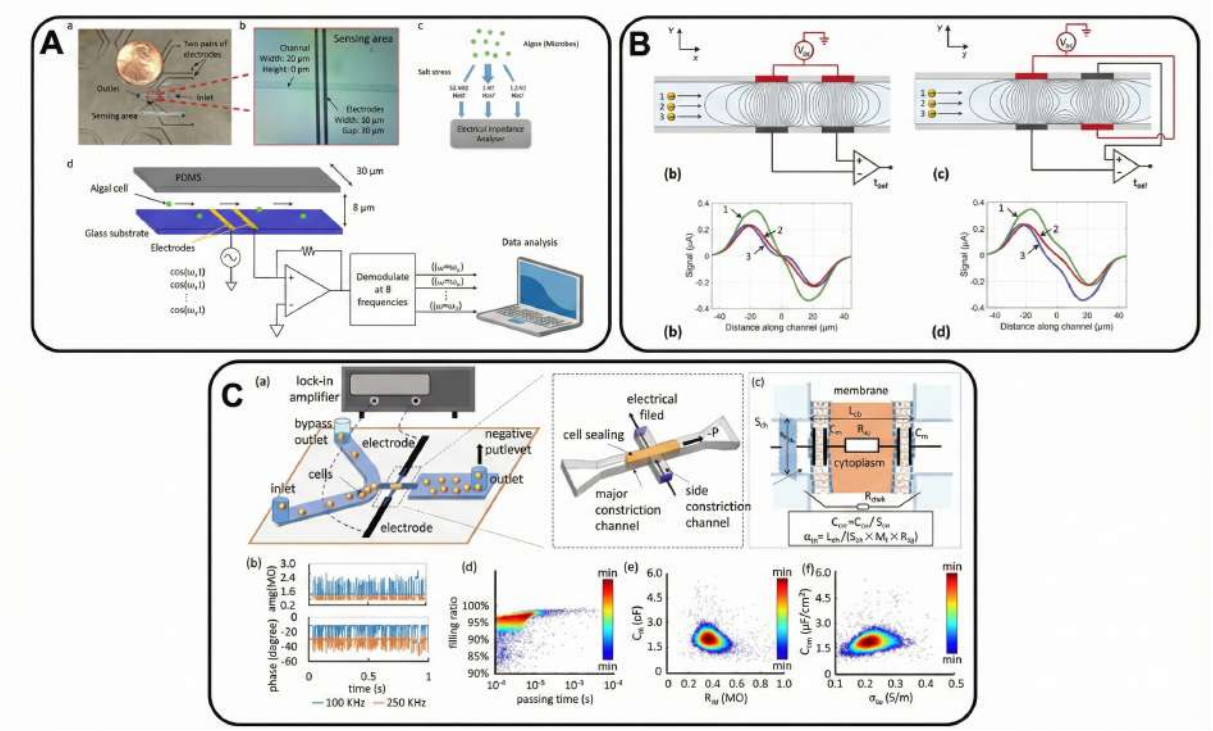

Figure 1.8: Illustration of a cell impedance signal measurement system based on microelectrodes.

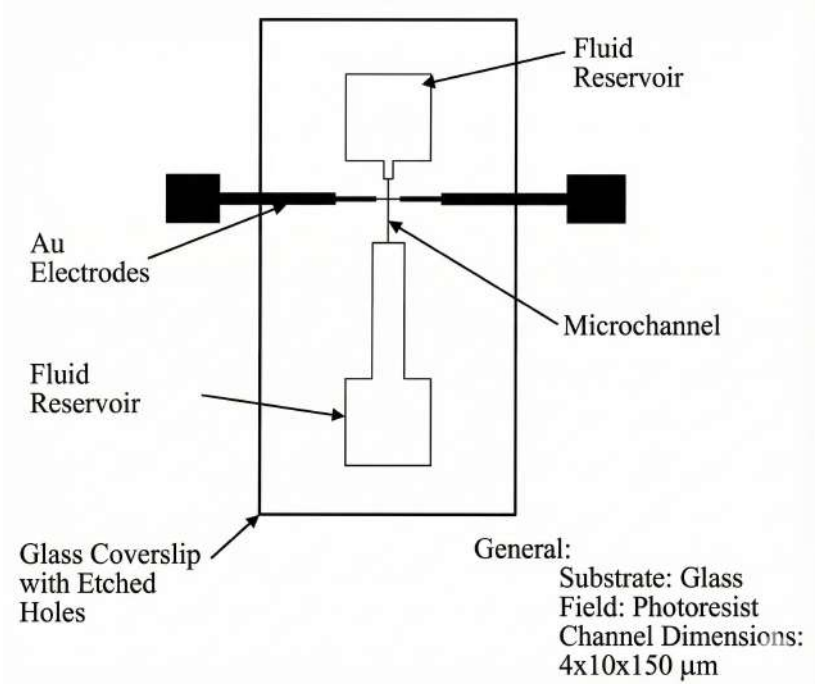

Figure 1.9: Schematic of a microelectrode impedance measurement device with gold electrodes integrated into a microfluidic channel [38].

ogy [33], [34], [35], viability [41], [42], [43], deformability [44], [45], mass [37], and intracellular components [36]. Individual cells emit multi-frequency AC signals, influenced by the detection circuit, frequency, and cellular characteristics, which are subsequently processed through a lock-in amplifier to generate an impedance data sequence. Although raw impedance data can provide preliminary information regarding cell size and characteristics, due to the nonlinearity of the detection system [46], impedance signal processing necessitates a more complex calibration and analysis process. These processes include simultaneously detecting cells and reference particles, comparing the impedance values of the cells with known reference particles, and subsequently extracting electrophysiological parameters correlated with cell characteristics. One advantage of impedance measurement is the grouping of cells or subgroups based on distinct impedance signal characteristics. Once calibrated, these characteristics can be statistically analyzed and utilized to compare physiological properties between different cell groups [34]. For example, the dielectric properties of cells can be employed to rapidly classify individual cells [47] or to identify differences between cell types within the same population, such as distinguishing cancer cells from benign cells.

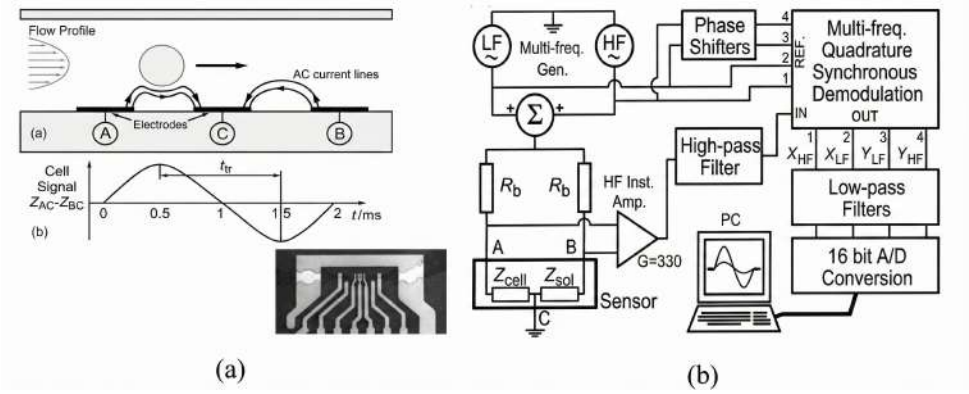

Figure 1.10: (a) Schematic illustrating a particle flowing through a microelectrode impedance chip and a typical impedance signal for a single particle. (b) Electronic components depicting the excitation, amplification, and demodulation sections of the mixed-frequency detection circuit.

In 2001, Gawad et al. introduced a significant advancement in single-cell impedance technology, demonstrating clear differentiation between red blood cells and platelets [48]. The single-cell impedance analysis method employed in this study is illustrated in Figure 1.10(a). Two pairs of microelectrodes are fabricated at the bottom of a microchannel. These electrodes are activated by voltage at a specific frequency, generating a non-uniform electric field inside the channel. One pair detects the current fluctuations caused by a cell, while the other pair measures the current flowing through the pure medium, serving as a reference. Microelectrodes similar in size to a cell (ranging from 10 to 30 μm) are employed to detect impedance signals from single cells. The current from the two sensor blocks is converted into a voltage signal via a transimpedance amplifier. Subsequently, a differen-

tial amplifier calculates the difference between these signals. A lock-in amplifier is utilized to demodulate in-phase and out-of-phase impedance signals at the excitation frequency while filtering noise at other frequencies (Figure 1.10(b)). The impedance variation, measured differentially, is represented as a pair of peaks. This differential impedance sensing method offers several advantages, as highlighted by Gawad et al.: (i) direct measurement of cell properties relative to the buffer environment, (ii) elimination of any uneven drift in electrode properties, and (iii) determination of cell velocity based on the transit time between peaks [32].

In summary, the method of detecting and quantifying cancer cells based on impedance signals offers numerous advantages, including simple equipment, straightforward integration into microfluidic systems, low sample consumption, rapid analysis speed, and reduced operating costs. The development of sophisticated microelectrode structures such as three-dimensional or multi-electrode configurations, along with multi-frequency measurement, continues to enhance sensitivity and resolution, establishing impedance-based counting as a significant trend in label-free cancer cell quantification and next-generation mobile testing systems.

1.5 System Proposal

From the preceding analysis, it is evident that research, design, fabrication, measurement, and testing of microfluidic systems continue to face numerous challenges. Currently, Lab-on-a-Chip (LoC) systems primarily focus on individual functions such as detection or cell separation but lack comprehensive integrated studies encompassing detection, separation, and cell isolation within a single system. This represents a significant limitation, particularly as the demand for mobile, automated, and practical biomedical devices continues to increase. An urgent need in modern cancer diagnosis and treatment is early detection and non-invasive monitoring through liquid biopsy, wherein the analysis of circulating tumor cells (CTCs) plays a crucial role. However, CTCs exist at extremely low densities in peripheral blood (approximately 1–10 cells per mL of blood), necessitating methods with very high sensitivity and specificity. Traditional analysis procedures often involve multiple manual steps, are time-consuming, require bulky equipment, and are prone to errors. Therefore, developing a Lab-on-a-Chip system that integrates the entire process from raw blood sample processing to analysis and isolation of individual cells on a single platform represents an important objective with the potential to revolutionize the field of cancer diagnosis.

This thesis proposes a Lab-on-a-Chip system utilizing an integrated microfluidic chip platform with an automated magnetic separation system, combined with a quantitative sensor for detecting and analyzing cancer cells in a flow. The multifunctional integrated Lab-on-a-Chip system proposed in this study offers significant advantages over existing

single-function systems. By combining multiple functional modules on a single chip, the system minimizes human intervention, thereby limiting errors and the risk of sample cross-contamination. Furthermore, full automation of the process significantly shortens analysis time, increases sample throughput, and improves the reproducibility of results. Most importantly, the integration enables continuous analysis of cells immediately after sorting, preserving cell integrity and viability—a critical factor for downstream analyses such as cell culture or gene sequencing. The proposed system integrates the following key functions: (1) CTC separation and enrichment based on specific magnetic methods; (2) Separation of cell clusters into single cells using inertial force; (3) Encapsulation of single cells into oil-in-water microdroplets; (4) Detection and quantification of single cancer cells; and (5) Sorting and collection of microdroplets containing target cells.

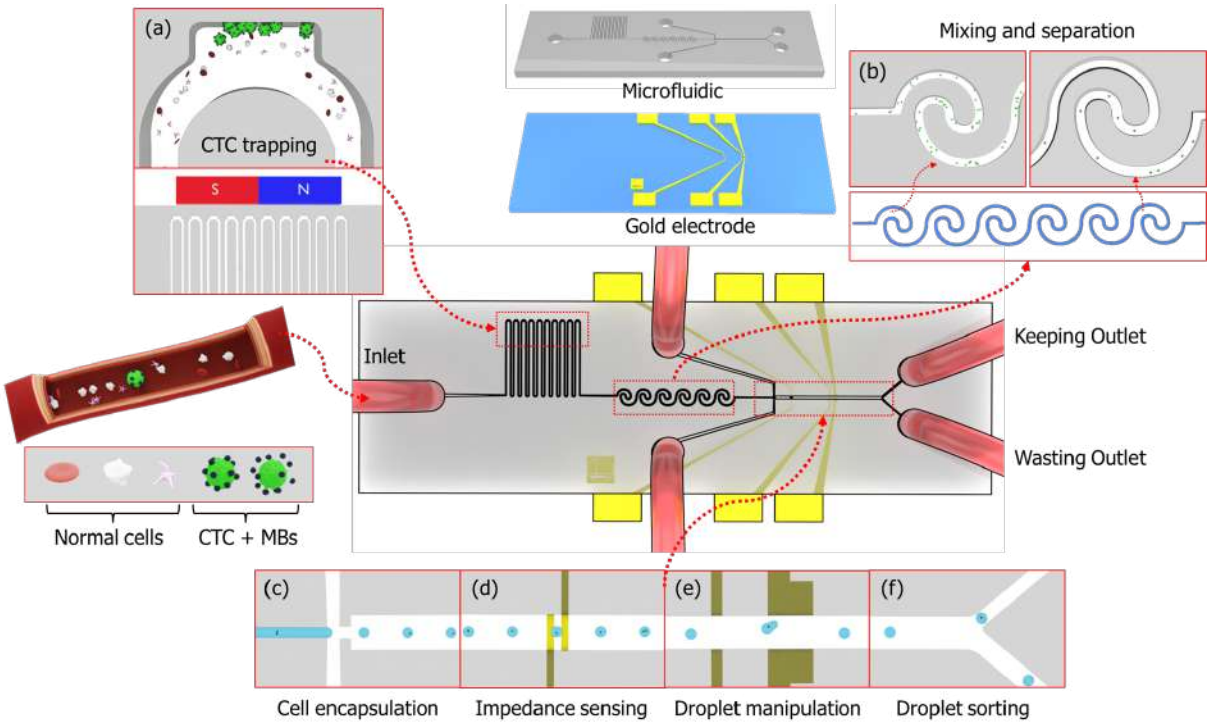

Figure 1.11: Schematic illustration of the integrated Lab-on-a-Chip platform for single-cell analysis, detailing the sequential operational stages: (a) Upstream magnetic trapping zone for selective enrichment of magnetically labeled CTCs. (b) Inertial microfluidic channel for cell ordering and spacing. (c) Cell encapsulation unit generating water-in-oil microdroplets at a T-junction. (d) Integrated electrode region for impedance-based detection of droplet contents. (e) Active microdroplet manipulation and sorting section. (f) Downstream sorting junction directing droplets into collection or waste outlets based on sensor feedback.

To maximize the potential of the proposed multifunctional LoC, constructing a complete peripheral device system capable of integrating, synchronizing, and automating processes is essential. Although microfluidic chips with core functions such as magnetic separation, cell encapsulation, and sorting play a central role, operational efficiency in real-world applications, particularly in point-of-care (POC) systems, depends on a sup-

porting ecosystem comprising specialized modules: flow control, signal acquisition and processing, optical observation, and user interface. The proposed device system aims to comprehensively address these challenges, establishing a closed-loop automated cell analysis platform capable of processing samples from input to final quantitative results. The design emphasizes compactness, simple operation, and automation of complex chip operations, thereby shortening analysis time and improving reliability.

As illustrated in Figure 1.11, the device operates through a comprehensive sequential workflow comprising six strategic stages to optimize sensitivity and specificity: (a) an upstream magnetic trapping zone utilizing a cavity-integrated microchannel for the selective enrichment of lung cancer cells magnetically labeled via aptamer binding; (b) an inertial microfluidic channel featuring a serpentine design to facilitate cell ordering and spacing prior to downstream processing; (c) a cell encapsulation unit that generates water-in-oil microdroplets at a T-junction, isolating single cells for discrete analysis; (d) an integrated electrode region performing real-time impedance-based detection of droplet contents; (e) an active microdroplet manipulation and guidance section; and finally, (f) a downstream sorting junction that directs droplets into collection or waste outlets based on sensor feedback. This architecture enables continuous operation, minimizing human intervention and operational errors while enhancing the reliability of the analysis. Detailed descriptions of the scientific basis, experimental methodology, and achieved research results of the proposed system are presented in the subsequent chapters:

Chapter 2 – Theoretical Basis and Simulation presents the scientific foundation underlying the entire study, including theories on microchip system design, the mechanism of interaction between aptamers and magnetic particles in cancer cell detection, the principle of magnetic separation, the theoretical basis of impedance sensors, and the design of microelectrode structures. Additionally, this chapter discusses the theoretical basis of the droplet encapsulation and separation method utilizing DEP, along with simulation modeling for each functional structure in the system, including simulation of the magnetic separation system, impedance sensor, and droplet control area.

Chapter 3 – Experimental Setup focuses on the process of circuit design and microfluidic chip fabrication, from the material preparation stage, electrode and microfluidic channel fabrication processes, to the setup of experiments corresponding to each function of the system such as magnetic separation, impedance counting, droplet encapsulation, and separation. Additionally, this chapter introduces signal acquisition and processing methods, as well as cell quantification and classification techniques based on machine learning and computer vision to enhance accuracy in cell counting and analysis.

Chapter 4 – Results and Discussion summarizes and analyzes the results obtained from the manufacturing, simulation, and experimental processes. The content includes the results of manufacturing the measurement system and microfluidic chip, evaluating the performance of the impedance sensor simulation, as well as the results of magnetic

separation, impedance counting, encapsulation, and droplet separation. Additionally, this chapter presents the application of machine learning models in signal processing and analysis to automate the cell recognition and counting process, thereby confirming the feasibility, effectiveness, and application potential of the proposed system.

1.6 Conclusion

This chapter has provided a comprehensive overview of the current landscape of cancer research, with a specific focus on the critical role of Circulating Tumor Cells (CTCs) as key drivers of lung cancer metastasis. While CTCs hold immense potential as biomarkers for early diagnosis, prognosis, and treatment monitoring, their extreme rarity and heterogeneity in peripheral blood present significant challenges for effective isolation and analysis. Evaluating existing technologies reveals that although methods such as immunomagnetic separation and microfluidic-based approaches have made strides, many still suffer from limitations including complex sample preparation, low throughput, or insufficient purity for downstream molecular analysis. Addressing these gaps requires a transition towards more integrated and automated systems. The proposed Lab-on-a-Chip platform aims to bridge this engineering-clinical divide by combining magnetic enrichment, inertial focusing, and droplet-based single-cell analysis into a unified, automated workflow. This integrated approach promises to enhance the sensitivity and specificity of CTC detection, potentially facilitating more accessible and precise non-invasive liquid biopsy applications in clinical oncology.

Chapter 2

THEORETICAL BASIS AND SIMULATION

2.1 Theoretical basis and system design

2.1.1 Mechanism of aptamer-magnetic particle binding in cancer cell detection

The core of the separation method is the magnetic principle, in which nano-magnetic particles are surface-functionalized and subsequently attached to the A549 cancer cell membrane. This attachment process is achieved through a highly specific biochemical interaction between the aptamer and the biomarkers expressed on the A549 cell surface. The selection of aptamers instead of traditional antibodies offers numerous advantages in terms of stability, cost, and synthesizability [49], [50]. The SELEX (Systematic Evolution of Ligands by Exponential Enrichment) method, independently developed by Tuerk and Gold [51] and Ellington and Szostak [52], has revolutionized the generation of aptamers with high specificity. The surface functionalization of magnetic particles plays a crucial role in ensuring specific and effective binding between magnetic particles and target cells. In this study, Fe_3O_4 magnetic particles were functionalized by covalently linking them to the EpCAM-specific aptamer, a synthetic oligonucleotide capable of specifically recognizing the EpCAM antigen on the surface of A549 lung cancer cells [53]. The specific process involved a series of chemical reactions and processing steps to optimize aptamer binding to the magnetic particle surface.

Initially, the carboxyl groups (-COOH) on the surface of the magnetic particles were activated using a pair of reactants: EDC (1-ethyl-3-(3-dimethylaminopropyl) carbodiimide) and NHS (N-hydroxysuccinimide). This reaction produces active esters capable of strongly interacting with the amino ($-NH_2$) groups of the aptamer. In this reaction system, EDC acts as a catalyst to form a direct covalent bond between the carboxyl group

on the magnetic particle and the amino group of the aptamer, while NHS stabilizes the intermediate ester bond, thereby enhancing reaction efficiency and preventing unwanted hydrolysis.

Following the activation of carboxyl groups with EDC/NHS, the EpCAM-specific aptamer with the structure 3'–ACGC TCGG ATGC CACT ACAG GGTT GCAT GCCG TGGG GAGG GGGG TGGG TTTT ATAG CGTA CTCA GCTC ATGG ACGT GCTG GTGA C–5'-NH_2 is added. This aptamer is modified at the 5' end with an amino group to facilitate covalent linkage with the active ester on the particle surface. This specific aptamer recognizes and selectively binds to EpCAM cell membrane proteins, which are transmembrane receptors comprising extracellular domains for ligand binding, transmembrane domains, and intracellular domains capable of signaling within the cell (Figure 2.1).

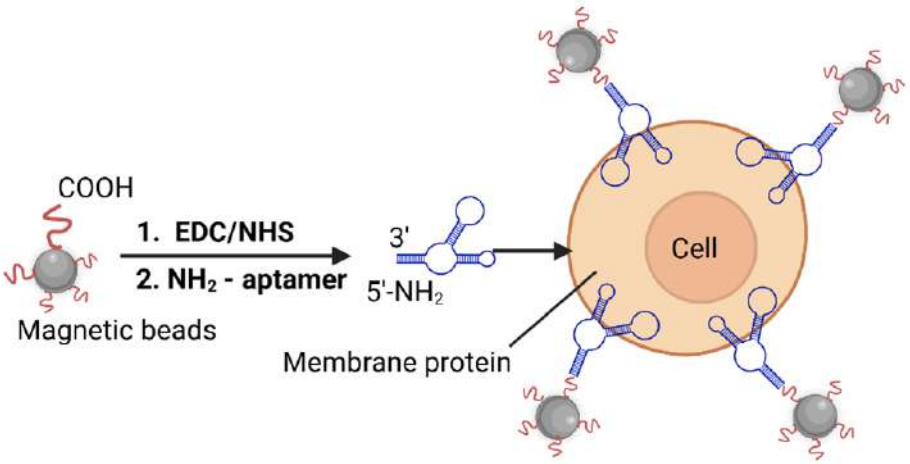

Figure 2.1: The adhesion of MB to the membrane proteins of the A549 target cells is mediated by the NH_2 aptamer.

The buffer solution utilized in the aptamer binding process comprises PBS (phosphate-buffered saline) to maintain stable pH and reaction conditions, BSA (bovine serum albumin) to block non-specific binding sites on the particle surface, $MgCl_2$ to stabilize the spatial structure of the aptamer under suitable ionization conditions, and yeast tRNA as an auxiliary blocking agent to prevent the aptamer from binding to unwanted surfaces. Specifically, the magnetic particles were treated by stirring them in an EDC/NHS mixture in MES buffer (2-(N-morpholino) ethanesulfonic acid, pH 6.0) for 30 minutes to ensure effective activation. Following this activation step, the EpCAM aptamer is added to the solution at an appropriate concentration (10 μM) and allowed to react at room temperature for 90 minutes. The immediate addition of aptamer minimizes the hydrolysis of the intermediate ester, thereby enhancing the efficiency of aptamer binding to the magnetic particle surface.

After incubation, the aptamer-bound magnetic particles are washed multiple times with PBS solution using a magnetic rack to remove excess unbound aptamer and reaction

byproducts. Following washing, the functionalized magnetic particles were prepared for binding to target cells. To proceed with subsequent experimental tests, a defined quantity of A549 lung cancer cells was mixed with the functionalized magnetic particles for 30 minutes, allowing the magnetic particles to bind specifically and efficiently to the cell surface via the attached aptamers. Experiments were conducted with superparamagnetic beads of different diameters, at a particle concentration of 8.15 mg-Fe/mL and an aptamer binding density of 0.2 mM. These magnetic particles were supplied by Bio-Cando Inc. (Taoyuan, Taiwan). The functionalization process was uniformly applied to all bead sizes to compare and evaluate the effect of bead size on target cell capture efficiency. To assess the specificity of the functionalization process and magnetic bead binding to lung cancer cells, the research group performed separation of a mixture of lung cancer cells and HeLa cells [54].

2.1.2 Theoretical basis of magnetic separation and cavity-integrated microchannel design

After completing the magnetic labeling step, the cell suspension is introduced into the proposed LoC platform through the inlet and first guided to the magnetic separation module. In this initial stage, the magnetically labeled target cells are subjected to a strong non-uniform magnetic field generated by an external permanent magnet. The proposed design is a microfluidic chip system termed a cavity-integrated microchannel [55]. The integration of magnetism with microfluidics has opened new possibilities for precise manipulation of biological samples [56]. The primary function of this structure is to selectively separate and capture magnetic particle-labeled CTCs from a mixed sample, such as whole blood. Structurally, the chip consists of a channel fabricated from PDMS material bonded onto a transparent glass substrate, with an inlet for sample introduction and an outlet for solution recovery.

The main channel of the chip is designed in a serpentine configuration. This structure generates centrifugal forces at the bends, pushing cells toward the outer walls of the channel where the trap chambers are located. The main channel has a width of 100 μm and a total height of approximately 100 μm. The trap chambers are rectangular extensions designed to optimize cell retention. Each chamber measures 340 μm in length and 100 μm in width. They are positioned along the outer wall of the curved segments in the serpentine channel, facing the magnet. To generate the necessary magnetic field, a permanent $Nd_2Fe_{14}B$ (N35) magnet measuring 20 mm (length) $\times$ 5 mm (width) $\times$ 5 mm (thickness) is employed. This magnet is placed at a distance of 1.5 mm to 3.0 mm from the chambers to ensure a sufficiently strong magnetic field gradient for cell trapping (Figure 2.2).

After the magnetic labeling process is complete, the mixed sample containing normal cells and A549 cells labeled with magnetic particles is pumped into a microfluidic chip.

This chip is designed and manufactured with optimized geometric structures, including channels and specialized trap regions. By integrating an external permanent magnet system, a high-intensity, non-uniform magnetic gradient field is generated within the trap regions inside the microfluidic channel. Under the influence of the magnetic force, the magnetically labeled A549 cells are deflected from the main flow and are attracted and retained in these trap regions. Meanwhile, normal cells unaffected by the magnetic field continue to move with the fluid flow and are subsequently discharged. This process enables the efficient and selective separation and enrichment of rare cancer cells.

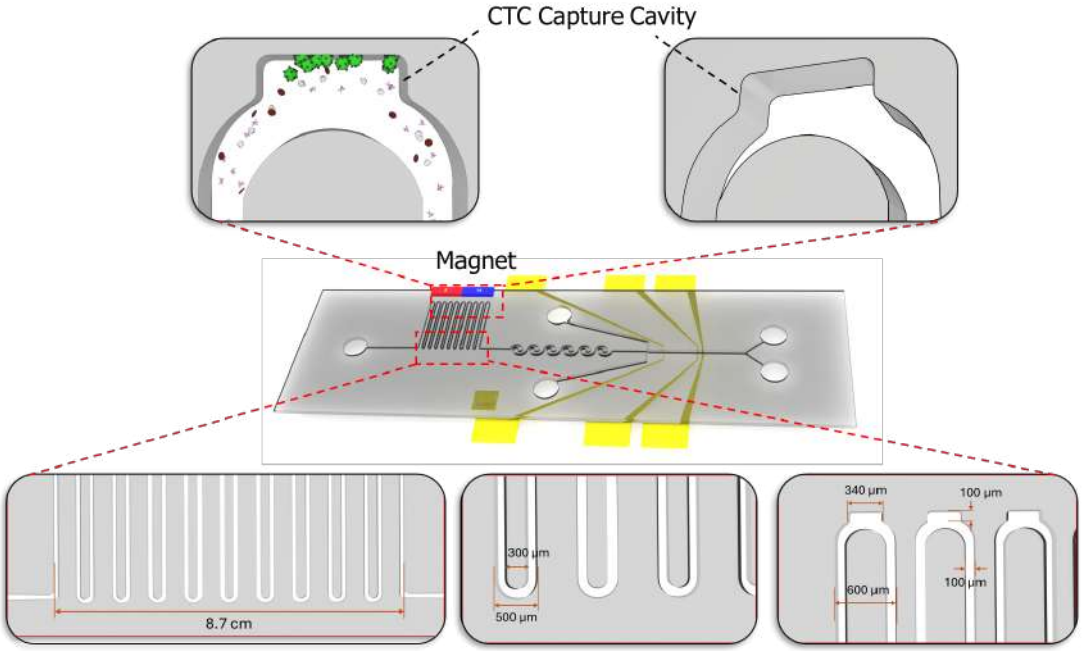

Figure 2.2: The proposed microfluidic system for CTC isolation in cavities. A. Schematic of the microfluidic device consisting of a channel pad placed on a glass substrate. The channel dimensions are 100 μm in width for the main channel, while the cavities (cell retention regions) extend to a length of 340 μm and a width of 100 μm.

In studies on cell separation employing magnetic techniques integrated with microfluidic chips, the selection of suitable magnetic beads is a key factor that significantly determines the recovery efficiency, purity, and biological stability of the system [57], [58]. Magnetic beads commonly utilized in this field are typically based on a ferromagnetic iron oxide core Fe_3O_4 (magnetite), with nano or micro sizes, coated with functional polymer layers such as streptavidin/avidin, silica, or polystyrene to enhance their binding capacity with biological recognition agents such as aptamers or specific antibodies. Currently, these types of particles have been widely commercialized by reputable suppliers such as TANBead, Dynabeads, and MagSi, ensuring uniformity in size and quality. Microchip-based immunomagnetic detection of circulating tumor cells has been demonstrated with high efficiency [59].

In this study, superparamagnetic magnetic beads were selected to systematically in-

vestigate the effect of particle size on the efficiency of capturing A549 cancer cells in different microfluidic configurations. The beads utilized possess an Fe_3O_4 magnetic core with a biocompatible polymer coating, enabling them to stably bind to specific biological recognition molecules. Different particle sizes were selected to serve specific purposes in the study. Smaller magnetic particles allow for easier movement and penetration of narrow structures in microchannels, increasing contact area and coverage on the cell surface, particularly in complex microfluidic channel designs. Conversely, larger magnetic particles provide stronger magnetic forces, improving cell displacement and capture under high magnetic field gradients. However, the utilization of larger particles also poses certain challenges, such as reduced biological contact area on the cell surface or the risk of microfluidic channel clogging if the design is not properly optimized.

All magnetic particles selected in this study possess superparamagnetic properties, meaning they exhibit magnetism only when exposed to an external magnetic field and lose all magnetism when the field is removed. This characteristic prevents particle agglomeration, ensures uniform and stable dispersion in the buffer solution, and minimizes adverse effects on living cells, which are highly sensitive to environmental conditions. Additionally, these magnetic particles fully satisfy the criteria for biocompatibility, are non-cytotoxic, and remain stable in common buffer solutions such as PBS, rendering them highly suitable for biological analysis applications and integration into Lab-on-a-Chip systems.

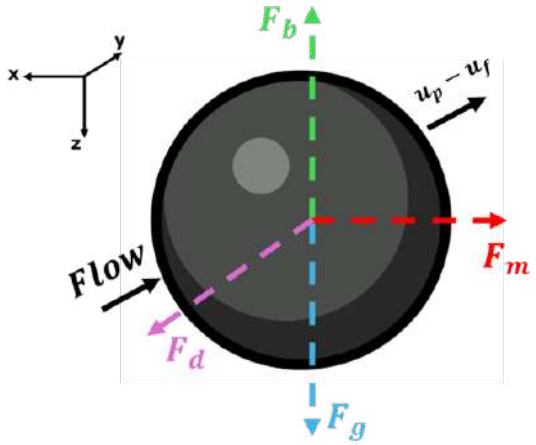

Figure 2.3: Schematic of force interactions on magnetic particles during magnetic migration.

Magnetic separation techniques in microchannels are based on controlling the trajectory of cells/microparticles containing magnetic beads (MB) under the simultaneous action of an electric field and a magnetic field. This motion follows Newton's Second Law, described by the equation:

$$m\frac{du_p}{dt} = F_m + F_d + F_g + F_b + F_L \tag{2.1}$$

where m is the particle mass, u_p is the particle velocity, and F_m, F_d, F_g, F_b, and F_L represent the magnetic force, hydrodynamic drag force, gravitational force, buoyant force, and lift force, respectively (Figure 2.3). At the micro/nano scale and low flow velocity (Reynolds $\ll 1$), the inertial component on the left-hand side is negligible; thus, the particle's state is primarily determined by the balance between magnetic force and drag force.

The magnetic force F_m acting on a superparamagnetic particle of radius R in a magnetic field gradient ∇B is calculated as:

$$F_m = \frac{V_p(\chi_p - \chi_f)}{\mu_0}(B \cdot \nabla)B \tag{2.2}$$

where $V_p = (4/3)\pi R^3$ is the particle volume, χ_p and χ_f are the relative magnetic permeability of the particle and the medium, respectively, and μ_0 is the vacuum magnetic permeability. This formula demonstrates that the magnetic force is proportional to the cube of the particle size and the linear gradient of the magnetic field; therefore, to control micrometer-sized particles at a flow velocity of millimeters per second, both an appropriate MB design and a sufficiently large magnetic gradient configuration are required ($|\nabla B| \approx 10^4$–10^6 T/m).

Meanwhile, the hydrodynamic drag force $F_d = 6\pi\mu_f R(u_f - u_p)$ follows Stokes' law, where u_p and u_f are the particle and fluid velocities, respectively. Since F_d increases linearly with particle size, larger particles, while experiencing stronger magnetic forces, also encounter greater drag forces, necessitating simultaneous optimization of both quantities in the design.

The two vertical force components—gravitational force $F_g = \rho_p V_p g$ and buoyancy force $F_b = -\rho_f V_p g$—typically account for only a few percent of F_m in buffer solutions ($\rho_f \approx 1000\,\mathrm{kg\,m^{-3}}$) and MB polymer coated with Fe_3O_4 ($\rho_p \approx 1200$–$1500\,\mathrm{kg\,m^{-3}}$). The lifting force F_L [60], arising from shear gradients, is considerably smaller in magnitude than the magnetic force but can assist in redistributing particles away from the channel wall.

To quantify the relative advantage between magnetic force and drag force, the dimensionless coefficient M is defined:

$$M = \frac{|F_m|}{|F_d|} = \frac{(\chi_p - \chi_f)R^2}{9\mu_0\mu_f} \cdot \frac{(\mathbf{B} \cdot \nabla)\mathbf{B}}{u_f} \tag{2.3}$$

When $M \ll 1$, particles are completely entrained by the flow; when $M \gtrsim 1$, the deflection trajectory is sufficiently large for particles to collide with the collection surface or exit the main flow. The response time $\tau = m/(6\pi\mu_f R)$ is in the sub-millisecond range, confirming that neglecting inertia is feasible in most microfluidic configurations.

Several important design implications can be derived from the above analysis. First,

the choice of MB size requires a trade-off: particles ≥ 4 μm generate strong magnetic forces but reduce antibody coverage area, while particles of 0.5–1 μm provide a large conjugate surface but require a higher magnetic gradient. Second, magnets or microelectrodes must be positioned so that the magnetic gradient is horizontal, reducing interaction with gravity, while achieving $|\nabla B|$ on the order of 10^5 T m^{-1} in the 50–100 μm region near the channel wall. Third, a flow velocity in the range of 0.5–2 mm s^{-1} (Re ≈ 0.01) ensures laminar flow and enables achieving $M \approx 1$ with an MB diameter of 2 μm under a 0.5 T field. Finally, the channel geometry design can exploit the Saffman lift force [61] to converge the CTC flow before magnetic pressure, thereby enhancing purity.

The device's operating principle relies on the interaction and imbalance between two primary forces: magnetic force and hydrodynamic drag. When the cell mixture, comprising target cells (magnetically labeled) and non-target cells, is pumped into the channel, an external permanent magnet generates a strong magnetic field gradient. The cell-magnetic particle complexes are subjected to the magnetic force (F_m), pulling them toward the region with the strongest magnetic field, i.e., toward the magnet. Simultaneously, all cells in the flow are affected by the hydrodynamic drag force (F_d), which tends to carry them away with the fluid flow out of the channel. Although other forces such as gravitational force (F_g), Brownian force (F_b), and hydrodynamic lift force (F_L) also act on the cells, their effects are negligible compared to the two dominant forces: magnetic force and drag force.

The separation occurs efficiently due to the channel's specialized design, with trap chambers positioned near the magnet. In these areas, the geometric structure causes the flow velocity to decrease to very low levels, approaching zero. This significantly reduces the drag force (F_d) acting on the cells. As a result, the magnetic force (F_m) dominates, readily pulling and trapping the cell-magnetic particle complexes into the chambers. Conversely, non-target cells, unaffected by the magnetic field, continue to be carried by the main flow's drag force through the chambers and out through the outlet. Thus, the microfluidic design configuration simultaneously utilizes the hydrodynamic properties of the serpentine channel and the trapping effect of the microstructural chambers. This combination enables effective control of the forces acting on the cells, achieving high capture efficiency and selectivity for target cells.

2.1.3 Theoretical basis of inertial microfluidics and spiral channel design

To ensure the efficiency of downstream impedance-based cell counting and cell encapsulation in microdroplets, cell ordering (arranging cells into a single file) and uniform longitudinal spacing are prerequisite requirements. Inertial microfluidics exploits fluid inertia at intermediate Reynolds numbers to achieve size-based particle focusing and sep-

aration without external forces [62]. In this study, the utilization of a continuous spiral inertial microfluidic structure is proposed to leverage hydrodynamic forces for the effective focusing and spacing of the cell stream. The fundamental principles of inertial focusing have been comprehensively reviewed [63], and spiral microchannels utilizing Dean flow effects have demonstrated effective continuous particle separation [64], [65].

Based on the design presented in Figure 2.4, the inertial channel structure is positioned at the intermediate stage of the LoC chip, immediately following the magnetic separation unit and preceding the impedance sensor. The channel features a serpentine configuration but is optimized as a chain of interconnected spiral structures (continuous spiral structure) to optimize the channel length within a compact footprint while enhancing the secondary Dean flow effect.

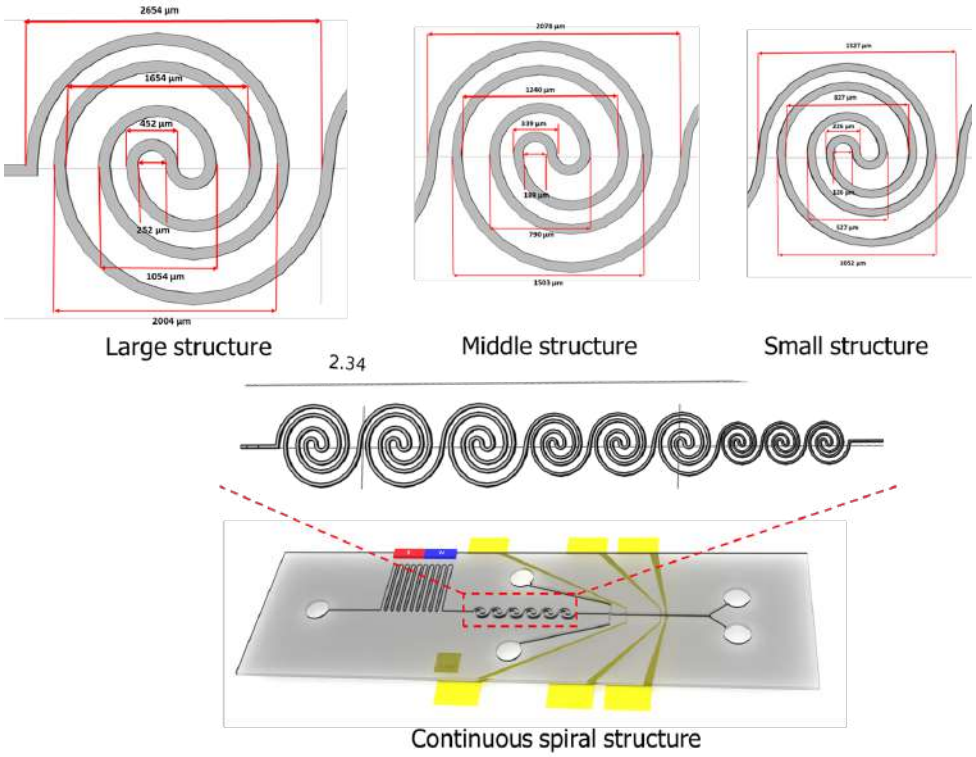

Figure 2.4: Proposed continuous spiral structure with progressively decreasing dimensions.

The structure consists of a series of spiral loops with progressively decreasing dimensions along the flow direction to gradually increase the fluid velocity and the forces acting on the cells. Specifically, the design comprises three main sections: a large structure located at the inlet to stabilize the initial flow and initiate the separation of cell clusters; a middle structure with reduced spiral loop sizes to increase the magnitude of the Dean number, thereby promoting the migration of cells toward equilibrium positions; and a small structure at the final section before the sensing region, where inertial forces reach their maximum to ensure precise cell focusing at the channel center and establish stable longitudinal spacing.

The migration of particles or cells within a microfluidic channel is governed by hydrodynamic forces arising from the inertia of the fluid. Two primary physical phenomena govern this process: (1) lateral migration due to inertial lift forces (inertial migration) and (2) secondary Dean flow in curvilinear channels.

Reynolds Number and Inertial Lift Force (F_L) In a straight channel, particle migration is characterized by the particle Reynolds number (Re_p) and the channel Reynolds number (Re_c):

$$Re_c = \frac{\rho U_{max} D_h}{\mu} \tag{2.4}$$

Where:

- ρ: Fluid density (kg/m^3).
- U_{max}: Maximum fluid velocity (m/s).
- D_h: Hydraulic diameter of the channel (m); for a rectangular channel, $D_h = \frac{2wh}{w+h}$.
- μ: Dynamic viscosity of the fluid ($Pa \cdot s$).

When Re_c is in the intermediate range (typically 1 to 100), inertial forces become significant. Cells experience two opposing lift force components:

1. **Wall-induced lift force (F_{LW}):** Repels the cell away from the channel wall due to the hydrodynamic interaction between the particle and the wall.
2. **Shear-gradient lift force (F_{LS}):** Pushes the cell toward the channel wall due to the curvature of the parabolic velocity profile.

The net inertial lift force (F_L) acting on a spherical cell of diameter a is expressed as:

$$F_L = C_L \rho G^2 a^4 \tag{2.5}$$

Or expressed in terms of flow velocity:

$$F_L = f_L(Re_c, x_c) \frac{\rho U_{max}^2 a^4}{D_h^2} \tag{2.6}$$

Where C_L and f_L are dimensionless lift coefficients, dependent on the particle position (x_c) and the Reynolds number; a is the cell diameter. This force F_L tends to drive cells to stable equilibrium positions located between the channel center and the walls.

Dean Flow and Dean Drag Force (F_D) in Curvilinear Channels For serpentine or spiral channel structures as proposed, the continuous change in flow direction generates centrifugal forces, leading to the formation of two counter-rotating vortices perpendicular to the main flow, known as Dean vortices. The intensity of this secondary flow is characterized by the Dean number (De):

$$De = Re_c\sqrt{\frac{D_h}{2R}} \tag{2.7}$$

Where R is the radius of curvature of the channel. In the proposed design, the radius R decreases from the Large Structure to the Small Structure, causing the Dean number to increase along the channel length, thereby enhancing mixing and particle focusing effects.

Cells entrained in the Dean flow experience a lateral Stokes drag force, referred to as the Dean drag force (F_D):

$$F_D = 3\pi\mu U_{Dean} a \tag{2.8}$$

The Dean velocity (U_{Dean}) typically scales with the Dean number according to the empirical relationship $U_{Dean} \sim 1.8 \times 10^{-4} De^{1.63}$. Consequently, the Dean drag force scales as:

$$F_D \propto \frac{\rho U_{max}^2 a D_h^2}{R} \tag{2.9}$$

Mechanism of Cell Ordering and Spacing Cell focusing is achieved through the balance between the inertial lift force (F_L) and the Dean drag force (F_D). The ratio of these two forces determines the final equilibrium position of the cells:

$$R_f = \frac{F_L}{F_D} \sim \frac{a^3 R}{D_h^3} \tag{2.10}$$

- If $R_f \to 0$ (small particles or small R): Dean drag dominates, causing cells to be entrained in Dean vortices and mixed.
- If R_f is sufficiently large (large cells such as CTCs): Inertial lift forces maintain the cells at stable equilibrium positions, while Dean drag pushes them toward a single position on the cross-section, resulting in single-stream ordering.

Simultaneously, longitudinal spacing is established due to differential migration velocities. Once cells enter the equilibrium streamline, hydrodynamic repulsion between cells, combined with the velocity profile of the flow, prevents cell clustering (clumping) and maintains a uniform distance between them. This ensures that when passing through the downstream impedance sensor, signals do not overlap, thereby enhancing measurement accuracy.

The spiral design with a decreasing radius of curvature R in this system allows for the fine-tuning of the R_f ratio along the flow path, ensuring that even cells with varying sizes are effectively focused before entering the counting and droplet encapsulation modules.

2.1.4 Theoretical Basis for cell encapsulation in droplets

Cell encapsulation in microdroplets is a widely used technique in microfluidics, enabling high-throughput single-cell analysis and manipulation. This method involves generating uniform microdroplets that can encapsulate individual cells or small groups of cells, providing isolated microenvironments for various biological assays **Chin2011**. The droplet generation process typically occurs in microfluidic channels designed to create controlled shear forces that fragment a continuous phase into discrete droplets containing the dispersed phase (cells suspended in a suitable medium) [66].

In this study, after completing the cell ordering process in the spiral microchannel, the cells are directed to the droplet encapsulation module to perform encapsulation into microdroplets. This process is carried out in a T-junction microfluidic channel, where the continuous phase (oil) and the dispersed phase (cell-containing suspension) meet at the junction to generate uniform droplets containing cells.

In a T-junction geometry, the dispersed phase (typically an aqueous, cell-containing suspension) flows through the side branch and intersects the continuous phase (typically oil) at the T intersection. Under the combined action of shear stresses and the pressure buildup imposed by the continuous phase, a droplet "neck" forms and progressively thins until pinch-off occurs, yielding water-in-oil droplets. This mechanism is governed by the competition between (i) viscous/shear stresses, (ii) interfacial tension at the interface, and (iii) inertial effects (Figure 2.5).

In microfluidic droplet generators, the breakup regime is commonly classified using the following dimensionless numbers:

- **Reynolds number** (inertia-to-viscous ratio):

$$Re = \frac{\rho U D_h}{\mu} \tag{2.11}$$

  where ρ is the fluid density, U is a characteristic velocity, D_h is the hydraulic diameter, and μ is the dynamic viscosity. In most droplet microfluidic systems, $Re \ll 1$ (or at most moderately low), hence inertia is typically not dominant.

- **Capillary number** (viscous-to-interfacial tension ratio):

$$Ca = \frac{\mu_c U_c}{\gamma} \tag{2.12}$$

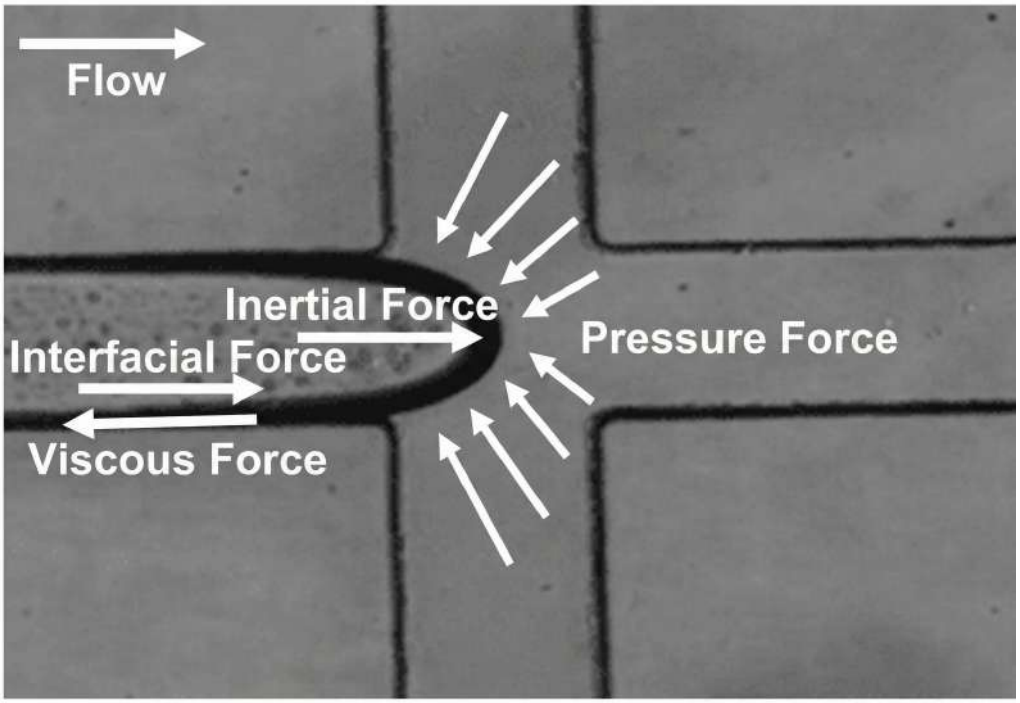

Figure 2.5: Illustration of droplet formation in a T-junction microfluidic channel, showing the necking and pinch-off process driven by shear stress and interfacial tension.

where μ_c and U_c are the viscosity and characteristic velocity of the *continuous phase*, and γ is the interfacial tension between the two phases. Ca is often the key parameter determining the T-junction droplet generation regime: for small Ca, interfacial tension dominates and droplets form in the "squeezing" regime; as Ca increases, the regime transitions toward "dripping" and may ultimately reach "jetting".

- **Viscosity ratio**:

$$\lambda = \frac{\mu_d}{\mu_c} \tag{2.13}$$

where μ_d is the dispersed-phase viscosity. The viscosity ratio affects the neck-thinning dynamics and droplet size.

- **Weber number** (inertia-to-interfacial tension ratio):

$$We = \frac{\rho U^2 D_h}{\gamma} \tag{2.14}$$

In microfluidic droplet generation, We is usually very small, so the dynamics are mainly governed by viscosity and interfacial tension.

Near the junction, droplet formation occurs when the shear stress and pressure increase imposed by the continuous phase become large enough to overcome the restoring effect of

interfacial tension. In an order-of-magnitude sense, the shear stress can be written as:

$$\tau \sim \mu_c \dot{\gamma} \tag{2.15}$$

where $\dot{\gamma}$ is a characteristic shear rate near the interface. The effect of interfacial tension is commonly represented by the Laplace pressure:

$$\Delta p_\gamma = \gamma \left(\frac{1}{R_1} + \frac{1}{R_2} \right) \tag{2.16}$$

where R_1 and R_2 are the principal radii of curvature of the interface. Pinch-off occurs when the hydrodynamically induced pressure and deformation drive the neck radius toward a critical thinness such that the balance with Δp_γ can no longer be maintained.

In the "squeezing" regime (often observed for $Ca \lesssim 10^{-2}$), droplet size depends strongly on the flow-rate ratio of the dispersed to continuous phase. A widely used empirical scaling for T-junction/flow-focusing geometries is:

$$\frac{L}{w} = 1 + \alpha \frac{Q_d}{Q_c} \tag{2.17}$$

where L is the droplet length (along the main channel), w is the main-channel width, Q_d is the dispersed-phase flow rate, Q_c is the continuous-phase flow rate, and α is a geometry-dependent constant (typically $\mathcal{O}(1)$). This relation indicates that increasing Q_d/Q_c increases the droplet volume, whereas increasing Q_c (at fixed Q_d) reduces droplet size and increases the droplet generation frequency.

The droplet generation frequency f can be estimated from dispersed-phase flow conservation:

$$f \approx \frac{Q_d}{V_{\text{drop}}} \tag{2.18}$$

where V_{drop} is the droplet volume, which can be approximated from the droplet dimensions and channel cross-section.

The fundamental mechanism of droplet formation in T-junction microchannels has been systematically characterized [67]. Strategies to overcome Poisson statistics limitations in single-cell encapsulation have been developed [68]. The principle of cell encapsulation in droplets in microfluidics is based on the creation of microdroplets containing cells, formed when the dispersed phase (containing cells) is fragmented by the flow of the continuous phase in microfluidic channels [66]. Differences in velocity, pressure, and shear force at the intersection of the flows lead to the separation of the dispersed phase into droplets of uniform size. Each droplet acts as an isolated "micro-reactor," capable of encapsulating one or a few cells in a sealed microfluidic environment, preventing mixing between units and ensuring independence in analysis [69]. This mechanism allows precise control of the number of cells in each droplet, facilitating single-cell level studies,

applications in cell culture, functional screening, and high-speed biological analysis.

In this study, the T-shaped channel structure was selected for its suitability for the goal of creating uniform droplets. The T-shaped flow-focusing channel has a fast and stable droplet formation rate, producing droplets of uniform size, ideal for the droplet encapsulation process. The channel dimensions were optimized to match the ratio of CTC cell diameter to droplet width, ensuring efficient cell detection and counting. With droplet-to-particle size ratios that are too small, droplet detection becomes more difficult; similarly, if the channel size is too small, it poses challenges in the machining process and droplet formation within the channel. The main channel is designed with a width of 300 μm, a continuous phase channel of 100 μm, and a dispersion phase channel of 100 μm. The detailed design and actual dimensions of the cell packaging system are illustrated in Figure 2.6, which depicts the T-junction configuration where the dispersed phase intersects with the continuous phase to generate droplets.

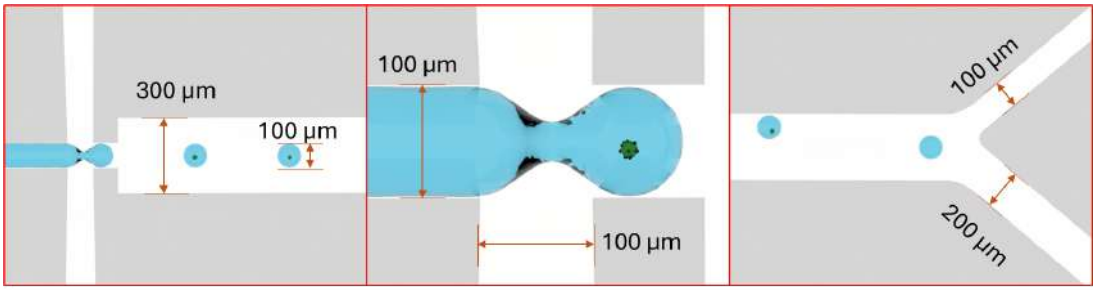

Figure 2.6: Detailed design of the cell packaging system in microdroplets.

2.1.5 Theoretical basis of impedance sensors and microelectrode structure design

Before presenting the sensor design, this report outlines several theories that can be used to design a microfluidic sensor based on capacitive principles. The Coulter principle, first introduced in 1956 [70], forms the basis for modern impedance-based cell counting. In general, there are many methods for fabricating a microfluidic sensor; however, due to the relatively complex fabrication methods, this report uses a simpler measurement method, based on changes in the electrical properties of the electrical and mechanical structures, and calculates the resulting data. These theories will be developed in an ideal environment, assuming no external influences. The theory of flat capacitors is outlined in the next section of the report. An important advantage of microfluidic devices is their ability to significantly reduce the volume of liquid required for chemical and biomolecular diagnostics. They allow liquid manipulation on the external surface of a semiconductor substrate or silicon substrate, providing a particularly flexible approach to liquid handling in the nanoliter range.

Capacitive sensors are often a good choice for detecting objects because of their non-invasive detection method, high sensitivity, and suitability for conductive or insulating liquids [71]. High-speed microfluidic impedance cytometry has been successfully applied for label-free leukocyte differentiation [72], and multi-frequency impedance analysis enables the extraction of detailed cellular properties beyond simple sizing [73]. High-frequency impedance measurements can reveal subcellular morphological features [74]. These advantages have been exploited to measure liquid volume, mass loss due to evaporation, micro-dimensions, liquid fill levels, different multi-layer materials, contact angles and droplet velocity in electric propulsion engines, and surface tension and chemical composition of small liquid volumes. Most of these sensors require an external impedance analyzer, making it difficult to integrate directly into a small microfluidic device. Flat electrode arrays can provide a more compact design that is geometrically optimized. Developed by Coney, further studies have shown that the use of integrated electrode arrays can significantly increase the capacitive signal, which is important when testing and analyzing the composition of a small liquid volume or diluted concentration. The implementation of interconnected arrays comprising metal electrodes with uniform width has been explored by several research groups. These configurations are best suited for homogeneous dielectric environments (Figure 2.7).

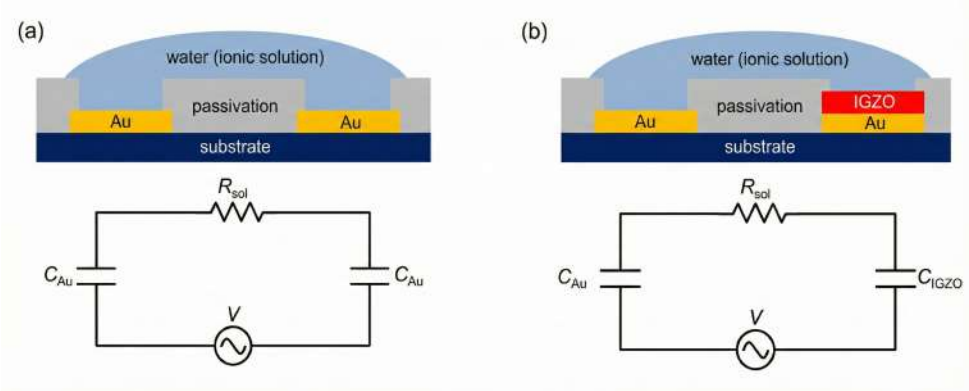

Figure 2.7: Structure and equivalent circuit of the device fabricated based on planar electrodes used for impedance measurements with gold electrodes.

The focus of the work is the design and development of capacitive sensors that can be directly integrated with current liquid-based technology platforms. The selected design allows the electrode arrays to be used as resistive heating devices to activate thermometers or as capacitive sensors for liquid detection and analysis. The electrode array must be designed to maximize the capacitive signal when handling liquid structures with uneven heights, such as small droplets or gaps. Analysis of the electric field distribution corresponding to a pair of parallel electrodes, the electrode terminals are used to illustrate the importance of penetration depth and effective electrode width in designing a suitable sensor layout for use with small, non-uniformly thick liquid volumes. The proposed design

demonstrates a trade-off between high signal-to-noise ratio and high spatial resolution.

In this study, electrical conductivity is obtained through numerical calculations, and this conductivity value is used to determine impedance. Electrical conductivity is defined as:

$$Y = \frac{1}{Z} \tag{2.19}$$

where Y represents the input conductance (S) and Z represents the impedance (Ω).

Resistance measures the degree of opposition of a circuit to a steady current. On the other hand, electrical impedance includes both resistive and dynamic factors, often referred to as electrical reactance. Similarly, electrical conductivity not only evaluates the degree of transmission of a steady current but also considers dynamic characteristics related to the material's sensitivity to polarization:

$$Y \equiv G + jB \tag{2.20}$$

Here, G is the electrical conductivity (S)—measuring the circuit's ability to conduct electricity, B is the susceptance (S)—reflecting the circuit's ability to store electric or magnetic field energy, and j is the imaginary unit where $j^2 = -1$.

The basic resistance is influenced by both the conductivity of the solution and the position of the object in the channel. The relationship between conductivity and impedance can be expressed as follows:

$$Z = R + jX = Y^{-1} = \frac{1}{G + jB} = \frac{G - jB}{G^2 + B^2} \tag{2.21}$$

where R is the resistance, and X is the reactance of the circuit.

Figure 2.8 shows the internal structure of a flat capacitive sensor, illustrating how the electric field is formed between the positive and negative electrodes. Gold (Au) is widely used as sensor electrodes for biomedical applications due to its biocompatibility. Gold is also a much better conductor than aluminum, copper, or even silver. This has been established, and the conductive surface of gold may be ideal for many biosensing applications, including monitoring bacterial growth, detecting viruses, and detecting DNA. Gold layers can be easily fabricated using commercially available photolithography technology on CMOS chips using low-temperature compatible microfabrication methods.

Gold electrode structures are a specialized design used in many microelectronic and microfluidic systems. Gold electrodes are fabricated from thin gold layers, typically deposited onto substrate surfaces using methods such as physical vapor deposition (PVD), sputtering, or electrodeposition. This gold layer has an optimal thickness to ensure high conductivity, a stable surface, and compatibility with modern microfabrication techniques. The gold electrode structure typically includes a contact system, a conductive region, and a main electrode region. The contact system is designed as large pads that connect

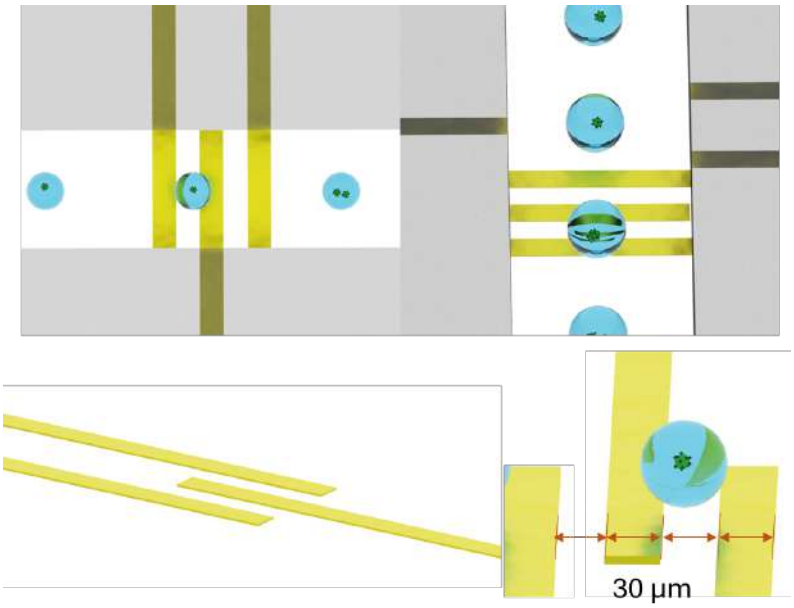

Figure 2.8: Microchannel structure for cell detection and counting using an integrated impedance sensor in a Lab-on-a-chip.

the electrode to peripheral components such as control circuits or signal measurement probes. These contact pads are typically large enough to reduce contact resistance and ensure mechanical durability during use. The conductive area consists of thin metal lines of appropriate width to maintain conductivity without significantly increasing resistance. These paths can be straight, curved, or branched depending on specific design requirements and applications. The main electrode area is where the device's important features are concentrated and can take various forms such as electrode grids, parallel electrodes, or concentrated electrodes to optimize electric field distribution.

The surface of gold electrodes is often specially treated to enhance adhesion to the substrate, minimize oxidation effects, and ensure long-term operability. Surface treatment methods include designing a titanium (Ti) or chromium (Cr) buffer layer between the gold and the substrate to increase adhesion, or using polymer protective layers to limit environmental impact. Thanks to these special design features, gold electrode structures can maintain stable performance and meet the high technical requirements of advanced microcircuit and microelectronic systems.

The impedance measurement electrode system is a specialized microelectronic design that determines the electrical characteristics of the environment using the impedance measurement method (Figure 2.8). This design includes 3 electrodes to create differential measurement pairs. Using 3 electrodes allows for differential measurement, which minimizes noise, optimizes accuracy, and ensures uniform electric field distribution in the measurement area. These electrodes are typically made of gold (Au) due to its excellent conductivity, oxidation resistance, and stable measurement performance.

The structure of this system is divided into three main regions. The electrode contact

region is where the electrode connects to the measurement system, ensuring stable contact between the circuit and the measurement source. The contact region is typically larger to reduce contact resistance and maintain long-term durability. The conductive region is the intermediate part between the contact region and the measurement region, often in the form of narrow conductive paths, helping to control the current and optimize the voltage distribution across the electrodes. Finally, the main measurement region contains 3 electrodes placed parallel with precise spacing, ensuring the most accurate impedance measurement by creating a uniform electric field.

The design of these electrodes has important features to ensure high measurement performance. The electrodes are typically thin parallel bars, which help create a linear electric field, minimizing the effects of contact resistance and electrical noise. This design allows for the creation of differential measurement pairs, which helps achieve higher measurement accuracy, especially in microenvironments. The electrodes are typically placed on an insulating substrate, such as silicon dioxide (SiO_2), glass, or PDMS polymer, which isolates the electrodes from the surrounding environment and ensures signal stability. To enhance adhesion between the electrodes and the substrate, a titanium (Ti) or chromium (Cr) buffer layer is often deposited before gold or platinum coating. The electrode was also designed to ensure uniform electric field distribution, enabling impedance measurements to achieve the highest accuracy. This structure minimizes the impact of contact resistance on impedance measurements while ensuring higher accuracy and stability compared to traditional single-pair electrode systems.

2.1.6 Theoretical Basis for droplet sorting using dielectrophoresis (DEP)

After detecting and encapsulating cells in droplets, the next step is to sort and separate the droplets based on specific criteria. Dielectrophoresis is a widely used technique for manipulating particles and droplets in microfluidic systems due to its label-free nature and high precision. Dielectrophoresis, first described by Pohl in 1951 [75], describes the motion of polarizable particles in non-uniform electric fields. The theoretical framework for electromechanics of particles has been comprehensively established [76], and DEP has emerged as a powerful label-free technique for manipulating biological samples [77]. Fluorescence-activated droplet sorting combines droplet microfluidics with DEP-based manipulation for high-throughput single-cell analysis [78].

Figure 2.9 illustrates the mechanism of microdroplet separation in a microfluidic channel. When a liquid droplet is placed in a microfluidic system under the influence of a direct current (DC) voltage, three primary electrostatic effects act on the droplet: electrostatic potential, dipole-dipole interactions, and dielectric electrostatic potential. Dipole-dipole interactions occur when droplets become polarized, creating an induced dipole moment

with oppositely charged ends. These interactions generate attractive or repulsive forces between droplets without producing a net force on individual droplets, thereby influencing the structure and dynamics of the droplet system, such as droplet chain or network formation. Electrostatic forces arise when electrically charged droplets move in a uniform electric field. This force is proportional to the charge of the droplet and the intensity of the electric field, playing an important role in the separation of cells or particles in a microfluidic system. Dielectric electrostatic forces act on uncharged droplets in a non-uniform electric field and depend on the difference in polarity between the droplet and the surrounding environment.

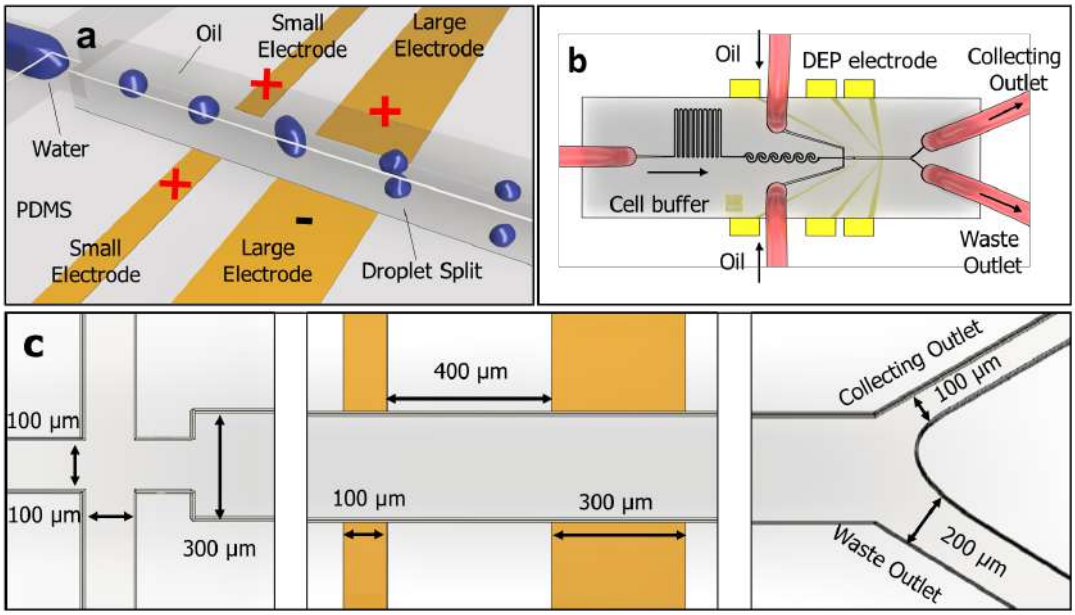

Figure 2.9: Microfluidic droplet classification and separation device. (a) Schematic illustration incorporating gold electrode pairs subjected to different high and low DC voltages with different sizes to achieve both steering and separation effects. (b) Water-in-oil structure designed to generate droplets through flow concentration effect with gold electrode pairs near the two outlets. (c) Dimensions of the inlet, outlet, main channel, and gold electrodes.

In this study, the problem of droplet classification and separation within the same microchannel and electrode structure (Figure 2.9(a)) [79] was addressed. Parameters such as channel width, droplet size, and electrode size are crucial for effectively solving this problem. Figure 2.9(b) illustrates the overall design of the microfluidic channel structure, including two inlets for the continuous phase and dispersed phase to facilitate droplet formation and two outlets to evaluate the droplet classification process, combined with electrodes to generate an electric field. In this proposed design, the droplet formation channel in the microfluidic system employs a flow-concentrating structure, with both the dispersed phase and continuous phase having a width of 100 μm (Figure 2.9(c)), aiming to produce droplets of approximately 100 μm in size. The main channel, with a width

of 300 μm, ensures that the droplets are concentrated in the center and allows for easy observation of EHD effects. The outlet channels, including a collection channel and a discharge channel, have dimensions of 100 μm and 200 μm, respectively. The role of the outlet channels is to evaluate classification efficiency by analyzing droplet control through voltage adjustments, thereby determining the optimal voltage range for effective droplet classification applications. In the absence of an electric field, droplets default to exiting through the discharge channel. The principle of droplet navigation under the influence of DEP force is illustrated in Figure 2.10.

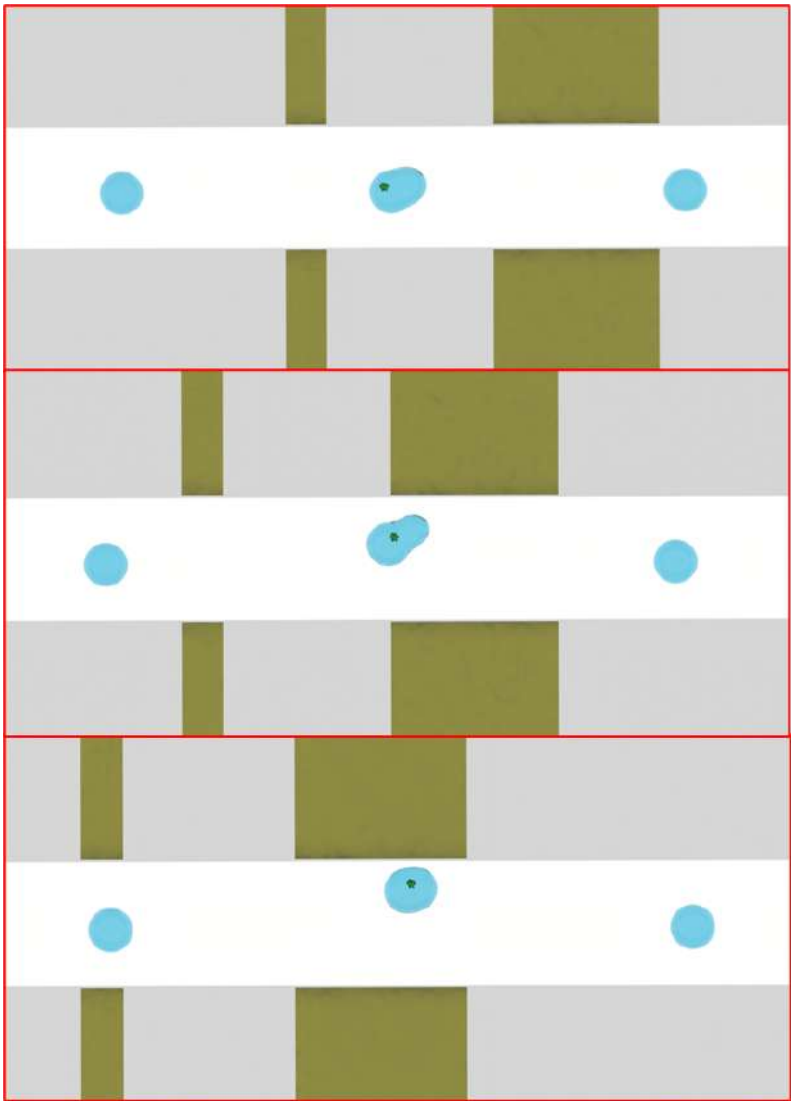

Figure 2.10: Illustration of droplet navigation under the influence of DEP force

In this study, the proposed electrode configuration consists of two pairs of flat electrodes placed outside the microchannel, where one pair is smaller than the other. The droplet does not come into direct contact with the electrodes; instead, the electric field causes a redistribution of charge within the droplet. Due to the use of flat electrodes of different sizes, the electric field generated inside the channel is inherently non-uniform.

The presence of the smaller electrode pair primarily helps deflect the droplet's movement during droplet classification. As the droplet passes through this non-uniform electric field, electrostatic polarization occurs, characterized by the redistribution of charge within the droplet under the influence of the electric field. This polarization process leads to the formation of a double electric layer on the droplet surface. After polarization, the redistribution of surface charge creates unbalanced electrostatic forces, leading to droplet deformation. The operating principle of the proposed microfluidic device is illustrated in Figure 2.11.

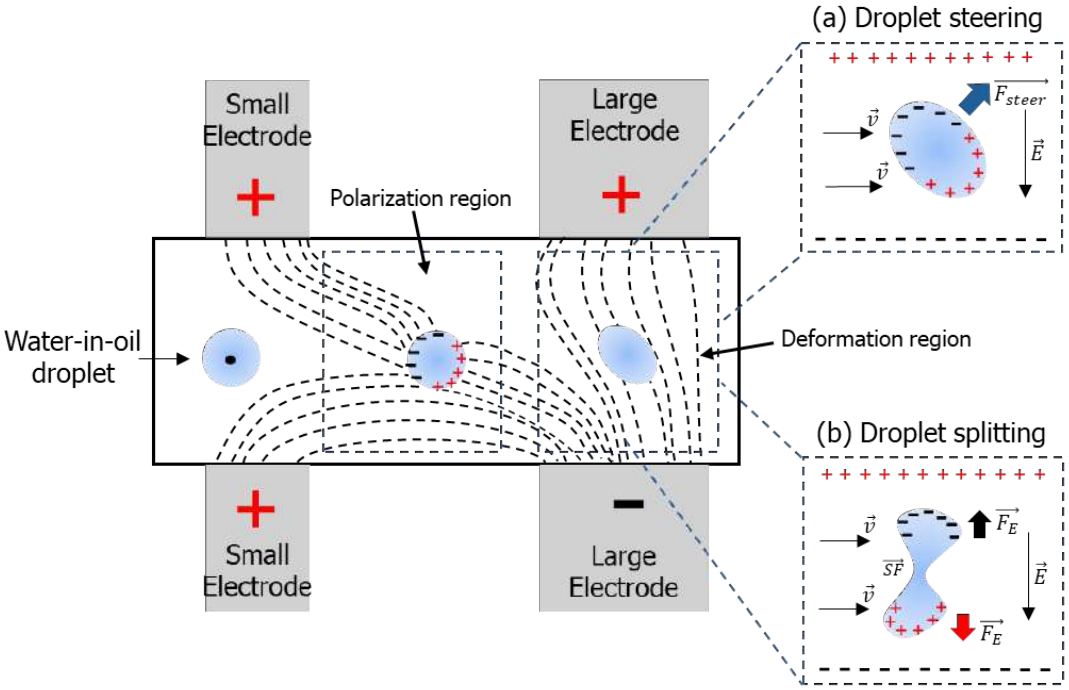

Figure 2.11: Operating principle of the proposed microfluidic device. When a water droplet in oil moves into the region between the small electrode pair and the large electrode pair, electric polarization occurs. As the droplet continues into the electric field created by the large electrode pair (Deformation Zone), two effects may occur depending on the applied voltage: (a) Droplet steering effect—once polarized, the droplet is influenced by the deflecting electrostatic force caused by the non-uniform electric field, altering the droplet's trajectory. (b) Droplet separation effect—when the applied voltage exceeds a threshold, the combination of droplet deformation and shear force caused by flow velocity causes the droplet to break into two smaller droplets.

The motion of the droplet is also influenced by electrohydrodynamic (EHD) effects, which describe the interaction between electric fields and fluid flow [80]. Free charges accumulate on the droplet surface, creating a non-uniform electric field. This field acts electro ically on the molecules on the droplet surface, creating forces described by the Maxwell stress tensor, causing uneven pressure on the droplet surface. As the electric field strength increases, the surface tension of the droplet becomes insufficient to maintain its original shape. When the electrostatic force exceeds the surface tension, the droplet will

be stretched or compressed depending on the characteristics of the electric field.

As the droplet approaches the region with larger electrodes, one of two physical phenomena may occur depending on the voltage applied to the electrodes [81]. In the first effect, when a certain voltage is applied, the combination of flow velocity and dielectric electrostatic force due to the non-uniform electric field causes the droplet to deviate from its initial linear trajectory. By adjusting the applied voltage, the degree of trajectory deviation can be linearly controlled within a certain range, allowing flexible application in droplet classification. Conversely, when the voltage is increased to a sufficiently high level, the combination of droplet deformation, the stretching force at both ends of the droplet caused by the electric field, and the shear force of the liquid flow leads to droplet separation. Therefore, by adjusting the voltage applied to the proposed electrode structure and microfluidic channel, two droplet control techniques can be achieved without the need for complex electrode configurations or large microfluidic spaces.

In this study, the Navier–Stokes equations describing fluid flow, combined with the Maxwell equations describing electrostatic phenomena, are formulated within the framework of the finite element method (FEM). These equations account for the incompressibility of the fluid, the interaction between the electric field and fluid flow, as well as the influence of surface tension:

$$\nabla \cdot v = 0 \tag{2.22}$$

$$\frac{\partial v}{\partial t} + (v \cdot \nabla)v = -\nabla p + \mu \nabla^2 v + f_{ST} + f_E \tag{2.23}$$

In these equations, v is the fluid velocity vector, p is the pressure, μ is the dynamic viscosity, f_{st} represents the surface tension force, and f_E denotes the electric force. The surface tension force f_{st} plays a crucial role in the behavior of the interface surface and is calculated based on the curvature of the interface κ and the surface tension coefficient γ.

$$f_{ST} = \gamma \kappa n \tag{2.24}$$

n is the unit normal vector at the interface surface. The electric force f_E is determined from the divergence of the Maxwell stress tensor σ_M:

$$f_E = \nabla \cdot \sigma_M \tag{2.25}$$

where the Maxwell stress tensor σ_M in static electricity is defined by:

$$\sigma_M = \epsilon \left(EE - \frac{1}{2} E^2 I \right) \tag{2.26}$$

where ϵ is the dielectric constant of the liquid, E is the electric field vector, and$E^2 = E \cdot E$ is the dot product of the electric field vector with itself, representing the square of

the electric field magnitude. I is the unit tensor.

The level-set method is used to track the interface surface between two liquid phases. The functionϕ varies continuously on the interface surface, allowing for accurate calculation of the forces acting on the interface. The level-set equation is expressed as follows:

$$\frac{\partial \phi}{\partial t} + \nabla \cdot (v\phi) = \chi \nabla \cdot \left(\Psi \nabla \phi - \phi(1-\phi) \frac{\nabla \phi}{|\nabla \phi|} \right) \tag{2.27}$$

Where ϕ is the level-set function, χ is the rescaling parameter, Ψ controls the thickness of the interface surface, and $\nabla \cdot (v\phi)$ represents the convection of the level-set function with respect to the fluid velocity. Hydrodynamic properties such as density ρ and viscosity μ are determined based on the level-set function, where ρ_1 and ρ_2 are the densities of the two liquid phases.

$$\rho = \rho_1 + (\rho_2 - \rho_1)\phi \tag{2.28}$$

$$\mu = \mu_1 + (\mu_2 - \mu_1)\phi \tag{2.29}$$

After the control equations are established, the system of equations is assembled and solved using numerical methods. The numerical calculation results are visualized and analyzed to understand the behavior of the droplets, including their trajectories, deformation, and interaction with the electric field. The electrostatic module is used to simulate the electric field in materials, combining spatial charge density to describe the electrostatic force acting on leaky dielectric materials.

The electrostatic forcef_c acting on leaky dielectric materials can be described through the divergence of the Maxwell stress tensor, which quantifies the force exerted by the electric field on the dielectric fluid. This force results from the interaction between the electric field and the dielectric properties of the material. The detailed formula for this force is expressed by the following equation:

$$f_c = q\mathbf{E} - \frac{1}{2}E^2 \nabla \epsilon + \frac{1}{2}\nabla \left[E^2 \rho \frac{\partial \epsilon}{\partial \rho} \right]_T \tag{2.30}$$

Where $\nabla \epsilon$ is the gradient of the dielectric constant, and q is the charge density. The charge density q and its influence on the electrostatic force also play an important role in electrohydrodynamic (EHD) simulations. The charge density is determined by the following formula:

$$q = \nabla \cdot (\sigma \mathbf{E}) - \nabla \cdot (\epsilon \mathbf{E}) \tag{2.31}$$

Where σ is the electrical conductivity of water, and ϵ is the relative permittivity. This equation ensures that the charge distribution is accurately described, influencing the

electrostatic forces in the fluid.

2.2 Simulation modeling

2.2.1 Simulation of magnetic separation using the cavity-integrated structure

The structure of the proposed microchip is illustrated in Figure 2.12. The geometric shape of the channel is designed according to the cavity model. In the meandering channel, the uneven flow pushes the cells toward the outer wall of the channel, where the trap chambers are located. A comparison between particle concentration in Newtonian fluid in a meandering channel and viscoelastic fluid in a straight channel shows that the meandering channel allows for more efficient particle concentration in viscoelastic fluid.

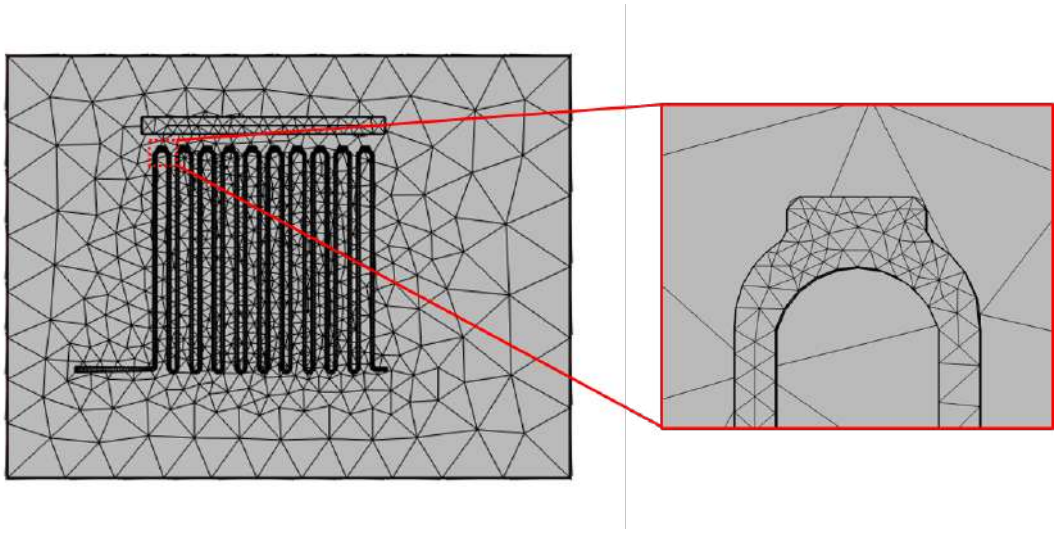

Figure 2.12: Simulation mesh model of the proposed cavity microfluidic device.

In this study, the chambers were designed with right angles to facilitate the capture of target cells. The operating principle of the proposed magnetic separation system involves the magnetic interaction created between an external magnetic field and magnetic particles fixed on the target cells. A permanent magnet (N35 magnet) is used to generate a magnetic field within the microfluidic channel area. Target cells with magnetic particles are attracted toward the regions of the magnet and thus captured at the corners of the square compartments, while non-target cells are carried away by the fluid flow.

The magnetic cell separation performance of the proposed structure was tested through numerical calculations using COMSOL Multiphysics software. The AC/DC and CFD modules were selected to determine the magnetic field and particle trajectory in a two-dimensional model. The model was built based on the shape and parameters of the actual prototype. A neodymium magnet was applied to generate the magnetic field in the model.

Table 2.1: Parameters used in the simulation study

Parameter	**Value**
Cell radius (r_c)	7.5 μm
Particle radius (r_b)	0.75 μm
Flow rate (q)	5 μL/min
Relative permeability of the particle	4.1
Relative permeability of the liquid	1
Residual magnetic flux density of N35 magnet	1.2 T
Length of N35 magnet	20 mm
Magnet height N35	5 mm

The dimensions and related electrical parameters are listed in Table 2.1.

2.2.2 Simulation of the Inertial Spiral Microchannel

In order to investigate the hydrodynamics of the Dean flow and optimize the cell focusing efficiency within the proposed continuous spiral structure, a comprehensive three-dimensional (3D) numerical simulation was conducted. The computational model was developed using COMSOL Multiphysics 6.1, leveraging the *Computational Fluid Dynamics (CFD)* and *Particle Tracing* modules. This section details the model construction, domain discretization, and the governing physical principles applied during the simulation.

Geometric Construction and Domain Discretization

The 3D geometry of the microchannel was constructed to match the experimental design dimensions exactly. As illustrated previously, the channel consists of a sequence of spiral loops with progressively decreasing radii of curvature to induce a gradient of Dean forces.

Discretizing the continuous domain into a discrete mesh is a critical step in Finite Element Method (FEM) analysis, directly influencing both the accuracy of the solution and the computational cost. For inertial microfluidics, capturing the secondary flow patterns (Dean vortices) that develop perpendicular to the main flow direction requires a high-quality mesh, particularly in the curved regions where velocity gradients are significant.

Figure 2.13 presents the meshing strategy applied to the inertial spiral microchannel.

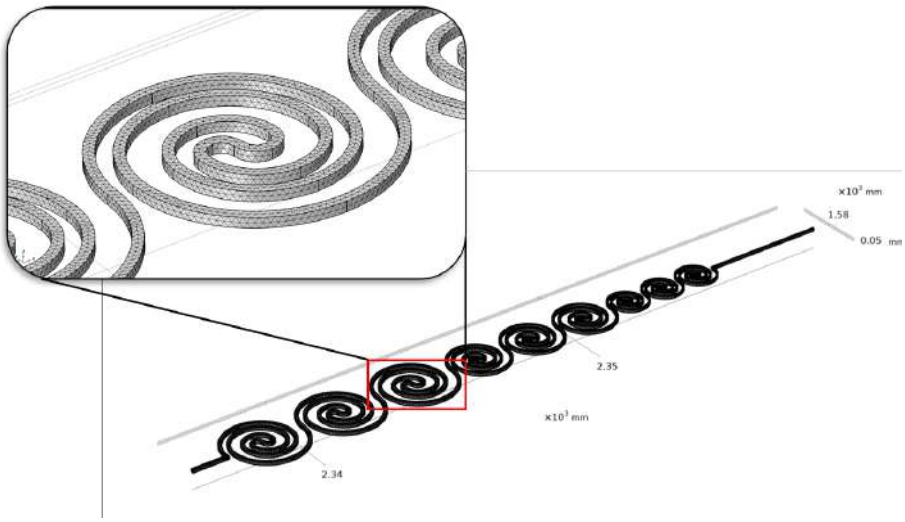

Figure 2.13: Finite element mesh generation for the 3D spiral microfluidic model. The overview shows the full channel geometry comprising the large, middle, and small spiral sections. The inset (zoom-in view) highlights the refined tetrahedral mesh elements applied to the curved channel walls to accurately resolve the boundary layer and secondary Dean flow vortices.

The domain was discretized using an unstructured grid composed primarily of free tetrahedral elements. To optimize the computational efficiency while maintaining high accuracy in critical regions, a user-controlled meshing sequence was implemented with the following characteristics:

- **Curvature Refinement:** As observed in the magnified inset of Figure 2.13, the mesh density is significantly increased in the spiral sections. The curvature factor was set to a lower value to ensure that the mesh elements accurately approximate the curvilinear geometry of the channel walls, preventing numerical diffusion errors that could dampen the calculated Dean velocity magnitude.

- **Boundary Layer Meshing:** To accurately resolve the steep velocity gradients near the channel walls (where the wall-induced lift force F_{LW} is dominant), a boundary layer mesh was applied. This consists of dense, prismatic elements stacked along the wall boundaries, transitioning to tetrahedral elements in the bulk flow.

- **Mesh Independence Study:** A grid independence test was performed by varying the number of mesh elements from coarse ($< 10^5$ elements) to extremely fine ($> 2 \times 10^6$ elements). The chosen mesh, depicted in Figure 2.13, represents the optimized configuration where further refinement resulted in less than a 2% variation in the maximum fluid velocity and particle trajectory deviations.

Governing Physics and Equations

The simulation was decoupled into two steps: a stationary study for the fluid flow field and a time-dependent study for particle tracking.

Fluid Dynamics (Laminar Flow) The fluid flow within the microchannel is governed by the continuity equation and the Navier-Stokes equations for an incompressible Newtonian fluid. Given the micro-scale dimensions and the operating flow rates, the flow remains within the laminar regime ($Re < 2000$). The governing equations solved by the *Laminar Flow (spf)* interface are:

$$\nabla \cdot \mathbf{u} = 0 \tag{2.32}$$

$$\rho(\mathbf{u} \cdot \nabla)\mathbf{u} = \nabla \cdot \left[-p\mathbf{I} + \mu(\nabla\mathbf{u} + (\nabla\mathbf{u})^T)\right] \tag{2.33}$$

Where $\mathbf{u}$ denotes the fluid velocity vector, p is the pressure, ρ is the density of the fluid medium (approximated as water, $\rho = 1000\ kg/m^3$), and μ is the dynamic viscosity ($\mu = 0.001\ Pa \cdot s$). The inertial terms $(\mathbf{u} \cdot \nabla)\mathbf{u}$ were strictly retained in the solver settings to ensure the capture of inertial effects essential for this separation mechanism.

Particle Dynamics (Particle Tracing) Once the steady-state flow field was established, the *Particle Tracing for Fluid Flow (fpt)* interface was used to calculate the trajectories of the cells. The motion of the cells is described by Newton's second law:

$$\frac{d(m_p\mathbf{v})}{dt} = \mathbf{F}_D + \mathbf{F}_L + \mathbf{F}_g \tag{2.34}$$

Where m_p is the particle mass, $\mathbf{v}$ is the particle velocity, and the forces include the Stokes Drag force ($\mathbf{F}_D$), the Inertial Lift force ($\mathbf{F}_L$), and the Gravitational force ($\mathbf{F}_g$). In this model, the wall-induced lift and shear-gradient lift forces were incorporated to simulate the equilibrium positioning of cells.

Boundary Conditions

Appropriate boundary conditions were applied to replicate the experimental setup:

- **Inlet:** A *Laminar Inflow* boundary condition was applied, defined by a specific flow rate (Q). Simulations were swept across a range of flow rates corresponding to Reynolds numbers $Re_c = 10$ to 100 to identify the optimal focusing regime.
- **Outlet:** A *Pressure* boundary condition with $p = 0\ Pa$ was set at the channel outlet to suppress backflow effects.
- **Walls:** A *No Slip* condition ($\mathbf{u} = 0$) was applied to all inner walls of the channel.

The simulation results, specifically the velocity profiles and particle focusing positions derived from this model, provide the theoretical validation for the design parameters selected for the fabrication process.

2.2.3 Simulation of the microfluidic impedance sensor

To evaluate the performance of the complex impedance measurement technique on a flat copper electrode substrate proposed by the research group, a simulation model was constructed. In the experimental design, the microelectrode structure consists of four electrodes, forming two differential electrode pairs, to facilitate signal recording and processing. In the simulation, to simplify the structure, the model was reduced to two flat electrodes with different sizes to record impedance changes. For calibration purposes, the model was used to calculate the impedance differences of buffer solutions containing different cell types, thereby enabling the identification of differences between cell types within the same population, such as distinguishing cancer cells from benign cells. These results demonstrate differences in electrical signals between cell lines and confirm that the proposed electrode structure is applicable for detecting and quantifying A549 lung cancer cells.

a) ***Single shell model***

Figure 2.14 shows the core model with a single shell, consisting of a conductive sphere in the cytoplasm and a shell of electric charges in the cell membrane, which is widely used to analyze electrical impedance measurements. The complex permeability in cell suspensions is often modeled using Maxwell's mixed theory. The complex permeability of the synthetic cell mixture, denoted as $\widetilde{\varepsilon}_{mix}$, is calculated as follows:

$$\widetilde{\varepsilon}_{mix} = \widetilde{\varepsilon}_m \frac{1 + 2\phi \widetilde{f}_{CM}}{1 - \phi \widetilde{f}_{CM}} \tag{2.35}$$

Here, $\widetilde{\varepsilon}_{mix}$ is the complex permeability of the cell mixture and suspension medium, and$\widetilde{\varepsilon}_m$ is the complex permeability of the cell. Additionally, ϕ represents the volume fraction of the cell relative to the suspension medium, and $\widetilde{f}_{CM}$ denotes the Clausius–Mossotti coefficient:

$$\widetilde{f}_{CM} = \frac{\widetilde{\varepsilon}_p - \widetilde{\varepsilon}_m}{\widetilde{\varepsilon}_p + 2\widetilde{\varepsilon}_m} \tag{2.36}$$

Furthermore, the geometric properties of the electrode arrangement and the electrical impedance of the integrated system can be expressed as follows:

$$\widetilde{Z}_{mix} = \frac{1}{j\omega \widetilde{\varepsilon}_{mix} G_f} \tag{2.37}$$

where ω denotes the frequency of the electric field and G_f is a constant determined solely by the shape of the sensor region.

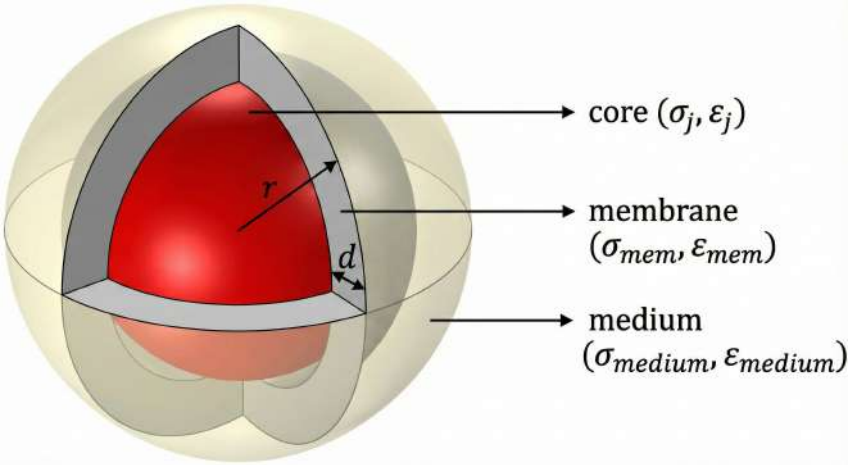

Figure 2.14: The core-shell model for the cell model

b) ***Simulation of the sensor structure***

A simulation model for testing the characteristic electrical signals of lung cancer cells is designed to include a sensor structure comprising a straight channel with two sensor electrodes (Figure 2.15).

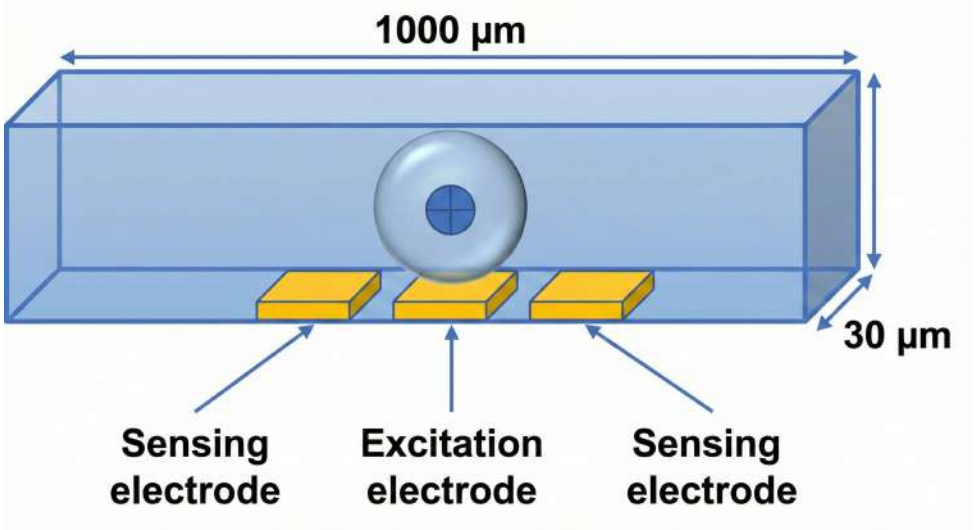

Figure 2.15: Proposed sensor structure model

In the simulation, the structure modeled the configuration of each cell passing through two electrodes integrated into a microchannel, where one electrode was supplied with a 1 V excitation voltage signal and the other was grounded. PBS 0.1X solution was used as the buffer solution. Other parameters used in the simulation, as well as the electrical characteristics of the two types of cancer cells and other blood cells, are presented in the table.

Table 2.2: Geometric parameters in the simulation model

Symbol	**Description**	**Size (μm)**
L	Microchannel length	1000
H	Microchannel height	30
W	Microchannel width	30
D	Electrode length	30
R_1	Electrode width	30
R_2	Electrode width *	15
R_c	Cell radius	7.5

Table 2.3: Some material parameters used in the simulation

Material	**Permittivity**	**Conductivity (S/m)**
Air	1	10^{-15}
PDMS	2.75	4×10^{-15}
Glass	5.5	10^{-15}
PBS 0.1X	80	0.055

In an electrically conductive medium, at a point, Ohm's law states that:

$$J = \sigma E + J_e \tag{2.38}$$

Where σ is the electrical conductivity (S/m) and J_e is the externally applied current density (A/m^2).

At equilibrium, the steady-state electric field in a conductive medium is described by the simplified steady-state continuity equation as follows:

$$\nabla \cdot J = Q_{j,v} \tag{2.39}$$

where $Q_{j,v}$ is the current source.

In the case of a static system, the relationship between the potential V and its gradient E can be determined as follows:

$$E = -\nabla V \tag{2.40}$$

where E is the electric field (V/m) and it also has characteristics similar to the classical gravitational field.

At the insulator node locations, boundary conditions are established in the simulation. These boundary conditions mean that no current can flow across the boundary, and the discontinuous voltage across the boundary is represented as in equation (2.41). Additionally, the boundary environment of the entire model is designed as a sphere and filled with air.

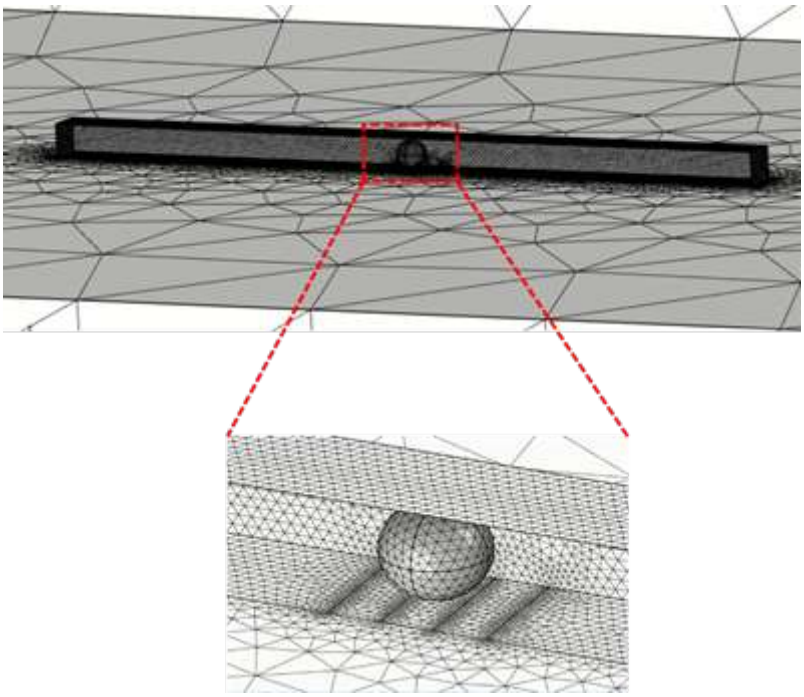

Figure 2.16: Mesh used in the simulation

$$\mathbf{n} \cdot J = 0 \tag{2.41}$$

This condition can be applied at symmetric boundaries where the potential is expected to exhibit symmetry. It is important to note that this insulating condition does not apply to internal boundaries. As described in Figure 2.16, a specially refined triangular mesh was created to increase the element density around the electrode surfaces, including both the stimulating electrode and the sensing electrode, resulting in a higher number of elements compared to other regions in the channel.

c) ***3-electrode impedance measurement circuit principle***

The impedance measurement system is designed based on a differential detection scheme using a three-electrode configuration. In this setup, the central electrode functions as the excitation source, driven by an AC voltage signal $V(t) = V_0 \sin(\omega t)$, while the two adjacent electrodes serve as differential sensing terminals. This symmetrical arrangement is critical for minimizing baseline drift and common-mode noise, which are prevalent in high-sensitivity microfluidic measurements.

The equivalent circuit for signal processing typically consists of two Transimpedance Amplifiers (TIAs) followed by a differential amplifier and a Lock-in Amplifier (LIA). The current signals I_1 and I_2 flowing through the two sensing electrodes are first converted into voltage signals V_1 and V_2 by the TIAs. Since the impedance of the fluid channel is high, the currents are in the nano-ampere to micro-ampere range, requiring high-gain, low-noise amplification. The differential voltage $\Delta V = V_1 - V_2$ is then extracted.

When the microchannel is filled only with the buffer solution, the electrical impedance between the excitation electrode and the two sensing electrodes is balanced, resulting in a near-zero differential output. As a cell traverses the detection region, it sequentially alters the impedance of the first and then the second sensing path. This disturbance generates a characteristic bipolar Gaussian-shaped signal in the time domain. The peak-to-peak amplitude of this signal correlates with the cell size, while the phase shift provides information regarding the cell membrane capacitance and cytoplasmic conductivity. The use of a Lock-in Amplifier allows for the precise demodulation of these in-phase (real) and quadrature (imaginary) components at the specific excitation frequency, ensuring high measurement accuracy even in noisy environments.

Applying impedance measurement methods to biological targets presents unique challenges that require adherence to specific circuit design constraints, particularly within microfluidic environments. primarily, the measurement voltage applied across the electrodes must be limited to prevent detrimental effects on biological samples. Typically, the excitation voltage in biosensors ranges from tens to hundreds of millivolts (mV) [35]. Due to the minute magnitude of these signals, the system is highly susceptible to noise, especially in sensors employing microelectrode structures.

To address this issue, a Lock-in amplifier circuit was designed for the impedance measurement system (Figure 2.17). In this design, the Lock-in amplifier is configured to operate within a frequency range of 10 kHz to 200 kHz. The current flowing through the sensor is fed back to the output via a transimpedance configuration. The output signal is subsequently directed to the lock-in amplifier stage, which utilizes an AD630 IC acting as a synchronous demodulator (multiplier). The lock-in amplifier functions as a high-Q filter; the signal is amplified only when its frequency precisely matches the reference frequency, while signal components at other frequencies are treated as noise and attenuated. The output of the lock-in amplifier is derived from the in-phase (0°) and quadrature (90°) components of the input signal relative to the reference signal.

Following the lock-in amplification stage, the signal is digitized by an Analog-to-Digital Converter (ADC) and processed by a microprocessor. Sequential measurements can be performed with incremental frequency steps within a programmable range of 10 kHz to 200 kHz. From the real and imaginary components of the signal (U_0 and U_{90}), the total impedance, real impedance, imaginary impedance, phase angle, and equivalent series capacitance are determined.

The specific block diagram of the system for detecting living cells in a liquid flow is illustrated in Figure 2.17. A three-microelectrode impedance chip is mounted on a PCB, allowing for easy detachment and replacement. A sinusoidal excitation signal with an amplitude of 1 V_{p-p} and a frequency of 100 kHz, generated by a function generator, is applied to the excitation electrode area. Sensing signals from the two receiving electrodes are acquired and transmitted to the processing circuit to detect impedance changes

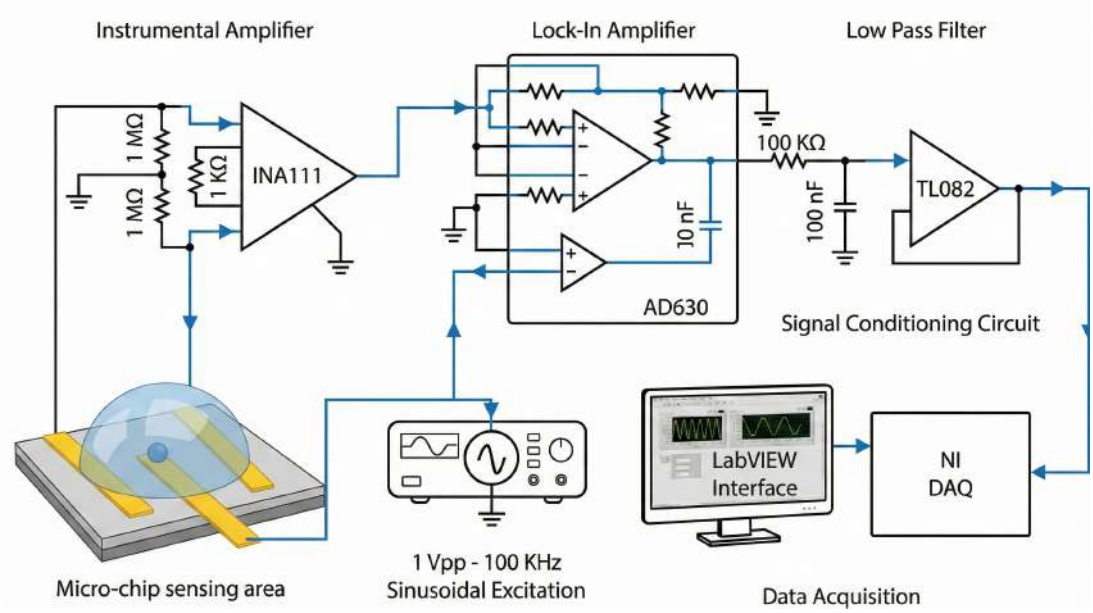

Figure 2.17: Block diagram of the living cell in-flow detection system utilizing differential impedance sensing technique.

between the excitation electrode and the respective receiving electrodes.

The signal processing circuit designed by the research team comprises a high-speed instrumentation amplifier (IC INA111) and a lock-in amplification stage utilizing a high-precision balanced modulator/demodulator IC (AD630 – Analog Devices). Two 1 MΩ resistors (R_1 and R_2) are connected to the inputs of the INA111 as part of a Wheatstone bridge configuration. A 1 kΩ resistor is employed as the gain resistor (R_G) to set the gain of the instrumentation amplifier stage, calculated as:

$$G = 1 + \frac{50\ \text{k}\Omega}{R_G} \tag{2.42}$$

The sinusoidal excitation signal supplied to the central electrode serves as the reference signal for the AD630 lock-in amplifier, facilitating the rejection of common-mode noise and unwanted background signals. The signal obtained after lock-in amplification is conditioned by a passive low-pass filter ($R = 100$ kΩ, $C = 100$ nF) and a voltage buffer utilizing a TL082 IC before being transmitted to an external data logger via an SMA connector.

A regulated DC power supply of ±12 V is used to power the signal processing circuit. The sinusoidal excitation signal is controlled by a function generator (Agilent 33220A, Agilent Technologies, Inc., Palo Alto, CA, USA). The processed signal is recorded using a National Instruments DAQ unit (NI-4431) at a sampling rate of 1 kHz and subsequently transferred to a computer via a digital interface (GPIB-USB-HS, National Instruments, Austin, TX, USA). Data is then processed and visualized using LabVIEW software.

The motion of the cell samples within the microchannel is observed and recorded using

an inverted fluorescence microscope (Model CKX41, Olympus, Tokyo, Japan) equipped with a CCD camera (DP71, Olympus, Tokyo, Japan) connected to a computer running Olympus DP image control software. Microscope images are displayed directly on the screen and recorded to validate the signal results obtained from the circuit. The excitation signal is applied to the central electrode, while the reference signal is utilized for the lock-in amplification process. The output voltage is transmitted to the NI 4431 DAQ for data acquisition.

2.2.4 Simulation of droplet sorting based on electric DEP

The finite element method (FEM) is a widely used numerical technique for solving complex problems in electrohydrodynamics (EHD), providing a powerful simulation framework for sophisticated phenomena such as droplet steering and separation. EHD involves the interaction between fluid flow and electric fields, leading to phenomena that are extremely sensitive to the properties of the fluid as well as the applied electric field. In particular, the process of droplet steering and separation in microfluidic channels under the influence of electric fields requires accurate simulation of fluid dynamics, electric forces, and surface tension. FEM divides a complex domain into smaller elements, enabling the solution of physical equations at those elements. In EHD simulation, FEM allows analysis of the interaction between factors such as electric fields, fluid flow, and forces acting on the fluid in complex environments. Specifically in this topic, FEM is applied to solve Maxwell's equations (for electric fields) and Navier-Stokes equations (for fluid flow) simultaneously, thereby predicting the distribution of electric fields and fluid flow under the influence of electric fields. This method helps calculate the force exerted on the fluid, determine the direction and velocity of the flow, which is crucial in the design and optimization of devices that control fluid flow using electric fields, such as in electronic inkjet devices or biomedical applications. FEM is particularly effective in solving nonlinear problems and complex boundary conditions, making it well-suited for EHD systems.

In this study, to gain a deeper understanding of the hydrodynamic phenomena occurring in microdroplet separation technology within microchannels, along with ensuring the feasibility of the technique, a simulation model was proposed and developed. 3D channel model and structure 2.20 was set up on COMSOL Multiphysics software (6.1, COMSOL, Inc., Burlington, MA, USA) to match the actual structure of the microfluidic chip as in Figure 2.18. Two pairs of electrodes were designed with a flat copper structure and positioned outside the microchannel. The main channel has a width of 200 µm to allow the droplet to move freely without being affected by the microchannel edges. A spherical droplet object with a size of 15 µm was placed in the middle of the microchannel to simulate the actual position and size of the droplet in a real microfluidic chip. Finally, the channel height is set to 50 µm, consistent with the actual channel height of 50 to 60

µm. The physical dimensions of the microchannel are set and simulated multiple times to determine the optimal parameters for the droplet formation process, serving as the foundation for the fabrication of microchannels and electrodes in practice. The liquid used in the simulation for the flow and droplets is oil with water, and the physical parameters such as density, viscosity, and conductivity are set based on the optimal conditions of the liquid.

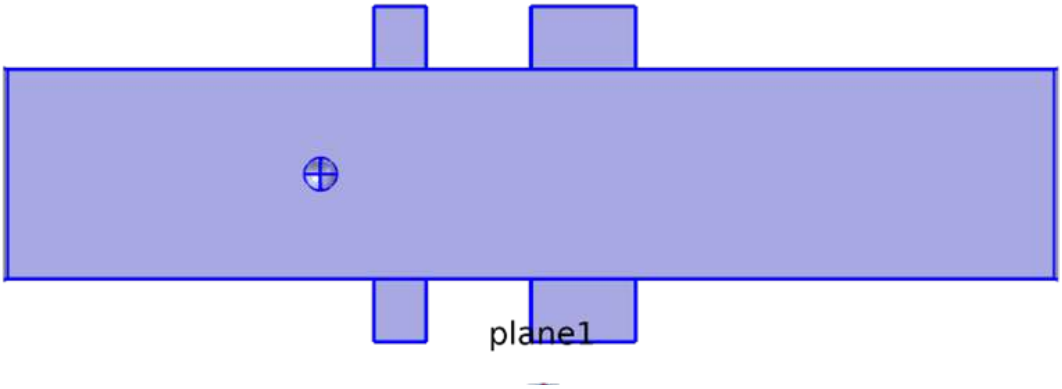

Figure 2.18: Structure of the 3D simulation model in the study

To ensure the accuracy of the model, the flow parameters of the oil environment were adjusted to match the actual conditions in the study. The interaction between the electric field and the liquid flow was simulated to study the effects of factors such as flow velocity, applied electric field, and electromagnetic force on droplet motion. The simulation results show that, by adjusting the voltage and flow parameters, the droplet separation and movement process in microchannels can be effectively controlled, opening up potential applications in automatic liquid classification systems and biological analysis devices.

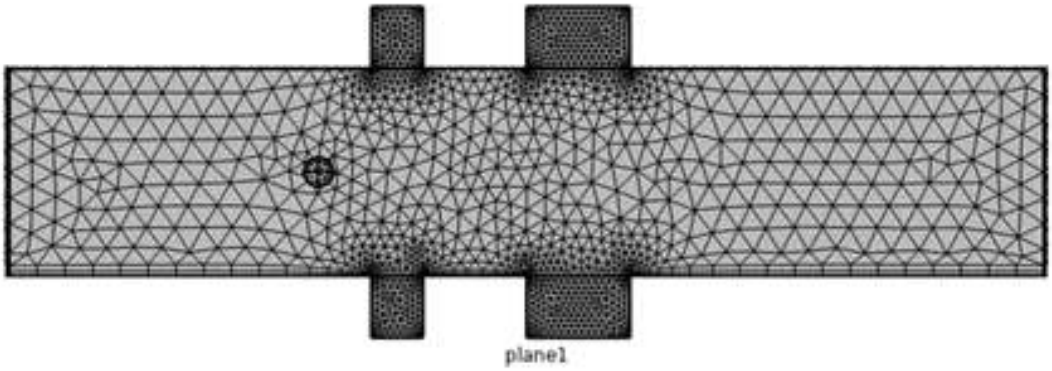

Figure 2.19: Finite elements in the simulation model

First, the simulation model mentioned in the previous section will be divided into finite elements in the form of a grid across the entire structure (Figure 2.19 illustrates the distribution of finite elements; the actual number of finite elements used is much larger

than in the figure). The smaller the size of the finite element, the higher the accuracy and detail of the simulation results; however, the computational model becomes more complex and requires stricter parameters. This size will be selected based on the requirements of the simulation problem. This study uses a large number of finite elements for the simulation model as follows: 7,127,983 domain elements, 258,400 boundary elements, and 4,299 corner elements to fully calculate the electric field and flow components and clearly show the changes of the droplet inside the channel. As can be seen in Figure 2.19, the density of finite elements is arranged more densely around the electrodes than in the regions inside the channel. This helps calculate the electric field parameters generated by the voltage applied to the four electrodes. After establishing the finite elements, the FEM method uses the input parameters to calculate the state values of each element in the structure. Each element in the structure is calculated at time steps based on parameters set at initialization or the results of the previous state. This process allows for accurate tracking and analysis of changes in the position, shape, and motion of the droplet throughout the simulation.

The spherical shape of the droplet is deformed by forces acting on the moving charges inside the droplet. This leads to electrohydrodynamic (EHD) effects, and as the applied voltage increases, the EHD effect becomes more pronounced, potentially causing the droplet to break up into smaller droplets. The droplet separation phenomenon observed in practice can be explained by the complex interaction between the electric field and the droplet, accurately modeled through the volume force module. This module incorporates the Maxwell stress tensor to calculate the electrostatic forces in three-dimensional space, which is crucial for understanding the behavior of the droplet under the influence of an electric field. The Maxwell stress tensor is represented as a matrix3×3 , reflecting the stress components exerted by the electric field on the droplet. The general form of the Maxwell stress tensorσ_M in three-dimensional space according to equation 2.28 is defined as follows.

$$\sigma_M = \varepsilon \begin{bmatrix} E_x^2 - \frac{1}{2}E^2 & E_x E_y & E_x E_z \\ E_y E_x & E_y^2 - \frac{1}{2}E^2 & E_y E_z \\ E_z E_x & E_z E_y & E_z^2 - \frac{1}{2}E^2 \end{bmatrix} \tag{2.43}$$

WhereE_x, E_y, E_z are the components of the electric field in the directions x, y and z, respectively. This tensor describes how the components of the electric field contribute to the internal stress within the droplet, leading to deformation and ultimately the separation of the droplet.

The force components in the directions x, y and z, denoted as F_x, F_y, F_z , are determined from the divergence of the Maxwell stress tensor, expressed by the following equations.

$$F_x = \frac{\partial \sigma_{xx}}{\partial x} + \frac{\partial \sigma_{xy}}{\partial y} + \frac{\partial \sigma_{xz}}{\partial z} \tag{2.44}$$

$$F_y = \frac{\partial \sigma_{yx}}{\partial x} + \frac{\partial \sigma_{yy}}{\partial y} + \frac{\partial \sigma_{yz}}{\partial z} \tag{2.45}$$

$$F_z = \frac{\partial \sigma_{zx}}{\partial x} + \frac{\partial \sigma_{zy}}{\partial y} + \frac{\partial \sigma_{zz}}{\partial z} \tag{2.46}$$

These equations describe how the divergence of the tensor components leads to forces acting on the droplet, causing deformation and controlling its motion.

The use of the COMSOL simulation model has helped clarify EHD phenomena in droplet separation technology and the theoretical basis behind the effect of electric fields on droplets. The simulation results include flow velocity, potential, electric field vector, and charge distribution on the droplet object. In this model, the input fluid flow rate is set to a fixed value of 2.78×10^{-11} m^3/s. From this parameter, I can calculate the velocity amplitude value inside the channel. As seen in Figure 2.20(A), the fluid flow velocity changes significantly in the region of the non-uniform electric field between the two large electrodes with opposite potentials. The cause of this phenomenon is that the electric field has affected the flow inside the microchannel. A study has shown that applying a potential to the flow can affect the flow velocity, as represented by the electric capillary coefficient ($\mathrm{Ca}_{(\mathrm{E})}$), which describes the ratio of the electric field pressure amplitude to the capillary pressure between two liquids[31] :

$$Ca_E = \frac{\varepsilon_m E^2 h}{\gamma} \tag{2.47}$$

where ϵ_m is the electrical conductivity of the environment outside the droplet, E is the electric field strength, h is the distance between the two electrodes, and γ is the surface tension between the two liquids. As Ca_Eincreases, the flow velocity gradually increases. This coefficient helps to assess the effect of the electric field on the droplet and the flow within the simulated and actual microchannel. In addition to affecting velocity, this coefficient also helps determine whether the droplet deformation regime is stable or unstable. In the dense electric field region, the flow velocity is greatly affected by the strong polarization effect in the channel and the Maxwell electric field pressure gradient, causing the velocity amplitude to increase from 45×10^{-4} m/s to 55×10^{-4} m/s. This velocity change region causes the droplet to change its initial direction or split into smaller droplets, depending on the magnitude of the electric field used inside the channel. The simulation results partially explain the phenomenon of droplet deflection or splitting in the design of the separation system in this study.

Another important set of simulation results is the potential shown in Figure 2.20(B). It can be seen that under the influence of three high-potential electrodes at 1300V, the

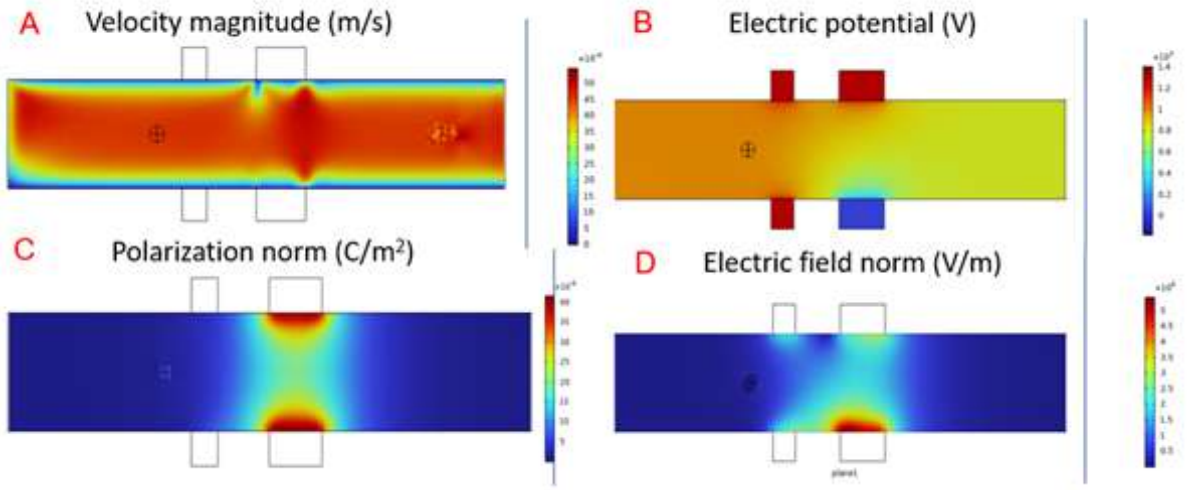

Figure 2.20: Results from the droplet separation system simulation model. A) Velocity amplitude. B) Potential. C) Polarization. D) Electric field strength

potential inside the microchannel ranges from 800 to 1000V depending on the distance of the points from the three electrodes. The three high-voltage electrodes create an electric field in the oil liquid with a value of approximately 1000V. The phenomenon of electric field generation is based on Gauss's law of electric field distribution:

$$Q = \nabla \cdot (\varepsilon \mathbf{E}) \tag{2.48}$$

Where Q is the charge density per unit volume, ϵ is the permittivity of the liquid, and $\overrightarrow{E}$ is the electric field vector. This law facilitates the calculation and analysis of electric fields in highly symmetric systems, while confirming that the electric field depends only on the charges within a given spatial region. Parallel to Gauss's law, charge is also conserved by the governing equation:

$$\frac{\partial Q}{\partial t} + \nabla \cdot I_p = 0 \tag{2.49}$$

where I_p is the current density. This principle ensures that the total charge in the system is always conserved, helping me understand the operating principle of an uneven electric field environment. Charges from three electrodes with high potential create an uneven electric field in the oil liquid environment in the channel. This static electric field causes the oil molecules in the channel to become polarized, creating a polarized region with opposite charges at different poles of the oil molecules. This creates an uneven electric field, which acts on the passing water droplet. Polarization occurs on the surface of the water droplet, forming two poles with negative and positive charges. As the water droplet passes through the non-uniform electric field, this polarization leads to the formation of dielectrophoretic forces (DEP) within the droplet, altering its structure and movement within the channel. This phenomenon is the operating mechanism in

microdroplet separation systems, where dielectrophoretic forces act on water droplets, causing droplet separation or controlling their movement.

Figure 2.20(C) shows the simulation results of the polarization of the environment inside the channel under the influence of an electric field. At the two large electrodes with opposite potential values, the polarization is greatest throughout the channel due to the concentration of oppositely charged particles moving between the two electrodes. The polarization is calculated using the formula:

$$P = \varepsilon_0(\varepsilon_o - 1)E \tag{2.50}$$

With P being the polarization vector, ϵ_0 is the permittivity of free space (8.85×10^{-12} F/m), and ϵ_o is the permittivity of the oil medium. The polarization of the oil in the channel has a small value, approximately half that in the region surrounding the electrodes, which is 20×10^{-6} C/m^2, due to its location in the strong electric field region within the channel. For points at the small electrodes, the polarization is smaller and not strong enough to affect the structure and shape form of the droplet. This region of weak polarization causes the droplet to become polarized as mentioned above, improving the effect of electric forces on the droplet and causing it to deform.

Finally, Figure 2.20(D) shows the simulation results of the electric field intensity in the channel, where the electric field region extends from the high-potential electrodes to the electrode set to zero potential. It is clearly visible that this is an area of non-uniform electric field, with the electric field intensity values at the center of the channel and between the two electrodes ranging from 2 to 2.5×10^6 V/m. This is the region where the droplet is most affected by the electric field due to the high electric field density, and the flow velocity also increases significantly here. Based on Gauss's law (Equation 16), I can analyze the effect of the electric field in the dielectric medium, which is oil. The oil material in this simulation model has a low permittivity of 2.2 F/m, so a high voltage is required to generate an electric field region with sufficient intensity to separate the droplets. The selection of oil and water materials is not only based on the different viscosities of the solutions; for the electric field to act on the water droplets in the microchannel, the permittivity of the two materials must also be considered. The permittivity of water in the simulation is 80 F/m, making the water droplet surface easier to polarize and more strongly influenced by the DEP force. The magnitude of the DEP force acting on the droplet depends on the permittivity difference between the two materials:

$$F_{DEP} = 2\pi a^3 \varepsilon_o \mathrm{Re}\left(\frac{\varepsilon_w^* - \varepsilon_o^*}{\varepsilon_w^* + 2\varepsilon_o^*}\right)\nabla E^2 \tag{2.51}$$

Where a is the radius of the droplet, ϵ_o is the permittivity of the oil environment surrounding the droplet, andε_w^*, ε_o^* is the complex permittivity of the two materials,

water and oil[32] . The complex permittivity is calculated using the following formula:

$$\varepsilon^*_{w,o} = \varepsilon_0 \varepsilon_{w,o} - j\frac{\sigma_{w,o}}{2\pi f} \tag{2.52}$$

Where f is the frequency of the electric field. However, the power source used in this study is a direct current source, so the frequency f is zero. Therefore, only the component$\varepsilon_0 \varepsilon_{w,o}$ plays a decisive role in the complex permittivity of the two materials. Thus, the selection of water and oil as the two materials in this study is appropriate for creating an electric field inside the channel. With the difference in permittivity, the DEP force generated by the non-uniform electric field will have a stronger effect on the water droplet. Finally, the distribution of the electric field shows that near the ground electrode, the electric field intensity reaches 5×10^6V/m. This phenomenon occurs because the electric field gradients are concentrated at the electrode with a low potential, so the electric field intensity here has a greater value than in the middle of the channel. In this region, positive charges are strongly attracted to the ground electrode by the DEP force and the electrostatic force, causing the droplet to deform.

2.3 Conclusion

In this chapter, a comprehensive theoretical framework was established to support the design of the integrated Lab-on-a-Chip platform for rare lung cancer cell analysis. First, the molecular recognition mechanism between EpCAM-specific aptamers and A549 cells, together with the subsequent coupling to Fe_3O_4 magnetic beads, was analyzed to clarify how stable, selective aptamer-magnetic labeling underpins efficient CTC capture in the cavity-integrated microchannel. Next, the principles of inertial microfluidics in spiral channels were developed, highlighting the balance between inertial lift and Dean drag forces that enables single-file focusing and uniform longitudinal spacing of cells prior to downstream detection. Finally, the electrohydrodynamic basis of dielectrophoresis for droplet steering and splitting was formulated, including the coupling of Navier–Stokes and Maxwell equations and the role of non-uniform electric fields in controlling water-in-oil droplet trajectories.

Numerical simulations using finite element models confirmed that the proposed design parameters are physically sound and suitable for implementation. The cavity-integrated magnetic separator achieved a simulated capture efficiency in the range of 80–100%, while the continuous spiral structure produced stable single-stream focusing of cells over practical Reynolds numbers. In the DEP-based droplet module, the simulations demonstrated precise steering and controllable splitting of droplets by tuning the applied voltage and electrode geometry, thereby optimizing droplet partitioning at the outlet junction. Collectively, these results validate the selected geometries, operating conditions, and material

choices, providing a solid theoretical and computational foundation for the experimental fabrication and characterization work presented in the subsequent chapter.

Chapter 3

MATERIAL PREPARATION AND EXPERIMENT SETUP

3.1 Fabrication Process and Sample Preparation

3.1.1 Microelectrode Fabrication Process

Fabrication of microelectrode structures using the wet etching method:

The photolithography method uses a mask and UV light source to create structures on a photoresist polymer layer, according to the mask design. The resolution of the mask depends on specific requirements: it can be laser printing on a transparent substrate (1200 dpi with a resolution of about 250 nm), high resolution on thin transparent film (10,000 dpi, about 30 nm), or a high-end mask with a structure printed by depositing Chromium on quartz (420,000 dpi, about 600 nm). High-resolution masks are typically more expensive and limited in size to microfluidic devices, usually around 100 mm per side. In this study, the mask was fabricated as a 4 inch quartz wafer as described in Figure 3.1.

The fabrication process for microelectrode structures based on photolithography and wet etching includes the following steps (Figure 3.2):

- **Step 1:** The S1813 photoresist layer (Shipley 1813, MicroChem Co., Ltd., Westborough, MA, USA) is coated onto a glass substrate that has been sputter-coated with a layer of chromium and gold and surface-treated. The coating process is performed in two stages: first, spinning at 700 rpm for 10 s, then increasing to 1700 rpm for 20 s to create a 2 µm thick photoresist layer. Next, the substrate is heated at 90 °C for 2 min to fix the coating.

- **Step 2:** The freshly coated photoresist layer is exposed to UV light at an energy level of 90 mJ cm^{-2}. After exposure, the glass plate is heated at 90 °C for 3 min to fix the photoresist layer.

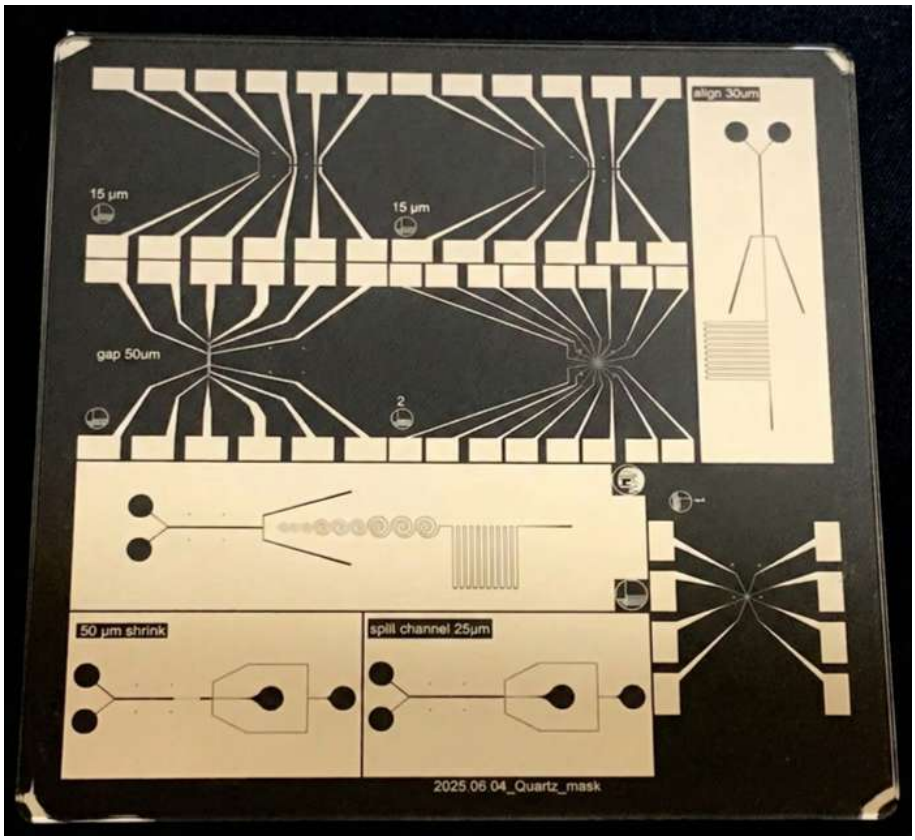

Figure 3.1: Quartz masks are used to fabricate electrodes

- **Step 3:** Prepare the developer solution by diluting MP 351 with DI water at a ratio of 2:9. The photoresist activated by UV light in the exposure step is developed by immersing the wafer in the developer solution for about 9 s. Then, rinse the wafer again with DI water and dry it with N_2 gas. The wafer is baked at 120 °C for 3 min to completely remove any remaining moisture on the surface.

- **Step 4:** Etch the gold layer not protected by photoresist by immersing the wafer in a gold etchant solution for about 15 s. Then, rinse the wafer again with DI water and dry it with N_2 gas.

- **Step 5:** Etch the Chromium layer not protected by photoresist by immersing the wafer in Chromium etchant solution for about 10 s. Next, rinse the wafer with DI water and dry it with N_2 gas.

- **Step 6:** Remove the remaining photoresist layer by rinsing the wafer with Acetone and Ethanol solution. Then, rinse the wafer again with DI water and dry it with N_2 gas.

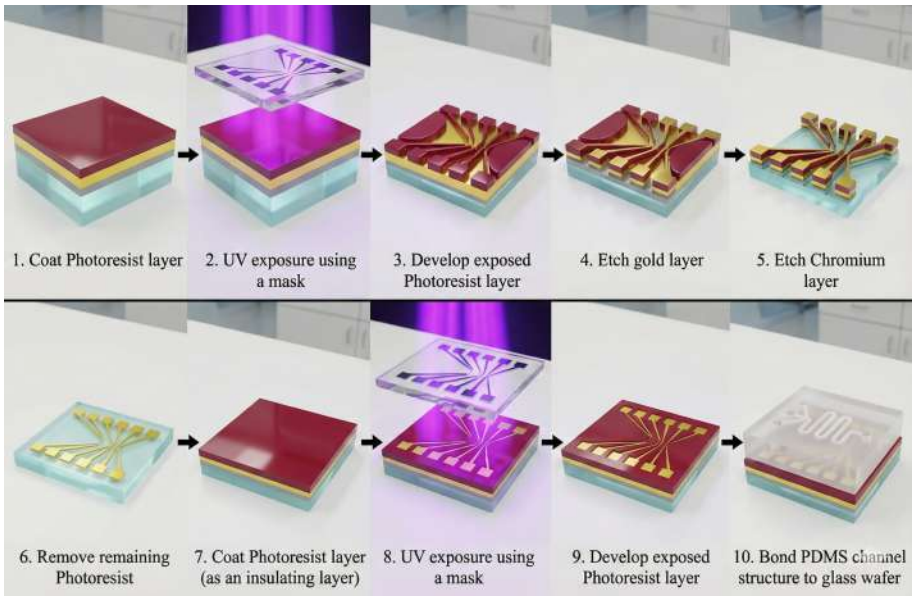

Figure 3.2: Fabrication process for microelectrode structures with microchannel structures

3.1.2 Microfluidic channel fabrication process

The polydimethylsiloxane (PDMS) microchannel was fabricated using soft lithography, a standard method in microfluidic technology (Figure 3.3) [82]. This process consists of two main stages: fabrication of the master mold using SU-8 photoresist material and replication of the microchannel structure onto PDMS material from that master mold. The technological parameters were optimized to ensure geometric accuracy and quality of the microchannel structures.

- **Step 1:** First, the master mold is fabricated on a silicon substrate. The silicon wafer is prepared and thoroughly cleaned by soaking in methanol, acetone, and then rinsing with deionized (DI) water before being dried with nitrogen gas. To create the microchannel structure, a layer of SU-8 2050 photoresist is evenly coated onto the silicon substrate surface. The channel height is controlled by the speed and duration of the spin-coating process. For example, to achieve a channel height of 100 µm for , the spin speed was set at 1700 rpm for 30 s. After coating, the substrate was soft baked at 65 °C and 95 °C to evaporate the solvent and stabilize the photoresist layer.

- **Step 2:** Spin coat with a spin coater (Laurell Technologies, Model: WS-650MZ-23NPP) for 35 s at 1000 rpm or 4000 rpm to create SU-8 layers with thicknesses of 100 µm and 30 µm, respectively.

- **Step 3:** Prebake (Softbake): Heat the SU-8-coated silicon wafer (2050, MicroChem Corp., Newton, MA, USA) from room temperature to 95 °C. Increase the temperature by 5 degrees every 2 min. The temperature increase from 60 °C to 65 °C was

maintained for 10 min, and the temperature increase from 90 °C to 95 °C was maintained for 30 min. The silicon wafer was then cooled to room temperature for at least 2 hours.

- **Step 4:** Expose the cooled silicon wafer to UV light (MIDAS SYSTEM, Model: MDA-400S Mask Aligner). The silicon wafer is set up with a mask containing defined structures placed on top of the wafer. The exposure energy is set according to the photoresist supplier's requirements; in this case, the energy is set at 210 mJ cm^{-2}.
- **Step 5:** Post exposure bake: Heat the exposed wafer from room temperature to 95 °C. Increase the temperature by 5 degrees every 2 min. The temperature increase from 60 °C to 65 °C is maintained for 5 min, and the temperature increase from 90 °C to 95 °C is maintained for 8 min. After that, the silicon wafer is cooled back to room temperature for at least 2 hours.
- **Step 6:** Develop the SU-8 photoresist using SU-8 Developer solution to remove unwanted photoresist. The remaining SU-8 photoresist will be used as a mold for the liquid microchannel.

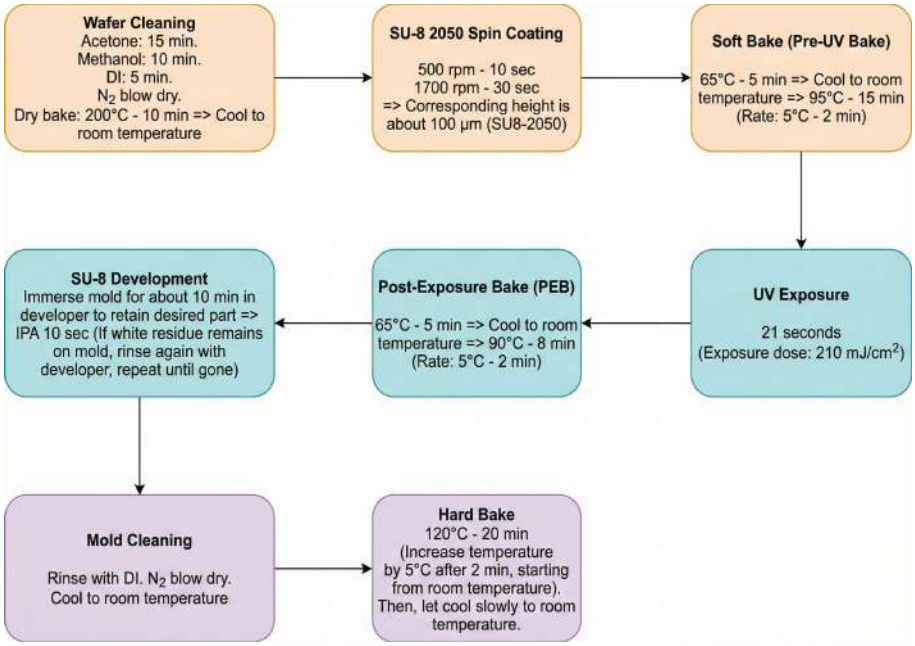

Figure 3.3: Optimized process for fabricating SU-8 channel molds

The next step is to replicate the structure from the master mold onto PDMS. The PDMS mixture is prepared by mixing the base polymer and curing agent (Dow Corning, Model: Sylgard 184) at a 10:1 weight ratio. The mixture is then degassed in a vacuum chamber to completely remove air bubbles. The liquid PDMS solution is poured onto the SU-8 mold surface and cured at 65 °C for 2 hours. After curing is complete, the PDMS

layer is carefully peeled off the master mold, forming an exact replica of the microchannel structure. Inlet and outlet ports are created using a specialized punching tool.

To complete the microfluidic chip, the surface of the PDMS sheet containing the microchannels and the surface of a substrate (e.g., a glass sheet containing microelectrodes) are treated with oxygen plasma. This process activates the surfaces, making them hydrophilic and facilitating permanent, irreversible bonding when the two surfaces are pressed together. The alignment process between the microchannels and the structures on the substrate is performed with high precision under the support of a camera monitoring system, ensuring absolute alignment before bonding, completing the microfluidic device.

Table 3.1: Optimal parameter table for the manufacturing process for 30 µm and 100 µm chips

Process parameters	**LoC (30 µm height)**	**LoC (100 µm height)**
Coating rotation speed (rpm)	4000	1700
Coating rotation time (s)	35	30
Soft bake 65 °C (minutes)	3	5
Soft bake 95 °C (minutes)	6	10
UV energy level ($mJ\,cm^{-2}$)	200	260–280
Irradiation time (s)	20	26–28
Post-Exposure Bake 65 °C (minutes)	1	5
Post-Exposure Bake 95 °C (minutes)	6	12
Development time (s)	10–15	15–20
Hard bake at 150 °C (minutes)	5	10

In the microfluidic device fabrication process, the selection and optimization of technological parameters such as spin coating speed, baking time, exposure time, and UV energy level are key factors that directly affect the quality and geometry of the microfluidic channel. Based on the design goal of channels with two heights of 50 µm and 100 µm, the parameters were fine-tuned to ensure accuracy in photoresist (SU-8) layer thickness, mold adhesion, and sharp patterning (Table 3.1). Specifically, at a height of approximately 30 µm, the SU-8 layer requires a higher spin coating speed (4000 rpm) to create a uniform thin film. The baking steps (soft bake and post-exposure bake) were also optimized with shorter times because the thin layer easily loses moisture and stabilizes its shape quickly. An UV irradiation energy level of $200\,mJ\,cm^{-2}$ and an exposure time of 20 s were sufficient to penetrate the thin SU-8 layer and ensure complete polymerization.

Conversely, at a height of 100 µm, the thicker SU-8 layer requires a lower spin speed (1700 rpm) to maintain the desired thickness. Both baking and exposure steps have higher time and energy (UV $260\,mJ\,cm^{-2}$ to $280\,mJ\,cm^{-2}$, 26 s to 28 s) to ensure deep UV penetration and polymerization reaction throughout the entire SU-8 layer height. Simultaneously, the exposure time is extended to completely remove the unexposed portion

without damaging the structure.

The selection of two channel heights, 30 µm and 100 µm, is based on specific application requirements:

- 30 µm is typically suitable for laminar flow, precise microfluidic control, and single-cell separation.
- 100 µm allows for higher flow rates, reduced inlet pressure, and is suitable for micro-particle systems or 3D cell models.

In this study, after optimization, a channel height of approximately 30 µm was selected as optimal. This channel height avoids channel blockage during magnetic separation and provides sufficient sensitivity for cell detection and quantification based on impedance signals.

3.1.3 Sample Preparation Process for Magnetic Separation Systems

First, prepare A549 (Sigma-Aldrich, Model: 8601284-CDNA-20UL) and HeLa (Sigma-Aldrich, Model: CB_85120602) cell samples cultured stably in a suitable medium and conditions. The steps for preparing the solution are described in detail below:

1. Use a pipette to take 5 µL of magnetic bead solution into a centrifuge tube and place it on a magnetic stand. The magnetic bead solution will be washed with 100 µL of MES buffer solution using a pipette. After washing the magnetic bead solution, the research team will use a magnetic stand to fix the magnetic beads and remove the excess liquid.
2. Add 60 µL of MES buffer solution and 40 µL of NHS/EDC solution to the washed magnetic particles. Mix the mixture thoroughly with a pipette and incubate the solution on a mixer with an oscillating shaking mode at 30 rpm for 30 min.
3. Prepare the NH_2-modified aptamer solution (solution stored in a freezer):

- After removing the centrifuge tube containing 5 µL of aptamer from the freezer, centrifuge at 10 000 rpm for 1 minute.
- Warm the aptamer using boiling water.
- Remove the aptamer from the hot water and allow it to cool for 15 min.
- Add 45 µL of binding buffer solution to the centrifuge tube and mix with a pipette.

4. Use a magnetic stand to fix the magnetic beads and remove excess liquid. Add the aptamer solution to the centrifuge tube containing the magnetic beads and mix the solution thoroughly with a pipette. Incubate the solution on a mixer set to oscillate at 30 rpm for 90 min.

5. Prepare A549 and HeLa cells

- Remove the cell culture dish from the incubator and aspirate the old DMEM solution from the dish using a pump.
- Wash the cells in the dish twice with 1.5 mL of 1X PBS solution (the solution will then be aspirated from the dish).
- Add 1.5 mL of Trypsin solution to the cell dish and place it in an incubator at 38 °C and 5% CO_2 for 5 min. This step will cause the cells adhering to the dish to detach from the bottom of the dish.
- After removing the cell dish from the incubator, add 1.5 mL of DMEM solution to the dish to neutralize the cell-killing effect of Trypsin.
- Tap the sides of the culture dish to ensure the cells are completely detached from the dish.
- Use a plastic pipette to aspirate the solution containing A549 cells into a centrifuge tube.
- The centrifuge tube will contain approximately 10^6 A549 cells in 1.5 mL of solution.
- Repeat the above steps with the HeLa cell culture dish.

6. Cell staining

- Place the centrifuge tube containing 1.5 mL of solution with A549 cells and the centrifuge tube containing 1.5 mL of solution with HeLa cells into a centrifuge at 500 rpm for 5 min.
- Remove the excess solution from the two centrifuge tubes and replace it with 1X PBS solution twice to wash the cells.
- Add 3 µL of blue staining solution to the solution containing A549 cells; add 3 µL of red staining solution to the solution containing HeLa cells and incubate in a Mixer at 25 rpm for 15 min.
- After staining, count the cells using a counting chamber to determine the cell concentration to be used in the experiment.

7. After incubating the magnetic bead solution for 90 min, wash the magnetic bead solution on the magnetic stand with 100 µL of 1X PBS solution three times. Add 200 µL of HeLa cell solution to the centrifuge tube containing the washed magnetic beads. Mix the solution thoroughly and place the system in a mixer with an oscillating shaking mode at 30 rpm for 30 min.

8. Complete the magnetic bead binding process

5 µL of the solution will be used for microscopic observation to evaluate staining and magnetic bead binding efficiency (Figure 3.4). The prepared solution sample will be transferred into a syringe for microfluidic separation experiments.

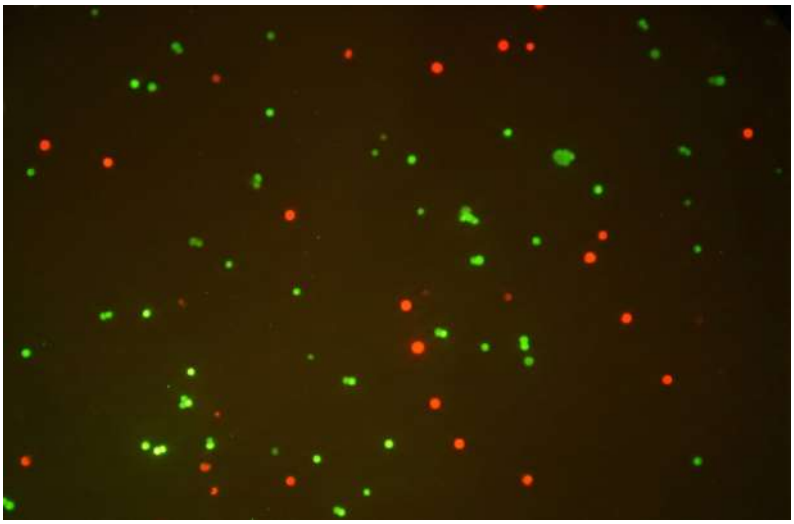

Figure 3.4: Images of A549 cells (stained blue) and Hela cells (stained red)

3.2 Experiment Setup

3.2.1 Experimental configuration for magnetic separation

The magnetic separation experiment system was arranged as shown in Figure 3.5, including the main components: micro syringe, microfluidic chip mounted on a microscope stage, fluorescent light source, CCD camera, and computer connected to image acquisition software. The A549 cell line labeled with magnetic particles was delivered from the container tube through the microinjection pump into the microfluidic channel at a flow rate adjusted between 2–8 µL/min to maintain stable laminar flow throughout the channel. The microfluidic chip was precisely positioned under the objective lens of the microscope to ensure the observation field always aligned with the magnetic compartments.

To create a magnetic field during the experiment, a permanent magnet was placed outside the chip at a position corresponding to the chamber area of the microfluidic channel. The intensity and direction of the magnetic field are adjusted so that the magnetic

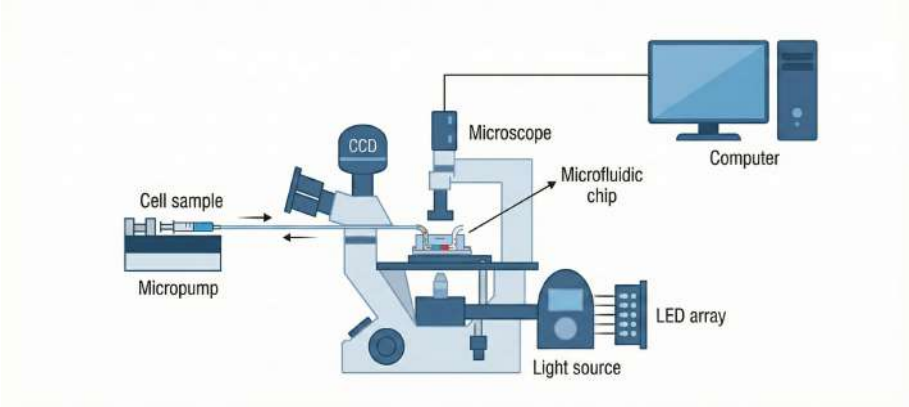

Figure 3.5: Experimental setup for magnetic separation

gradient is concentrated at the upper wall of the channel – where the phenomenon of magnetic particle-bound cell capture is expected to occur. Light from an LED fluorescent source is shone through the transparent glass substrate of the chip, allowing clear observation of the location of stained cells.

Before conducting the experiment, A549 cells were labeled with magnetic nanoparticles and stained with a specific fluorescent dye for easy identification under a microscope. During operation, the fluorescent images emitted by the captured cells were captured by a high-sensitivity CCD camera, transmitted directly to a computer for recording and processing. This allowed real-time observation of the movement, positioning, and adhesion of magnetic cells in the channel.

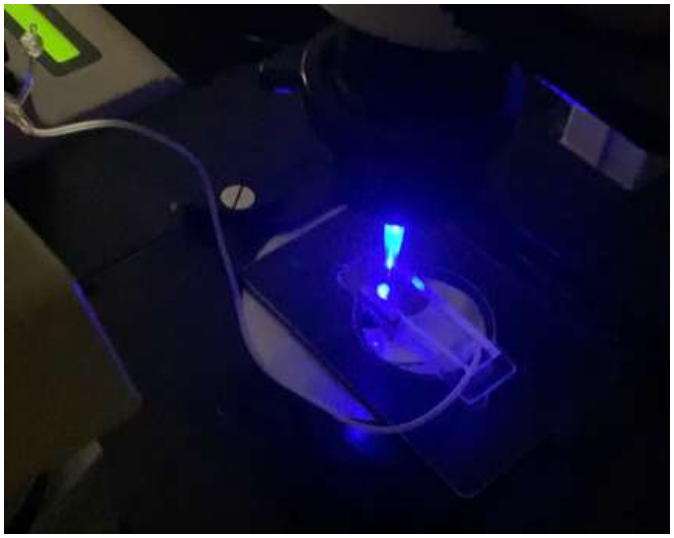

Figure 3.6: Actual setup of magnetic separation on a microfluidic chip

Figure 3.6 shows the actual configuration of the experiment. The microfluidic chip is fixed on the microscope stage, with the inlet connected to a micro-syringe. Blue fluorescent light is used to detect the signal from stained cells, enabling direct observation of the capture process of A549 cells labeled with magnetic particles. Experimental conditions are

maintained at room temperature, with the pumping rate adjusted appropriately to avoid flow disruption or excessive shear forces that could affect the adhesion of magnetically captured cells.

This setup allows for visual verification of the magnetic cell capture process in a microfluidic environment, serving as an important intermediate step before performing quantitative separation efficiency experiments. Simultaneously, this configuration is also used to calibrate operational parameters such as optimal pumping speed, magnet placement, and light intensity, ensuring standardized conditions for accurate fluorescence data acquisition in subsequent experiments.

3.2.2 Experimental configuration for impedance measurement

The cell counting system is operated according to a complete device procedure, in which each step supports and complements each other to ensure high accuracy and reliability of the count. First, the cell sample is prepared under standard conditions, including appropriate dilution, removal of debris or fragments, and ensuring cell integrity before entering the system. After preparation, the sample is loaded into a microfluidic pump, where the sample flow is pushed into microchannels at a stable speed to avoid air bubbles or flow fluctuations, factors that could affect the measurement results.

As the sample moves through the microfluidic chip, integrated impedance sensors on the planar structure continuously record electrical signal changes as each cell passes through the measurement region. These impedance measurements enable the detection and characterization of cells based on electrical variations in the surrounding environment. Simultaneously, the entire process is monitored under an optical microscope, combined with a high-speed camera to capture images and videos of cells moving in the microchannel. Thus, image data can be used for verification, morphological description, or to supplement the signal analysis step.

Subsequently, the acquired electrical signals and images are transferred to a data acquisition and processing unit, where the system performs noise filtering, event separation, and signal classification related to each cell. Processing algorithms are then applied to extract information, calculate cell counts, and determine parameters related to their electrical characteristics. This analysis step helps link pure data from the sensor with visual observations from the optical system, producing reliable and well-founded results.

Finally, all results are displayed through the system's intuitive interface, allowing users to easily evaluate cell counts, compare sensor data with images, and use the information obtained for further research or applications. Through the integration of microfluidic, electronic, and optical devices, this process forms an efficient, automated cell counting system suitable for microscopic analysis in biological and biomedical research.

Table 3.2 presents the main specifications and corresponding functions of the compo-

Table 3.2: Data table on equipment in the cell counting system

No.	Equipment	Key technical specifications	Notes
1	Liquid pump	Adjustable flow rate: 0.1–10 μL/min	Used to push cell samples into stable microchannels
2	Microfluidic channel	Width: 30 µm, height: 30 µm	Integrated with sensors and designed to fit cell size
3	High-speed camera	Frame rate: 1000 fps, resolution: 640×480 px	Records the process of cell movement in the channel for comparison
4	Impedance measurement circuit	Frequency range: 10 kHz – 300 kHz, sensitivity: <10 mV/cell	Capture electrical signals and determine cell presence
5	Signal and image processing software	Supports impedance signal analysis and cell image recognition	Simultaneous data processing from measurement circuit and camera
6	Control computer and data storage	CPU $\geq$ i5, RAM $\geq$ 8GB, storage $\geq$ 256GB SSD	System control, data storage, and result display

nent devices in the Lab-on-a-Chip integrated cell counting system. The system uses a liquid pump with adjustable flow rates from 0.1 to 10 μL/min to ensure stable flow in the microchannel. The microfluidic channel is designed with compact dimensions (30 µm wide, 30 µm high) to match cell size and optimize sensor performance. The high-speed camera has a frame rate of up to 1000 frames per second with a resolution of 640×480 pixels, enabling accurate recording of cell movement within the channel. The impedance measurement circuit operates in the frequency range from 10 kHz to 300 kHz, with a sensitivity below 10 mV/cell, serving to receive bioelectric signals to determine the presence of cells. Data from the camera and measurement circuit are processed simultaneously through dedicated software, enabling impedance signal analysis, image recognition, and automatic cell counting. Finally, the entire system is controlled and data is stored by a computer with a minimum configuration of an i5 CPU, 8GB RAM, and an SSD hard drive, ensuring stable operation and fast data processing. The specification table provides an overview of the technical features and roles of each device, serving as a basis for system evaluation and optimization.

Figure 3.7 shows the actual connection of the system, including key components such as a microscope, impedance measurement circuit, analysis computer, and camera. Based on this image, we will describe and analyze how each component in the cell counting system works.

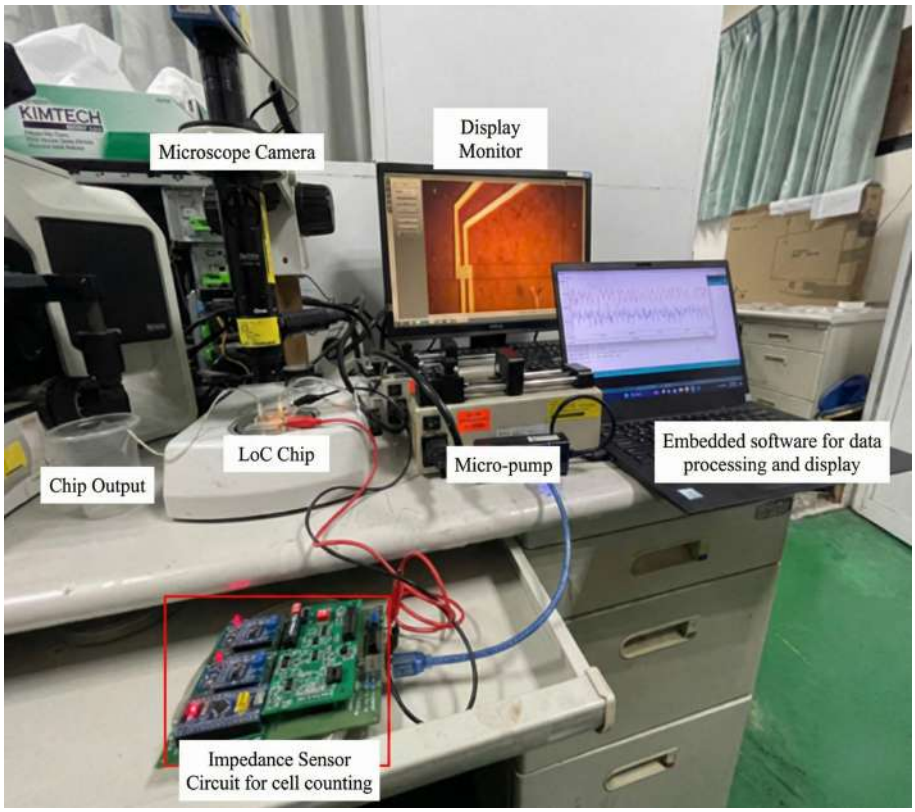

Figure 3.7: Image of the cell counting system setup

3.2.3 Experimental configuration for cell encapsulation in droplets and droplet separation using DEP

Based on the issues raised and the research objectives, the microfluidic cell packaging system for single-cell analysis was developed as follows.

Figure 3.8 shows the experimental setup with a microfluidic chip. The microfluidic chip has two input channels and one discharge channel. The input channels include an oil solution channel and a water solution channel. The test object is a plastic particle sample mixed with water solution at a ratio of 1 gram of particles mixed with 5 mL of water. In addition, the micropump uses two 5 mL cylinders containing the input solution for the chip. To test the system, the pump speed in the water channel is kept constant at 3 µL/min, and the pump speed in the oil channel is gradually increased from 5 µL/min to 8 µL/min.

The hardware system consists of four main components: a microfluidic chip, a micropump, a high-speed camera, and a processor. The output of the hardware system is cells encapsulated in droplets. Images of the droplets are sent from the camera to the processor and analyzed by deep learning algorithms to detect droplets and count the number of cells.

The pumping process is performed after successfully connecting the pumping channels to the droplet-forming chip. For a microfluidic system to operate smoothly, the dispersed

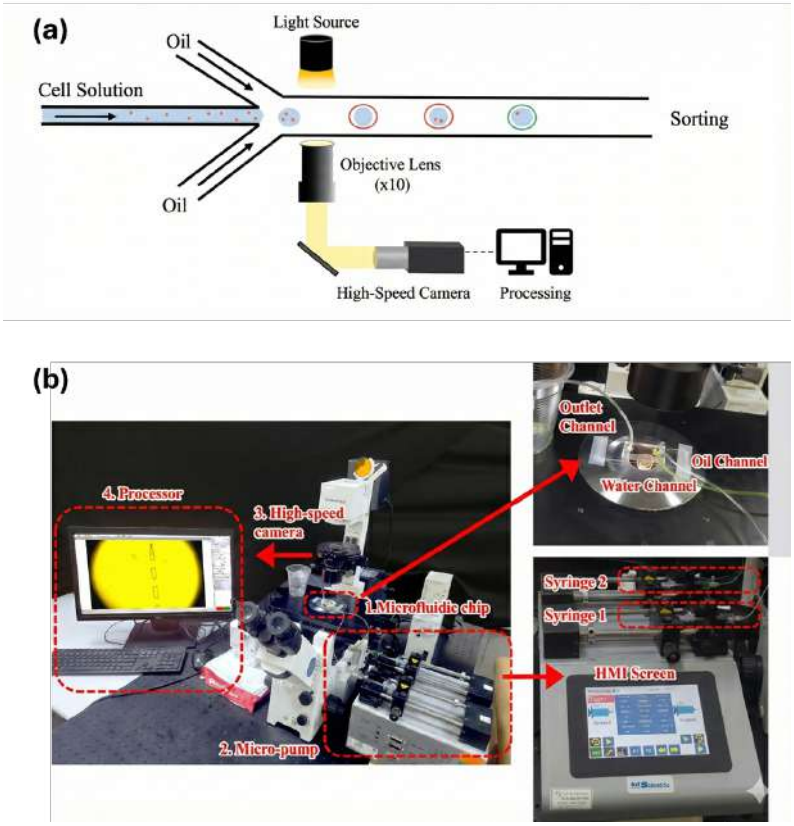

Figure 3.8: Overall system for cell encapsulation in droplets and droplet sorting using DEP

phase and continuous phase of the device must be pumped evenly. Microfluidic chips have very small phases, so micro-pumps are needed to use driving force to push the solution into the phases. Micro-pumps need to be stable and capable of transferring liquid at slow speed and can be changed over time to achieve the desired droplet size. During droplet formation, energy introduced from the cylinder pumps or pressure controllers is partially converted into interfacial energy, thereby promoting instability of the liquid-liquid interface and causing droplets to be cut off from the dispersed phase.

The microfluidic cell separation system developed consists of three main modules: the observation and display module, the flow manipulation module, and the microdroplet manipulation module. The observation and display module uses a display screen and microscope to observe liquid droplets and analyze the cell separation process in the microchannel. The flow control module includes cylinders that control the flow of liquids (water and oil) and connection systems such as solution delivery tubes, allowing precise adjustment of the flow through the microchannel. The microdroplet manipulation block includes devices that enable the control and separation of liquid droplets in the channel, including a high voltage source to generate an electric field that affects the droplets. This system allows experiments to be performed in a compact space and can be packaged into a dedicated experiment kit if the observation and flow manipulation blocks are replaced

with smaller devices.

The micro-pump used in the system is the "GEMINI 88 Plus Dual Syringe Pump" from KD Scientific. The micro-pump provides two independent pumping channels, P1 and P2, which are linked via both software and hardware. The micro-pump meets the main requirements of the project, such as remote control via USB cable, interaction via HMI interface, and the ability to control the difference in speed between the two pumping channels to influence the droplet control process. To support the data collection process for droplet formation, the system uses a high-speed Phantom camera with the model number "VEO-710L-72G-C" to observe the microfluidic channel. This is a high-speed camera capable of 7400 fps with an image resolution of 1280×800, suitable for providing detailed videos of the research subjects. The processing unit includes a computer device responsible for receiving image and video signals from the camera and performing analysis algorithms. With different channel velocities, the size of droplets displayed on the computer screen varies, and the number of cells packaged relates to size and flow rate, all recognized by deep learning algorithms.

3.3 Signal processing techniques

3.3.1 Computer vision model for quantifying the coverage value of magnetic particles

Quantifying the coverage value of magnetic particles

The effectiveness of cell separation systems using magnetic fields strongly depends on the specific binding ability between target cells and magnetic beads (MBs). Therefore, quantitatively assessing the degree of cell surface coverage by MBs is crucial for ensuring the quality of the cell-bead binding process, which directly impacts the capability and efficiency of magnetic separation devices. Additionally, analyzing the impact of magnetic particle size on cell surface coverage provides important data for selecting the optimal particle size in practice.

Figure 3.9 illustrates the principle of quantitatively calculating the degree of MB coverage on the surface of A549 lung cancer cells. The coverage value is determined by the ratio of the cell surface area covered by MBs (MBs Area) to the total cell surface area (Cell Area). Specifically, the cell area covered by MBs is determined from bright-field images and fluorescence images; fluorescence images are particularly useful when the cell area is heavily obscured by MBs in bright-field images. The coverage value is calculated using the formula:

$$\text{Coverage value} = \frac{\text{MBs Area}}{\text{Cell Area}} \tag{3.1}$$

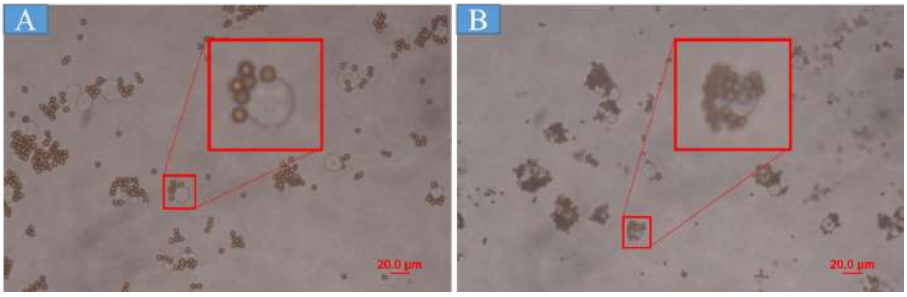

Figure 3.9: Quantitative assessment of magnetic particle coverage on A549 target cells

where the MBs area is determined directly through bright-field image analysis or combined with fluorescence images, while the total cell area is mainly extracted from fluorescence images to avoid errors caused by cells being covered by magnetic particles in bright-field images. Quantitative assessment of the coverage level of MBs on the cell surface is very important for magnetic separation efficiency. Specifically, a high coverage level means that the number of MBs bound to the cells increases, leading to a significant increase in the magnetic force acting on the cells. Conversely, when the cell surface area is less covered, the magnetic force obtained may be insufficient to manipulate or effectively separate target cells, especially under conditions of high flow velocity or low magnetic field gradient. Furthermore, determining the coverage value also provides direct information about the effectiveness of MB surface functionalization and the specific recognition ability of the aptamer or antibody used. Thus, the coverage value serves as a quantitative parameter for evaluating the performance of sample preparation and processing steps prior to magnetic separation, enabling optimization of experimental parameters to achieve the best results.

Application of Computer vision models for evaluation In recent years, image segmentation techniques have been extensively researched and developed, particularly in biomedical applications such as tumor detection in medical images, cell classification in microscopic images, tissue segmentation in MRI images, and anatomical structure analysis from CT images. Among these, cell segmentation plays an essential role in cell analysis, helping to accurately identify and quantify rare cells in complex biological samples, thereby supporting early disease detection and effective treatment monitoring.

In this study, a key challenge addressed was how to accurately quantify the surface area of cells covered by magnetic particles and predict the actual cell area through image processing and segmentation techniques. These techniques allow determining the number of pixels corresponding to the covered area on the acquired image (Figure 3.10). In this study, we used a 20° magnification objective lens, which is the optimal balance between resolution and image acquisition efficiency , ensuring the necessary analysis quality while minimizing experimental time and minimizing cell damage when outside the culture

environment.

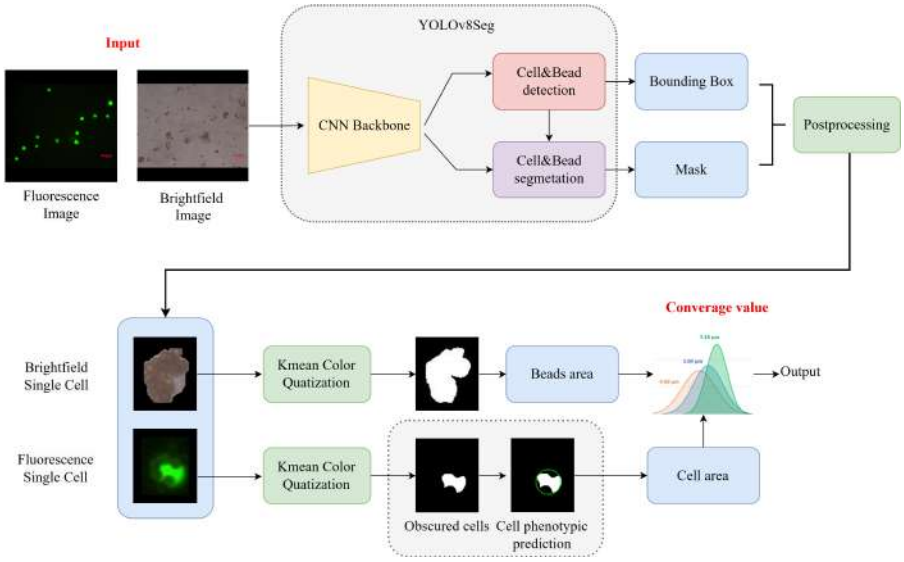

Figure 3.10: Schematic diagram of the detection and segmentation model for cells and magnetic particles

Images of the MBs–CTCs mixture were acquired using an inverted fluorescence microscope (CKX41, Olympus, Tokyo, Japan) combined with a CCD camera (DP71, Olympus, Tokyo, Japan) and connected to a computer running Olympus DP Controller software. The acquired images contained a mixture of MBs and A549 cells, simultaneously showing both cells attached to beads and uncovered cells. When a cell or cell fragment was not attached to any bead, its characteristic boundaries and internal structure could be clearly observed, similar to MBs not attached to cells.

To evaluate the inactivation and binding efficiency of MBs on A549 lung cancer cells (live cells), the study proposed a method using a combination of object detection and semantic segmentation techniques. This method aims to accurately identify A549 cells in the acquired microscopy image set and quantify the degree of MBs bound to each cell.

The acquired microscopy images include a mixture of cells bound to MBs, clusters of cells without MBs, and clusters of MBs not bound to any cells. The main objective of the study is to identify MBs–cell pairs using a specialized single-layer object detection model, where the output is bounding boxes corresponding to MBs–cells. From these bounding boxes, sub-images containing individual MBs–cells are cropped from the original image. This step helps eliminate most unnecessary objects, such as free MBs or cells not attached to MBs, from subsequent processing steps.

After separating the cropped images of each MBs–cell, a semantic segmentation model is applied to distinguish the region occupied by the cell and the region occupied by the MBs. The model generates masks after segmentation, and these masks are used to calculate the area covered by MBs on the cell. By aggregating the area data obtained from each MB attached to the cell, an approximate distribution can be estimated to

evaluate the efficiency of the attachment process.

In this image processing workflow, the YOLOv8 (You-Only Look-Once version 8) model is used as an object detection and segmentation tool, focusing on a single object class: cell clusters–MBs. YOLOv8 represents an advanced image segmentation model, enabling the identification and isolation of individual objects within an image. The output of the YOLOv8 model is then used to determine the location of cells in the fluorescence image. Next, the K-means algorithm is applied to separately segment the cell area and MBs area in the bright-field image, as well as to segment the cell area in the fluorescence image. The cell area segmented in the fluorescence image is used to estimate the actual cell area using the smallest-circle problem (finding the smallest circle that contains the cell).

The YOLOv8 model combines object detection and semantic segmentation within a convolutional neural network (CNN). The CNN in YOLOv8 generates low-resolution feature maps through convolutional layers, then gradually increases the resolution through successive layer sampling techniques. In this model's architecture, the convolutional layer builds masks for each pixel. Combined with bounding boxes and confidence scores, these masks are used to accurately identify and classify objects in images, effectively solving the segmentation challenge.

In this study, the main objective of the model is to detect and segment MB clusters associated with cells. The YOLOv8 model training dataset was labeled using the Roboflow tool, and the model was pre-trained on the large COCO dataset to improve learning efficiency. During image labeling, only cell-associated MBs were marked to ensure the model's specificity. The model's detection function plays a crucial role in eliminating non-cell-associated MB clusters, ensuring that only truly cell-associated MBs are accurately segmented. The model's output includes bounding boxes and pixel masks of cell–MB clusters, providing a comprehensive and accurate visual representation of these objects. The first stage involves detecting MBs–cell pairs using the YOLOv8 Object Detection model, an advanced object detection and image segmentation model developed by Ultralytics. This model uses an anchor-free approach, predicting the center of the object rather than relying on the difference from a predefined anchor box. This approach enhances the effectiveness of the subsequent post-processing step, called Non-Maximal Suppression (NMS). YOLOv8 is highly regarded for its speed, accuracy, and ease of use, making it the preferred choice for many applications in the field of computer vision. The output of YOLOv8 Object Detection is a set of bounding boxes surrounding objects in the image, accompanied by class labels and confidence scores for each box.

3.3.2 Machine learning model for classifying cell impedance signals

The electrical signals generated by the movement of cells across the sensor area were collected, processed, and analyzed. The passage of cells causes time-dependent changes in the output signal. Figure 3.11 illustrates the measured voltage change as a cell passes through the electrodes. The inset images show the cell's position at different locations corresponding to specific points on the voltage trace. The signal recorded by shows bipolar peaks, which result from the cell passing through both pairs of sensor electrodes. Positive peaks occur when the cell moves through the first pair of electrodes, while negative peaks are observed when it passes through the second pair. The baseline voltage, approximately 0.14 V, represents the offset voltage when no cell is present in the sensing region. This offset voltage may be due to defects in electrode fabrication or limitations in the accuracy of electronic components. The signal profile shows that the positive peaks have higher amplitudes than the negative peaks. The maximum voltage deviation from the baseline measured is approximately 1.4 V for positive peaks and 1.7 V for negative peaks. This amplitude difference is likely due to hydrodynamic forces acting on the cell as it passes through the electrode region, which may affect its relative vertical position within the microfluidic channel.

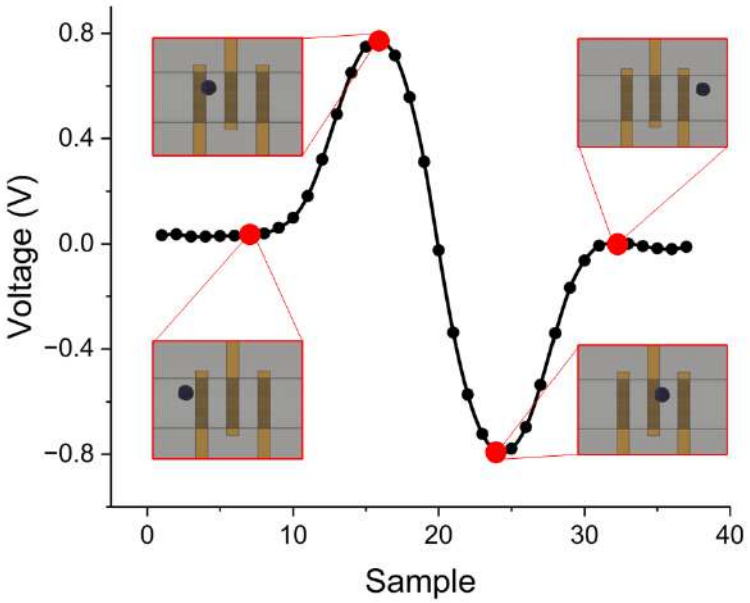

Figure 3.11: Changes in the output signal as the cell passes through the counting region; the insets in the graph indicate the cell's position corresponding to the output voltage at each point

Segmenting cell signals from data In the discrete time-series signal array collected from the microfluidic device, segmenting and classifying cell signals is essential to distinguish them from noise. In previous studies, cell counting was performed by evaluating the amplitude of positive peaks relative to a fixed threshold. However, this method has significant limitations when the data contains high-amplitude noise exceeding the predefined threshold. Furthermore, the characteristic signal shape, including successive positive and negative peaks (Figure 3.12), can be exploited as a distinctive feature to detect and count cells passing through the electrode more accurately. For each cell signal in the collected data array, key reference points are defined: Start Point (SP), End Point (EP), Positive Peak (PP), and Negative Peak (NP).

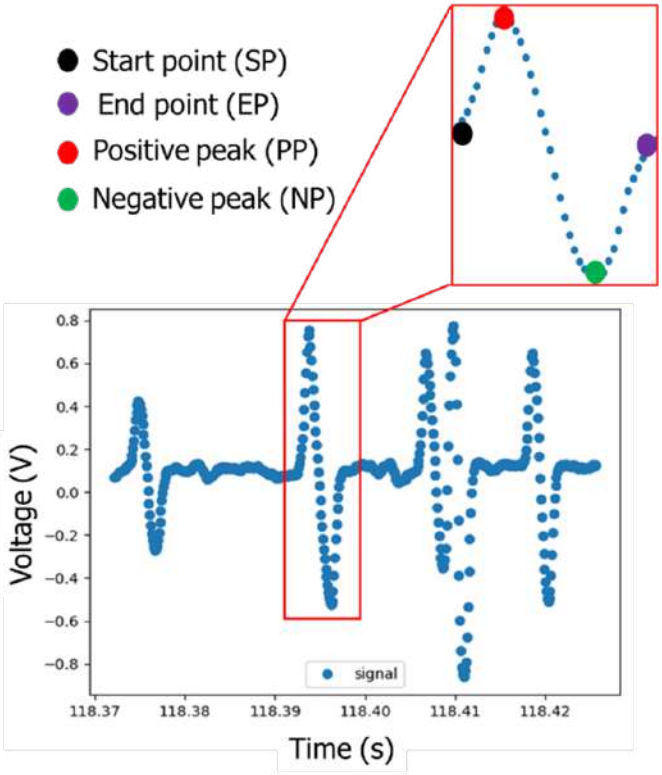

Figure 3.12: Define the segments of cellular signals in the data array. Each signal is characterized by a Start Point (SP), an End Point (EP), a Positive Peak (PP), and a Negative Peak (NP)

To construct this 2D signal segmentation model, the following specific conditions are established: The voltage values of SP and EP must be below the baseline (where the baseline is defined as the signal when the voltage value is approximately 0), the heights of PP and NP are required to be similar, and any waveform that deviates significantly from the bipolar shape is classified as noise. This refinement method improves the accuracy of cell detection and counting , while addressing the limitations of previous methods in noisy environments.

The signal recognition and extraction process is conducted in two main steps. Positive

peaks (PP) and negative peaks (NP) are identified using the find_peaks function (detecting local maxima in signal data) from the scipy library, specifically designed to detect peaks in signal data. Specifically, PPs are detected directly, while NP are determined by reversing the sign of the input parameter in the method. After PP and NP are collected, their number is reduced by removing identifiable noise peaks. The remaining PP and NP are then balanced in number and paired accordingly. These PP-NP pairs define the Start Point (SP) and End Point (EP) of the signal.The SP is determined by tracing back from the position of the PP until the downward trend of the voltage ends. Similarly, the EP is located by tracing forward from the NP until the upward trend ends. Finally, all data points from SP to EP are grouped into a vector, and this process is repeated until no more PP-NP pairs remain. Figure 3.13 illustrates the complete process of cell signal segmentation. First, peaks are identified from the entire signal (Figure 3.13a), and then the specific cell signal segments are extracted based on the identified start and end points (Figure 3.13b).

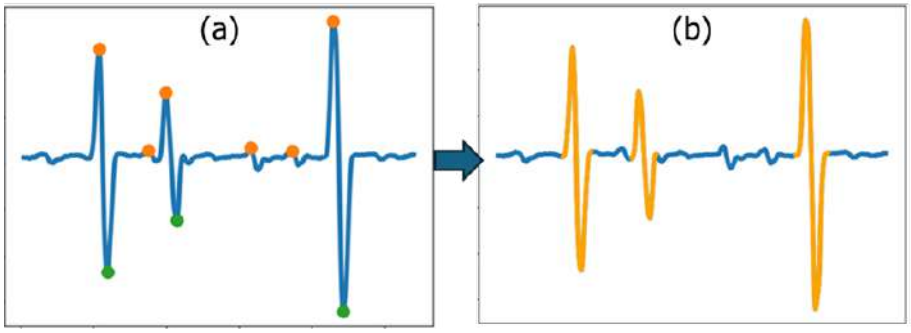

Figure 3.13: Cell signal segmentation process: (a) Identifying peaks from the entire signal; (b) Segmenting the cell signal

Feature description for machine learning models The preprocessing process filters out signal segments with peak patterns similar to those generated by cells. However, the segmentation model primarily removes background noise and measurement circuit noise. In reality, cells are not the only entities passing through the electrodes and generating such signal patterns. Specimens may also contain cell debris, cell clusters, dust particles, or other impurities that can produce electrical signals with similar shapes. Despite this overlap, each type of object in the sample exhibits distinct signal characteristics that can be leveraged for further classification. Since most detected objects are cells, specific signal features can be defined. Machine learning models can be applied to accurately determine whether a given signal corresponds to a cell if it lies within a defined convergence region. This method enhances the reliability of cell signal recognition while minimizing false positives caused by non-cellular artifacts.

In this study, signal features were defined and evaluated using over 1,000,000 data points collected from experiments.

The main features include:

- **Segment width:** represents the distance between SP and EP and provides important information about the duration of the signal in terms of time samples.
- **SP-EP deviation:** quantifies the voltage difference between SP and EP and serves as another key indicator.
- Discrete signal segments are also analyzed for smoothness to ensure their validity. Any anomalies or outliers causing a significant increase in the standard deviation (SD) of the signal segment are not considered valid cell signals.
- **Slope angles:** calculated as left-slope for SP-to-PP, mid-slope for PP-to-NP, and right-slope for NP-to-EP to capture the shape of the signal.

These features are described in Figure 3.14. Most signal cases filtered from raw data exhibit similar patterns for the defined features.

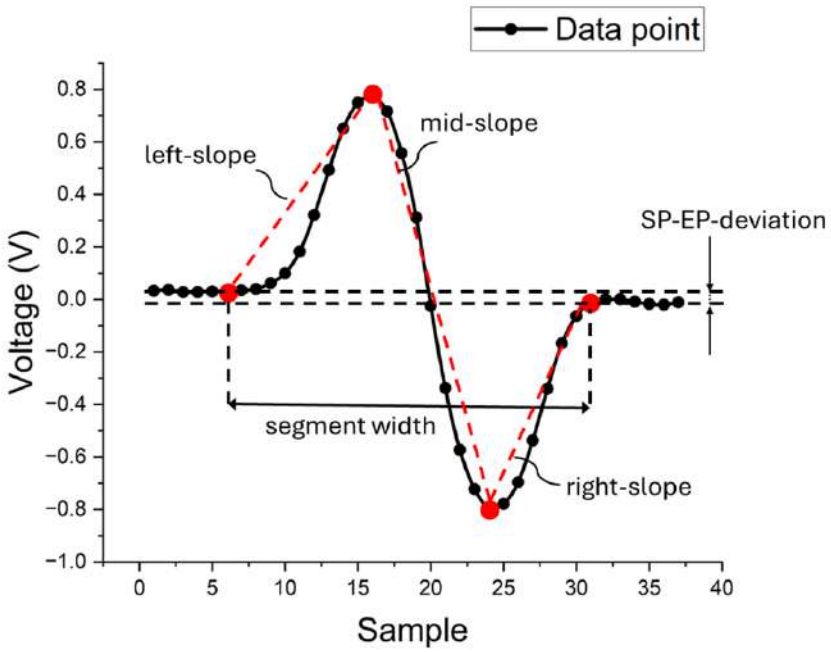

Figure 3.14: The defined features include: segment width (the horizontal distance between the Start Point and End Point); SP-EP deviation (the vertical distance between SP and EP); Standard Deviation (SD) of the data points; left-slope, mid-slope, and right-slope quantifying the slope angles of the peaks

Signal data generated as a cell passes through the electrode region provides valuable insights into individual cell characteristics. The amplitudes of PP and NP reflect both the relative height of the cell relative to the electrodes within the microfluidic channel and its overall size. Smaller cells or cells positioned farther from the electrodes produce

lower peak amplitudes, while larger cells or cells closer to the electrodes produce higher peak amplitudes in both the positive and negative directions. Furthermore, the flow velocity of the cells introduced into the microfluidic channel was maintained at a constant level throughout the experiment. As a result, the velocity of the cells within the channel remained nearly uniform. Signal width, defined as the time duration between SP and EP, measures the relative size of the cells in the experimental sample.

Deploying machine learning models After defining and extracting relevant features from the entire dataset, the data was applied to several widely used machine learning classification models to compare and evaluate their performance. The data used for training included two classes: the majority class, representing cases labeled as actual cell signals, and the minority class, representing cases labeled as noise. This study proposes two approaches for training machine learning models: one-class classification and binary classification. For the one-class classification method, models such as Isolation Forest and One-Class SVM are used to identify and isolate cell signal cases without explicitly relying on noise labels. Conversely, the binary classification method uses widely used models, including Decision Tree, Random Forest, Logistic Regression, Support Vector Classifier (SVC), K-Neighbors Classifier, and Gradient Boosting Classifier, to distinguish between cellular signals and noise cases. A comparative analysis of these two training strategies evaluates their effectiveness in handling imbalanced datasets and improving the accuracy of cell signal detection in microfluidic systems.

3.3.3 Machine learning model for cell counting in droplets

The method is based on the YOLOv5 object detection model. This is a deep learning model used for object recognition in images and videos. YOLOv5 is an improved version of YOLOv4. Version v5 is faster and more stable than previous versions and other models. This model excels at detecting small objects with high density. With its high customizability, YOLOv5 can be used to detect a wide range of objects in various fields. The structure of YOLOv5 is divided into three parts: the Backbone network, the Neck network, and the Head network (Figure 3.15). The input data, which is an image, will pass through these three main components and produce a prediction result regarding the location and type of objects detected by the model. The output will be a matrix containing vectors related to the center coordinates (x, y); the length and height of the object's bounding box (w, h); the accuracy probability of the prediction; and vectors related to the object's label. Depending on the configuration of the problem, the defined object classes will be different. The backbone network is the core part of the model, using a CNN (Convolutional Neural Network) to extract features from the input image. YOLOv5 uses a special CNN called CSP (Cross-Stage Partial) to speed up training and improve accu-

racy. The neck network is a part of the model that enhances object detection capabilities. The neck network is used to combine features from the previous layers of the model and create more complex features to make more accurate predictions about the location and type of objects. More specifically, this part includes a series of convolutional layers and some feature refinements to create features with greater depth. These features are then fed into several detection layers to determine the location and type of objects, thereby improving the model's object detection capabilities. Next, the Head network searches for regions of interest (ROIs) in the image using the anchor box algorithm to detect the location of objects. Then, bounding boxes are predicted for objects in the image using a subsequent CNN network. YOLOv5 uses a Siamese CNN network to predict bounding boxes for objects and improve accuracy. The advantage of YOLO is its fast processing speed, enabling real-time use while maintaining stable accuracy.

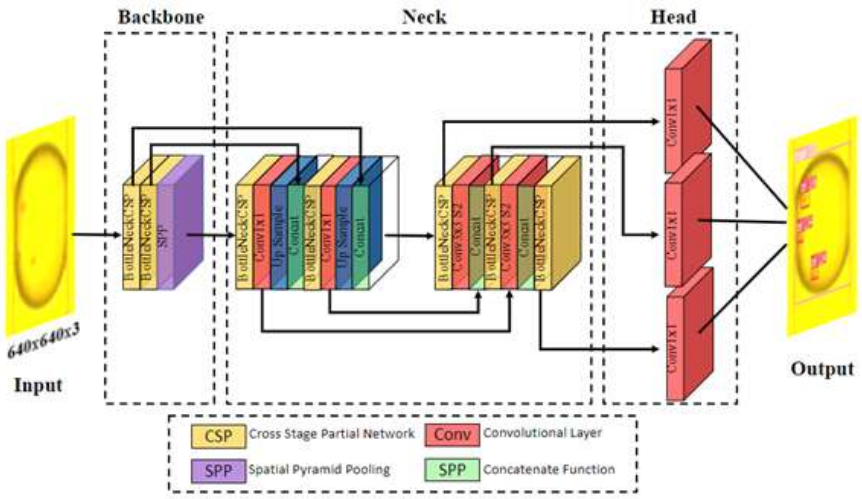

Figure 3.15: The structure of the YOLOv5 model in the problem

Two classes are defined in the problem: droplet and particle. Droplet detection can be fully achieved using the image processing steps, but we want to label both droplets and particles so that the model can learn the spatial correlation between these two objects, namely that particles are always enclosed within droplets to avoid mistaking stains on the channel walls for particles. Since the droplet size in a single frame is very small, the captured video has a resolution of 1280×800, while each particle occupies only 4×4 pixels. Therefore, to enhance the features the model can learn and standardize the input images for the YOLO model, an image processing procedure (Figure 3.16) is proposed to accurately detect the location of droplets, crop the image to focus on the droplets in the frame, and standardize the crop size so that all droplets appear in the center of the acquired image. From the input video frame, the image is converted to grayscale and blurred using the Gaussian Blur algorithm to reduce the brightness intensity of the channel

walls and other small objects to facilitate the Canny edge detection process. Subsequently, to connect any discrete elements of a droplet, morphological transformations are applied to fill the droplet's edges into a unified block. This makes it easy to find the contour and bounding box of each droplet. A sample image size is created by surveying all the maximum sizes of droplets that the channel can produce, which is 73×186 pixels. An offset is applied so that all sample images have this size and the position of the droplet is pushed to the center. The frame rate in the captured video is 30 fps (frames per second), but frames that are too close together will not differ significantly, so the sampling rate is reduced to $\sim$7 fps. This means that instead of capturing all frames appearing in the training video, only one frame is captured every four frames to ensure differences in shape. Thus, from the original 1-minute training video, 1076 images were obtained. These images were divided into three sets: train, validate, and test, with ratios of 80%, 10%, and 10%, respectively.

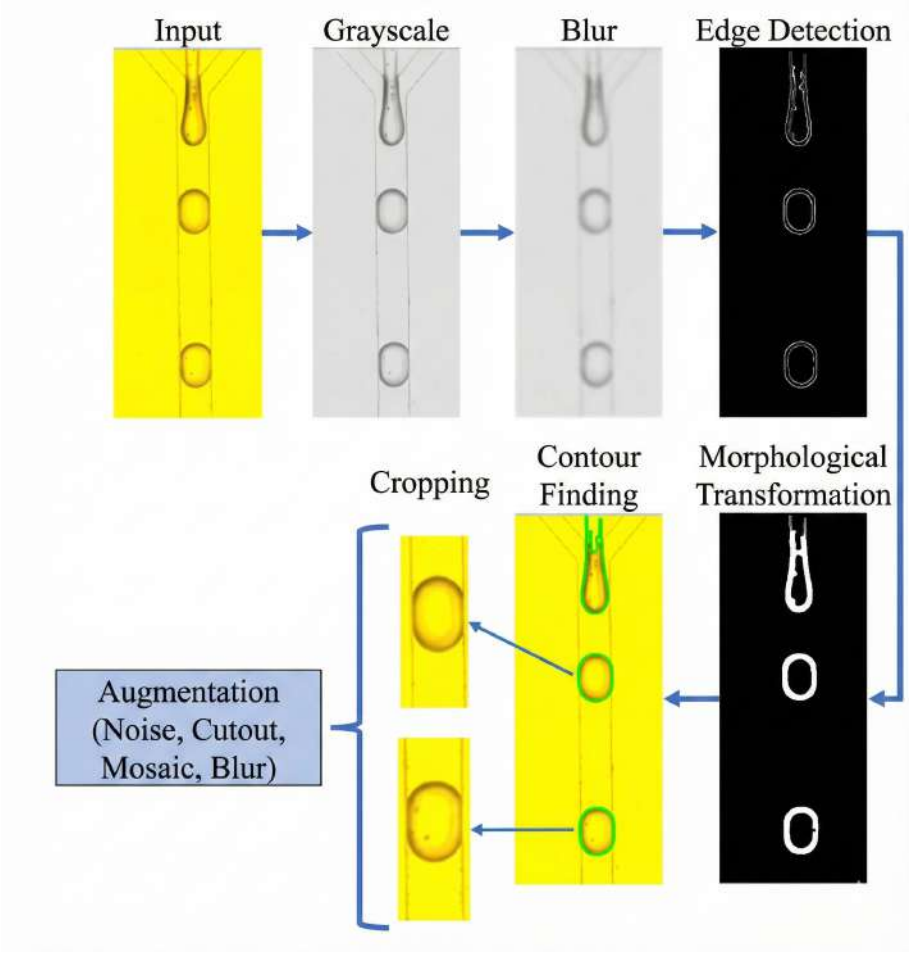

Figure 3.16: Image sampling process for droplets

To increase the number of samples for the deep learning model and avoid overfitting, thereby improving detection efficiency, several basic data augmentation algorithms were applied with specific effects as follows: Blurring: helps the model adapt better to small

changes in sample resolution (a), adds noise (b), cutout: helps avoid misdetecting droplets (c), and mosaic: helps detect droplets and particles even when partially missing (d) (Figure 3.17). Data augmentation is only applied to the training set, forcing the model to learn under more challenging conditions, while the validation and test sets are kept as close to real-world conditions as possible for accurate evaluation. The results yielded a total of 1576 images across all three datasets. Labeling the samples was performed with the support of the Roboflow platform, a tool that helps with labeling, preprocessing, and data enrichment. It also exports labeled files according to the YOLO model training standard. Each image has a labeled file with the number of lines corresponding to the number of objects in the image. Each line contains information about the object class and the object's position, standardized according to the image's width and height dimensions.

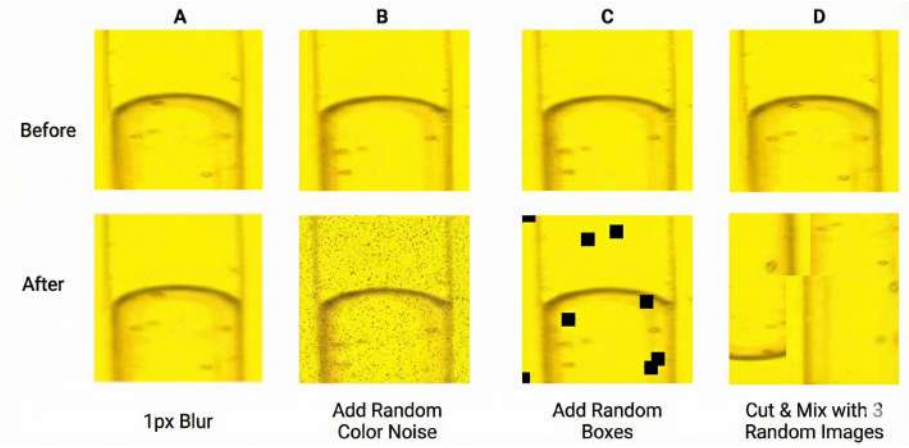

Figure 3.17: Data augmentation methods: A, Blurring; B, Noise; C, Cutout; D, Mosaic

Figure 3.18 shows a complete process from the sampling stage to checking the number of cells in each droplet. The labeled data (b) will be used to train the YOLOv5 model (c). Training is performed on the Google Colaboration platform with the support of a Tesla T4 16Gb GPU, PyTorch 1.13 + CUDA 116. Input images are normalized to a size of 640×640, with a batch size of 16. Training is performed for 100 epochs, then stopped and the weights with the highest accuracy are retrieved. The total training time was 2 hours. After training, the model's weights were used to make predictions for reference samples. A workspace with dimensions matching the image crop size of 73×186 was fixed at the channel location where there was minimal dust. Drops passing through this area are detected through image processing. Only when the drop is completely within the workspace is the image extracted and fed into the model for inspection. This is because the number of particles in the drop only fully appears on the workspace frame at that point. Drops passing through the channel appear multiple times in consecutive frames. However, since there is no difference between frames that are too close together, instead of taking

them continuously, every 4 frames are sent for inspection. On average, a droplet passing through the channel will be inspected 3-6 times. Each time will be a conclusion about the number of particles, these numbers will be averaged and rounded to the threshold. The rounded value will be taken at a threshold of 0.4, biased towards more droplets, because detecting a droplet containing a particle requires a minimum of confusion, and there are cases where particles stick to the channel wall and are very difficult to detect. Therefore, as long as they appear in a few frames, the average value will tend to increase towards a higher quantity. And this is their true quantity. The threshold value has been investigated and shown to be effective.

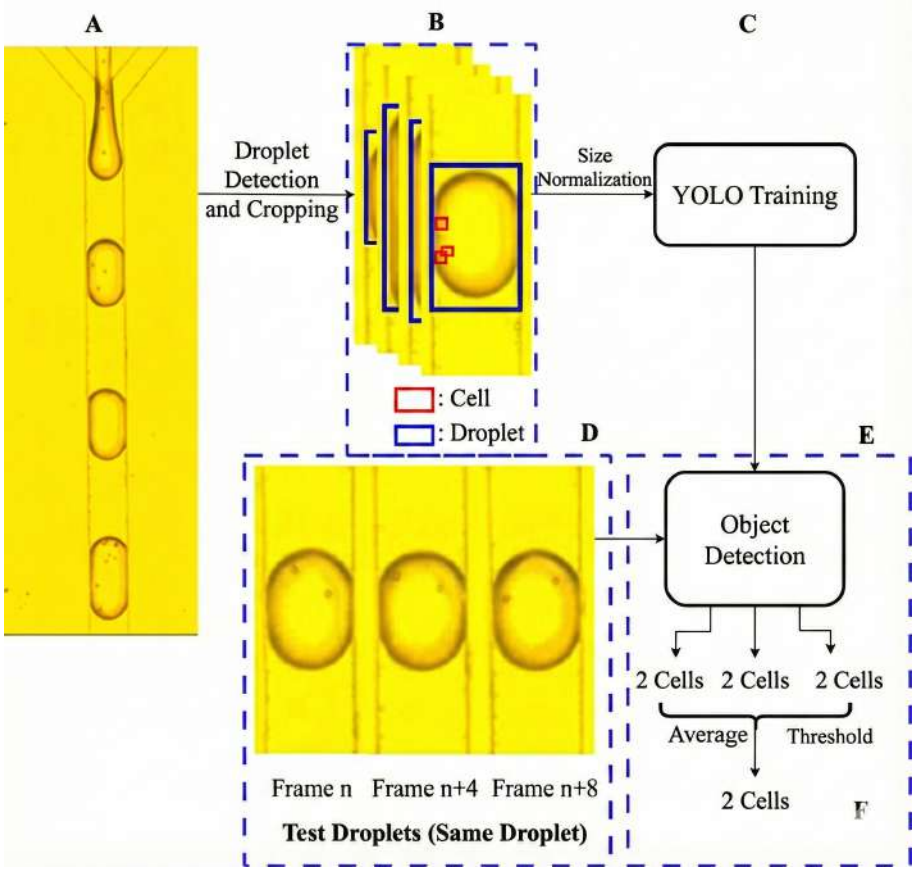

Figure 3.18: Process for counting the number of particles in a droplet: A, Original video frame; B, Data labeling; C, YOLO training; D, Test sampling; E, Sample content conclusion

3.4 Conclusion

This chapter has presented the complete experimental implementation of the proposed Lab-on-a-Chip platform, from material preparation and device fabrication to automated signal acquisition and processing. Using standard soft lithography techniques with SU-8 masters and PDMS casting, the microfluidic modules for magnetic separation, inertial

focusing, and droplet generation/sorting were successfully fabricated, bonded, and interfaced with the custom impedance electronics and optical imaging system. The resulting LoC device provides a stable, reconfigurable platform capable of operating with real biological samples, enabling reproducible studies of bead–cell binding and single-cell electrical characterization.

In parallel, an end-to-end signal processing and data analysis pipeline was developed to transform raw images and impedance waveforms into quantitative, machine-readable descriptors. Deep learning-based image analysis was implemented by integrating a YOLOv5 architecture for robust bead enumeration in static chambers and moving droplets, while a One-Class Support Vector Machine (OC-SVM) model was employed to automatically detect, validate, and classify impedance pulses corresponding to single-cell events. These methodologies constitute core technical contributions of the dissertation and correspond directly to the authors publications [P1], [P2], [P3], [P4], [P5], and [P6].

Chapter 4

RESULTS AND DISCUSSION

4.1 Lab-on-Chip Fabrication Results

Figure 4.1 presents the results of the microfluidic chip following fabrication. The entire microfluidic system was designed with overall dimensions of 75×25 mm and a microfluidic channel height of 30 µm, ensuring a balance between flow capacity and cell flow control. In the magnetic filtration region, the channel was configured as a parallel bend with a channel width of 100 µm. The results demonstrate that the channel loops are clear and uniform, facilitating flow redistribution and minimizing wall adhesion. Subsequently, the channel gradually narrows through transition segments at the entrance to the cell orientation region.

After passing through the narrow section at the exit of the mixing and cell flow adjustment region (with a minimum width of only 30 µm), the single-cell stream moves under the action of flow, passing successively through the impedance sensor region. The narrowing width (30 µm) renders the channel cross-section approximately the size of a typical cell, compelling the cells to move in a nearly single-file manner and minimizing the phenomenon of overlapping or parallel movement of multiple cells in the measurement region. This configuration is particularly significant for impedance-based cell counting modules, as each recorded signal pulse corresponds almost exactly to a single cell, thereby substantially improving the accuracy and resolution of the analysis. Downstream, the channel widens again to 100 µm before the droplet formation region and to 300 µm in the classification region, where droplets are separated based on the principle of dielectrophoresis (DEP) technology. Modifying the channel width in this T-shaped region facilitates mixing with the oil phase in subsequent experimental sections.

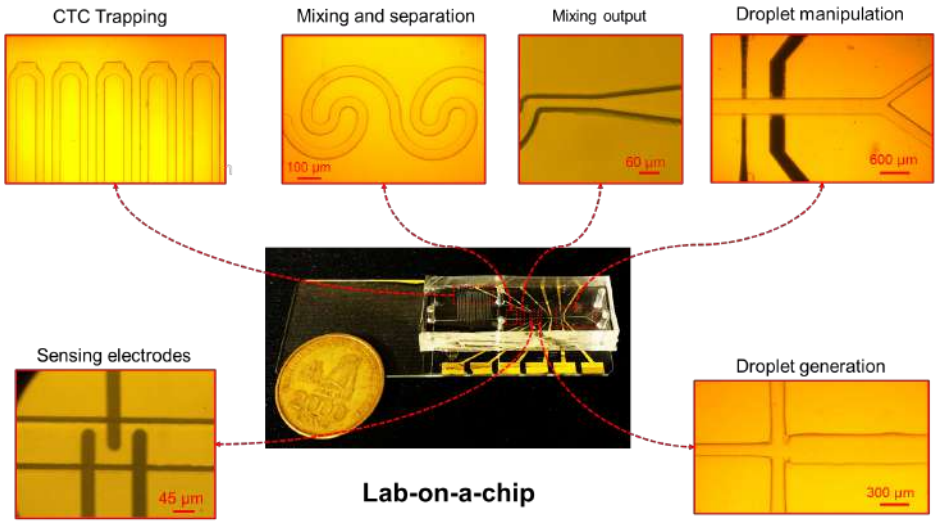

Figure 4.1: Results of the LoC chip after fabrication.

4.2 Modeling and Simulation Results

4.2.1 Modeling and Simulation Results of the Magnetic Separation Structure

Figure 4.2 illustrates the magnetic field intensity generated by a 0.5 T magnet positioned 3 mm away from the channel cavity. The magnetic field intensity decreases as the distance from the microchannel to the magnet increases. Within the internal structure of the channel, the cavities closest to the magnet experience a relatively large magnetic field, causing the particles to undergo maximum magnetic force. Consequently, cells attached to magnetic particles in the vicinity of the magnet are effectively captured. The average magnetic flux density at the capture region is estimated to be approximately 0.103 T, generating magnetic forces of approximately 2.1×10^{-11} N, 2.7×10^{-11} N, and 3.0×10^{-11} N (directed toward the magnet) on magnetic bead (MB) particles with sizes of 1.36 μm, 3.00 μm, and 4.50 μm, respectively. Conversely, the remaining regions in the channel exhibit higher flow velocities, which enhance the transport of both sample and non-target particles, as illustrated in Figure 4.2B. By leveraging the different flow conditions within the channel, this optimized design improves the overall efficiency of collecting and separating target cells from the mixed sample.

The low particle velocity in the chambers due to flow conditions also facilitates easier magnetic capture of targets. Conversely, the remaining regions in the channel exhibit higher flow velocities, enhancing the transport of sample and non-target particles, as depicted in Figure 4.2B. By utilizing different flow conditions within the channel, this optimized design improves the overall performance of capturing and separating target cells from a mixed sample. Three particle types were simulated simultaneously in the proposed structure, as shown in Figure 4.2C. The chambers are numbered from 1 to 10 in

the flow direction. Particle colors are represented based on particle diameter properties in COMSOL software. The distribution of MB 4.50 μm cells (red dots) is concentrated in the upstream chambers (1–6), while MB 3.00 μm cells (green dots) appear from compartment 1 to 9, and MB 1.36 μm cells (blue dots) are distributed throughout all compartments (1–10). The distribution results indicate that cells containing larger MBs experience greater forces and are therefore more likely to be trapped in the first compartments they encounter. Conversely, for small particles (1.36 μm), the cells experience relatively modest forces and are partially transported out through the exit due to drag forces.

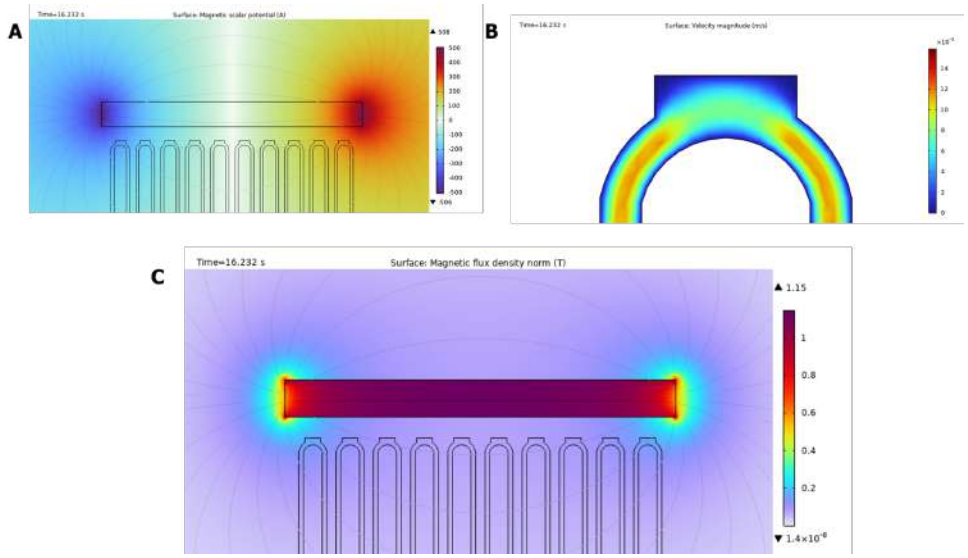

Figure 4.2: Simulation results for MB cell particles: A) Magnetic field intensity distribution across the microchannel area, B) Particle velocity in the proposed microchannel is low in the capture zone and high in the remaining zone, C) Magnetic flux density and particle distribution in the microchannel.

These findings are consistent with the magnetic force acting on the particles, indicating that even with changes in particle diameter and associated drag forces, magnetic force remains the dominant factor influencing capture efficiency. The simulations conducted in this study provide a fundamental theoretical framework that clarifies the operating principles, serving as a basis for predicting and optimizing device performance prior to conducting actual experiments.

4.2.2 Modeling and Simulation Results of the Impedance Sensor Structure

Figure 4.3 illustrates the electric field distribution of the sensor structure, depicting the electric field intensity both in the air region and the space between the excitation electrode and the sensor electrode. The visual representation demonstrates the coverage range of the electric field, indicating its presence and influence on the designated area within the

sensor structure. This comprehensive description facilitates understanding of the spatial characteristics and range of the electric field, providing insights into how it interacts with the surrounding environment and potential targets, such as biological cells in a fluid stream.

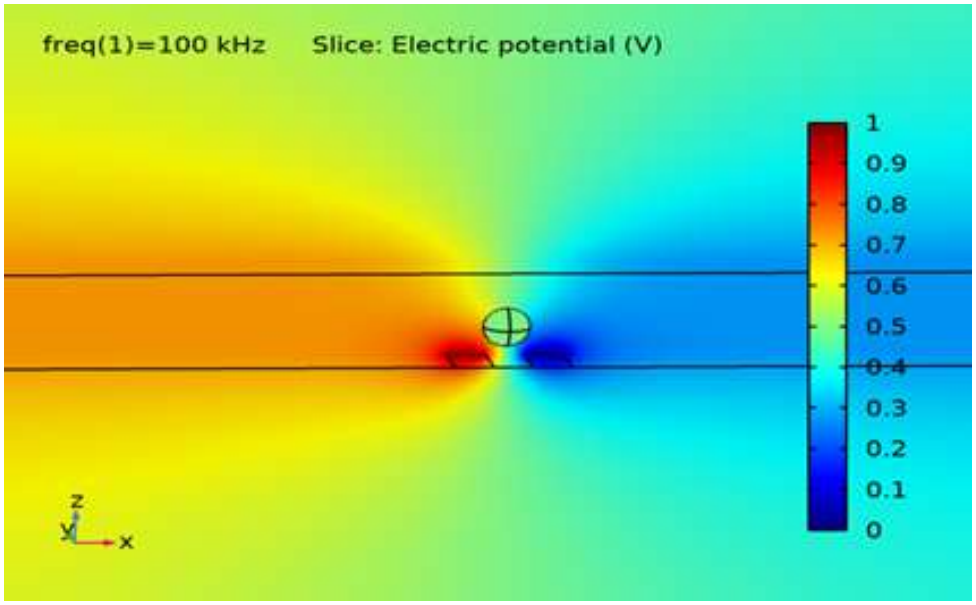

Figure 4.3: Potential distribution.

The change in impedance ΔZ is calculated as the difference between the impedance Z_A obtained when the A549 cell passes through the sensor structure in an 8.6% sucrose environment and the impedance Z_B obtained when no A549 cell is present in the channel with an 8.6% sucrose environment:

$$|\Delta Z| = |Z_A - Z_B| \tag{4.1}$$

The signal obtained when the A549 cell passes through the impedance sensor region at a stimulation frequency of 100 kHz in an 8.6% sucrose buffer solution exhibits a symmetrical pulse shape around the 0 µm position on both electrode structures. The change in impedance due to the movement of A549 cells through the sensor region in the real part is ΔR, also known as the change in resistance. The change in impedance in the imaginary part ΔX is also known as the change in reactance.

From the above analysis, it can be concluded that the electrode structure with a size and spacing of 15 µm provides a larger impedance signal, a more distinct pulse amplitude, and a more compact sensing area, rendering it the optimal choice for the A549 cell counting module based on impedance in an 8.6% sucrose solution. This structure not only significantly improves the sensitivity and reliability of the measurement but also creates favorable conditions for the subsequent step of packaging single cells into droplets in microfluidic modules.

This simulation provides survey results on the impedance changes of the sensor under specific frequency conditions, revealing significant changes in both resistance and impedance parameters. Understanding these impedance variations, particularly in response to simulated cell movement, contributes to a more comprehensive understanding of sensor operation and supports design refinement for optimal performance. The observed changes emphasize the sensor's sensitivity to the presence of cells, further highlighting the potential utility of this technology in applications requiring accurate cell detection in microfluidic environments.

Figure 4.4 illustrates the electric potential distribution and field lines within the microfluidic channel, highlighting the influence of cells encapsulated in microdroplets on the electric field. The presence of cells introduces localized inhomogeneities in the electric potential, leading to a concentration of field lines around each cell. As the number of encapsulated cells increases, the electric field becomes significantly distorted, with noticeable changes observed in the field lines. These distortions reflect the complex interactions between the electric field and biological cells, which play a critical role in achieving high accuracy in impedance measurements. An important observation is the strong correlation between the position of cells within the droplet and the peaks in the impedance signal. This underscores the necessity of accounting for both the number and spatial arrangement of cells within the droplet, as these factors directly influence the efficiency of impedance-based detection systems. The presence of high-conductivity objects, such as cells with cytoplasmic conductivity of 0.5 S/m, significantly reduces the average conductivity of droplets compared to empty droplets.

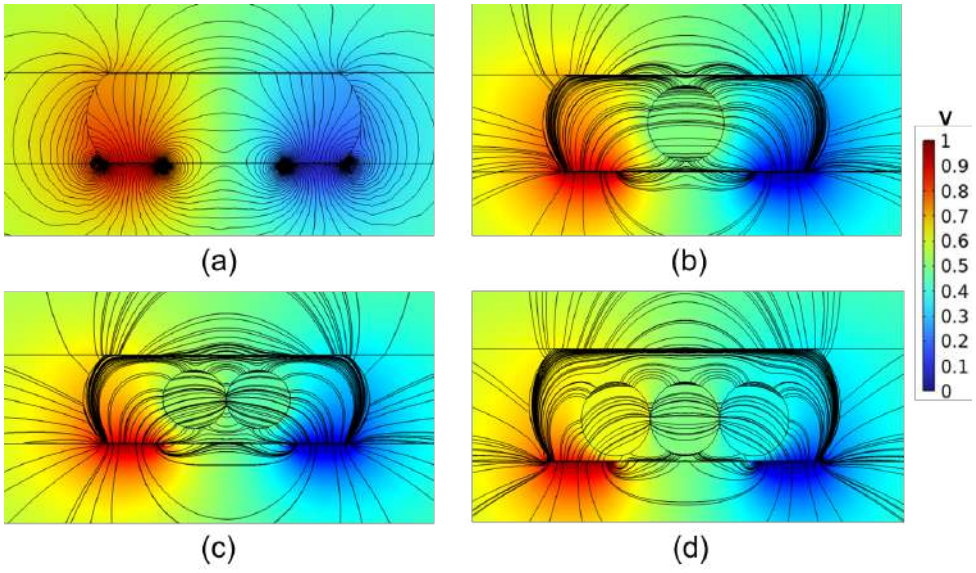

Figure 4.4: The electric potential and electric field line distribution according to the droplet with: (a) no encapsulated cell; (b) 1 encapsulated cell; (c) 2 encapsulated cells; (d) 3 encapsulated cells

However, since the conductivity of the buffer solution is typically higher than that

of the cytoplasm, encapsulated cells are often short-circuited by the surrounding solution, rendering detection through impedance analysis more challenging. Additionally, the permeability of the cell membrane facilitates ion exchange between the high-conductivity cytoplasm and the low-conductivity aqueous buffer, further complicating the detection of encapsulated cells. In the case of multiple encapsulated cells, the average conductivity of the droplet increases, and the effective electrical detection volume becomes larger. This results in a reduced serial resistance between the cells and the electrodes, producing a more pronounced impedance signal. Optimizing system parameters to enhance sensitivity in detecting encapsulated cells within droplets is therefore essential. To achieve high efficiency in classifying the number of cells within microdroplets, factors influencing the electrical properties of cell-encapsulated droplets, including the buffer solution, electrode spacing, and excitation frequency, were simulated and investigated.

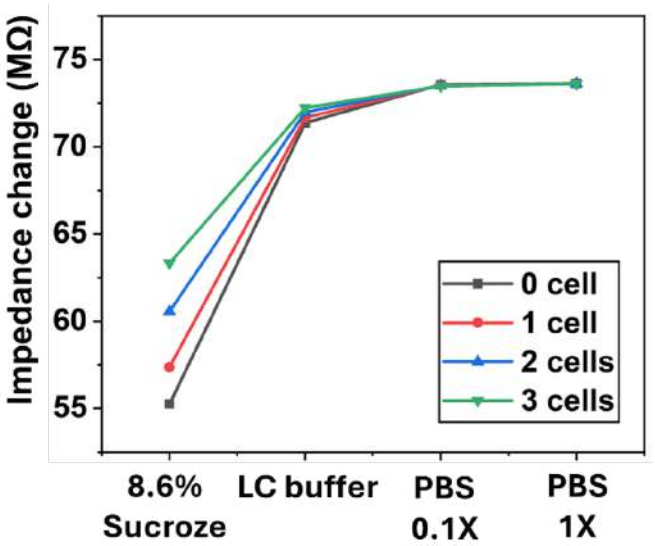

Figure 4.5: Comparison between different solutions when droplets at the center of the sensing region with different cell numbers at 500 kHz.

Various buffer solutions were examined to evaluate impedance changes at a frequency of 500 kHz in microdroplets containing different numbers of encapsulated cells. The investigated buffers included 8.6% Sucrose, LC buffer, PBS 0.1X, and PBS 1X, as shown in Figure 4.5. Each buffer possesses distinct properties that render it suitable for specific applications in microfluidic research and impedance-based cellular analysis. Sucrose 8.6% features low conductivity and is ideal for stabilizing microdroplets. LC buffer offers moderate conductivity and helps reduce noise while optimizing signal quality. PBS 1X simulates physiological conditions with high conductivity. PBS 0.1X, as a diluted variant, enhances sensitivity in measurements. The results demonstrated a progressive increase in impedance change with higher buffer conductivity, from Sucrose 8.6% to PBS 1X. Droplets containing more cells exhibited significantly larger impedance changes.

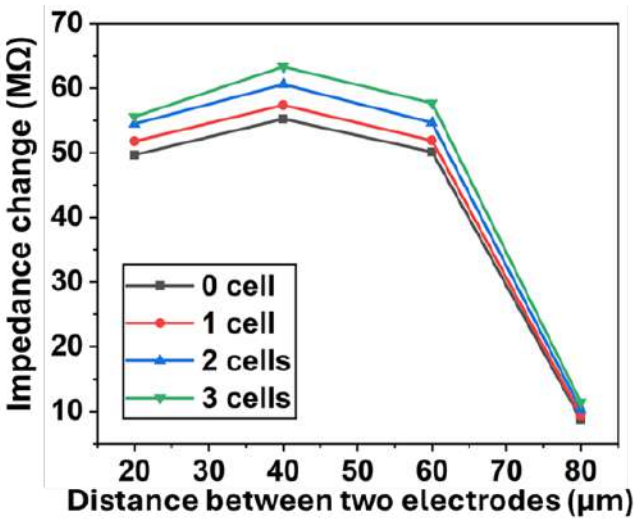

Figure 4.6: The impedance change depends on the distance between the two electrodes.

The distance between electrodes in biomedical impedance sensor experiments significantly impacts impedance measurements, as it directly influences the system's sensitivity and the interaction between the electric field and the sample. When the electrode distance is too small, the electric field becomes more concentrated, enhancing sensitivity to subtle changes in the electrical properties of the droplet or cell. However, excessively small distances may lead to signal saturation or localized noise, reducing measurement accuracy. Conversely, when the electrode distance is too large, the electric field intensity diminishes, resulting in decreased system sensitivity. In such cases, the measured signal may weaken, rendering it challenging to detect impedance changes caused by the sample. Additionally, a larger distance can lead to uneven electric field distribution, compromising the stability of the system. Optimizing the electrode spacing is therefore essential to achieve a balance between sensitivity, signal strength, and field uniformity, ensuring precise and reliable impedance measurements.

In this study, the electrode spacing was investigated under varying cell counts within droplets to determine the optimal distance for droplet classification (Figure 4.6). The analysis included four cases: droplets with no cells and those containing one, two, and three cells. As the electrode spacing increased from 20 µm to 40 µm, the impedance change progressively increased across all configurations, reaching its maximum at a spacing of 40 µm. However, further increasing the spacing to 80 µm led to a significant decrease in impedance change. These results indicate that electrode spacing plays a critical role in the impedance response, with an optimal spacing of 40 µm providing the highest sensitivity. Additionally, droplets with higher cell counts consistently exhibited greater impedance changes at all electrode spacings, highlighting the influence of cell quantity on the electrical properties of the system.

The data presented in Figure 4.7 illustrate the impedance profiles of droplets contain-

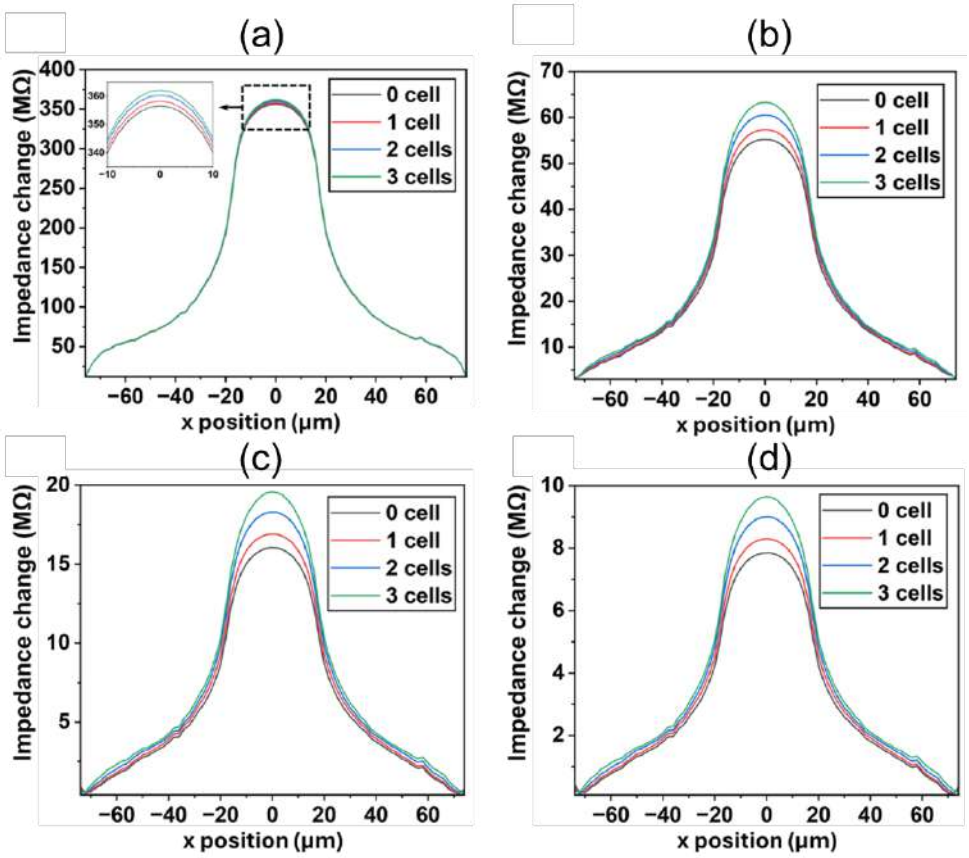

Figure 4.7: The impedance change with 8.6% Sucrose Solution at (a) 100 kHz; (b) 500 kHz; (c) 1.5 MHz; (d) 2.5 MHz

ing varying cell counts in an 8.6% Sucrose solution across four distinct frequencies: 100 kHz, 500 kHz, 1.5 MHz, and 2.5 MHz. At 100 kHz, the impedance profiles exhibit distinct and sharp peaks, with the maximum impedance change for droplets containing three cells reaching approximately 360 MΩ, compared to approximately 355 MΩ for droplets without cells. Although the absolute impedance values are high, the differences between droplets with varying cell numbers remain relatively small. At 500 kHz (Figure 4.7b), the overall peak amplitude decreases, yet the difference between droplets with and without cells becomes more pronounced. This indicates that, despite the smaller absolute peaks, the contrast at 500 kHz provides better discrimination between droplets containing different numbers of cells. At higher frequencies, such as 1.5 MHz and 2.5 MHz (Figures 4.7c and 4.7d), the impedance profiles converge significantly. For instance, at 1.5 MHz, the maximum impedance change for droplets with three cells decreases to approximately 25 MΩ, and the differences between profiles for varying cell counts become less distinct. By 2.5 MHz, the profiles are even closer, with a maximum impedance change of approximately 20 MΩ for three-cell droplets and minimal variation between profiles corresponding to different cell numbers. This behavior highlights the trade-off between sensitivity and operational frequency. Lower frequencies, such as 500 kHz, offer greater differentiation and precise cell detection but may involve slower signal acquisition and higher variability. In contrast, higher frequencies reduce sensitivity but enable faster data acquisition and improved stability.

4.2.3 Modeling and Simulation Results of Droplet Separation Structure

The simulation results illustrate the droplet separation phenomenon resulting from the complex interaction between the electric field and the droplet's dynamic behavior in the microchannel environment (Figure 4.8). The electric field is represented by a color map, demonstrating the intensity of the electric field around the deformed droplet and clarifying the droplet's polarization in the electric field. These representations highlight regions of high and low potential, contributing to the elongation and deformation of the droplet. Time-series images of the deformation and separation process at different time intervals illustrate the progression from the initial state, through the elongation phase, to complete droplet separation.

The droplet separation phenomenon was also calculated through simulations to investigate the ratio of droplets formed. First, simulations were performed to calculate the changes in the droplet object inside the channel under the pressure of the electric field over time. The time parameter input into the simulation ranged from 0 to 110 ms, with the interval between each calculation set at 5 ms to ensure the accuracy and detail of the simulation results. This approach enabled the research team to analyze the phenomena

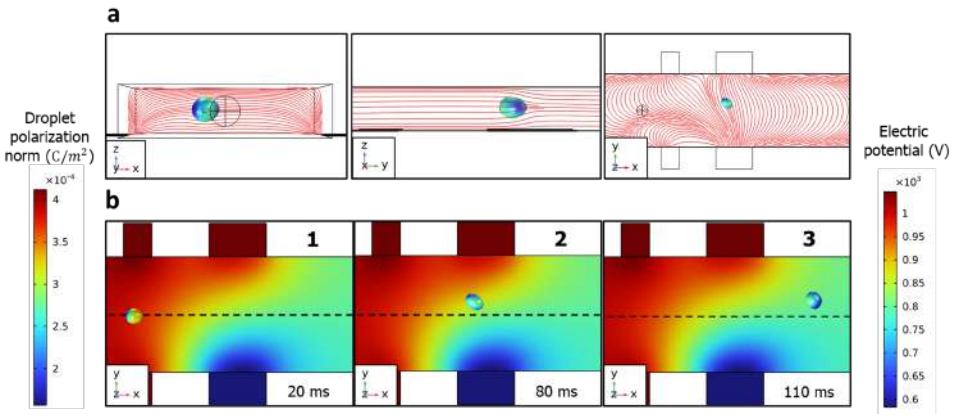

Figure 4.8: Simulation results of the electrostatic force controlling the droplet's trajectory.

inside the channel in greater depth.

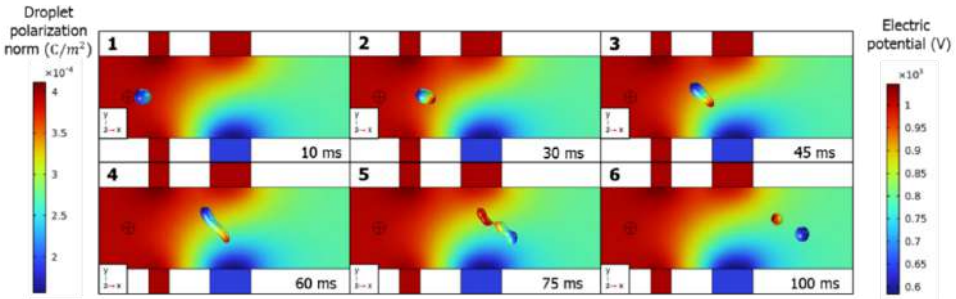

Figure 4.9: Simulation results describing the potential and dynamic behavior of a droplet in a DC electric field.

The simulation results (Figure 4.9) illustrate the droplet separation phenomenon resulting from the complex interaction between the electric field and the droplet's dynamic behavior in the microchannel environment. The potential is represented by a color map, demonstrating the intensity of the electric field around the deformed droplet and highlighting the droplet's polarization in the electric field. These representations indicate regions of high and low potential, contributing to the elongation and deformation of the droplet. The potential used in the simulation is 1300 V, a level sufficient to generate the electric force required to split the droplet into two smaller droplets. Time-lapse images of the droplet deformation and splitting process at different time intervals illustrate the droplet's states from the initial stage, through the stretching phase, to the point where it completely splits into two droplets. The image sequence demonstrates the electrostatic force, governed by the Maxwell stress tensor, acting on the droplet, causing it to stretch and ultimately split.

In the images at 30, 45, and 60 ms, the droplet gradually deforms more strongly over time as it approaches the region of strong electric field. The increase in droplet deformation can be explained by the increase in capillary electric force (Equation 15). This number is always maintained below the threshold that could cause droplet instability

(e.g., the Quincke phenomenon) or droplet breakup (the droplet breaks into many small, uncontrollable droplets). At 75 ms, the narrow region in the middle of the droplet is subjected to electric forces and viscous shear forces, causing the narrow region to shorten. When the external force exceeds the surface tension, the droplet is no longer in a stable deformed state and will split into two droplets, with the two ends separating. Finally, at 100 ms, the two droplets have been successfully separated under the action of the electric field. The simulation results demonstrate that the microchannel structure for droplet separation can be implemented in a practical system.

The diameter of the two droplets depends on the volume of liquid in the spatial region with coordinates defined by x_{sc}, which represents the separation region between the two droplets. The volume of the droplet is calculated by integrating the level-set function (ϕ_{ls}) with a value greater than 0.5. The formula for calculating the droplet diameter is as follows:

$$d_{first\ droplet} = 2 \times \left(\left(\int_0^1 (\phi_{ls} > 0.5) \times (x > x_{sc}[mm]) \right) \times \frac{3}{4\pi} \right)^{\frac{1}{3}} \tag{4.2}$$

$$d_{second\ droplet} = 2 \times \left(\left(\int_0^1 (\phi_{ls} > 0.5) \times (x < x_{sc}[mm]) \right) \times \frac{3}{4\pi} \right)^{\frac{1}{3}} \tag{4.3}$$

In the simulation case of Figure 4.10 , the ratio between the two droplets is approximately 0.4. The simulations show that using a single voltage value for the three electrodes cannot produce two droplets of equal size. When the applied voltage to the three electrodes exceeds 2000 V, the simulation results also show the phenomenon of droplets sticking to the bottom of the channel due to excessive electrostatic force and DEP force. This significantly reduces the effectiveness of controlling the droplet inside the microchannel. Furthermore, in practice, applying too strong a voltage to the electrodes will affect the object inside the droplet and the durability of the electrodes used.

To better control the size ratio of the two droplets, the research team changed the input voltage parameters to two values: V_S is the voltage applied to the two small electrodes, and V_L is the voltage applied to the large electrode. V_L was kept constant at 1300 V, and the V_S parameter was varied from 600 V to 1560 V. Investigating these voltage ratios on the simulation system helped determine the necessary voltage ratio for the actual system. The calculations were performed and the results obtained are as follows and the corresponding images of the droplets are also shown. At low $V_{(S)}/V_{(L)}$ratios, the sizes of the two droplets are quite similar, with a ratio above 0.6. In these cases, the two electric forces acting on the polarized half-droplet are not too strong and cause the narrow region of the droplet to be most strongly affected by the viscous shear force near the center of the droplet. This causes the two separated droplets to have equal ratios. Notably, at a voltage ratio of 0.55, the size similarity of the two droplets is highest, with a ratio exceeding 0.9.

We can see that with a low voltage ratio between $V_S$and V_L, the ability to separate

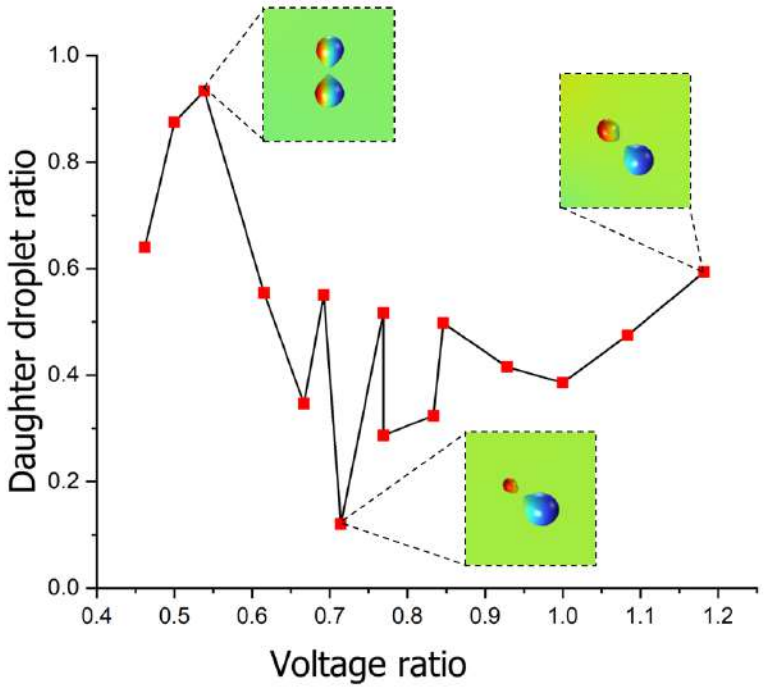

Figure 4.10: Simulation results of the ratio of droplets formed with different voltage ratios applied to the electrodes.

droplets evenly is higher; however, with an excessively low ratio, the two electric forces are not strong enough to separate the droplets. When V_S is too low, the polarization on the droplet decreases, making the droplet less affected by the electric force, and at that point, the droplet separation capability of the system is not guaranteed. As the voltage ratio increases, the ratio of the two droplets gradually decreases below 0.6. The electric force is stronger at higher voltage ratios, causing the droplet to stretch unevenly and the strongly polarized half to deviate more than the other half. In fact, at a voltage ratio of 0.7, the separated droplet has a ratio below 0.2, and the volume of the original droplet remains almost unchanged. At other voltage ratios, the separation of the two droplets is uneven, and the ratio ranges from 0.3 to 0.6. These simulation results will help the research team optimize the voltage used in the actual system according to the desired droplet ratio. These ratios will be used in experiments to demonstrate the effectiveness of droplet control in microdroplet separation systems using non-uniform electric fields.

The simulation results in this study provide a deeper understanding of EHD phenomena in droplet separation techniques using an uneven electric field. The Navier-Stokes equation, Maxwell stress tensor, and parameters calculated in the simulation model provide a solid theoretical basis to help the research team control the internal factors in droplet separation techniques. Concurrently, these results also provide information on the influence of parameters such as the voltage ratio between electrodes on the droplet separation process and the degree of droplet deformation at different potentials. The

simulation results also indicate that there is an optimal voltage limit for the droplet separation process, where the droplets can be controlled with the most uniform size ratio. These results not only provide a clear understanding of the physical mechanism behind the EHD phenomenon in droplet separation but also open up the possibility of optimizing droplet separation systems in practice, particularly in applications requiring droplet size uniformity such as in microfluidics research and biological and medical applications.

4.3 Experimental results and signal processing machine learning models

4.3.1 Magnetic separation results

Results of magnetic particle binding to lung cancer cells

The results of the incubation and binding of immunomagnetic beads (IMBs) to the surface of A549 cancer cells are presented in Figure 4.11. The use of a combination of different imaging modes is an important methodology, with each mode providing a distinct layer of information. Brightfield imaging allows confirmation of the physical presence and distribution of non-fluorescent magnetic particles; fluorescence imaging helps accurately locate labeled living cells and confirm their identity; while integration imaging plays a crucial role by superimposing the two information channels, providing indisputable visual evidence of co-localization between magnetic particles and cells, thereby confirming a successful binding. This multi-channel method allows for accurate identification of objects even under complex conditions such as cell clumping or rupture. Through visual observation, cells in all three test samples with different particle sizes showed effective binding with magnetic particles, with no cases of target cells failing to bind. At 40x magnification, confirming the presence of magnetic particles became straightforward, particularly for particles sized 3.00 µm and 4.50 µm, facilitating subsequent quantification.

Morphological analysis of the 2D images showed that the cells were nearly round, and the distribution of magnetic particles tended to depend significantly on size. For larger particles (3.00 µm and 4.50 µm), they mainly concentrated and adhered to the outer edge of the cell membrane. This phenomenon can be explained by physical and biological factors, including steric hindrance, which makes it difficult for large particles to access recessed areas on the cell surface, and the possibility that receptors on the cell membrane are unevenly distributed, concentrating more in areas with greater curvature. Although some particles penetrate into the central region of the cytoplasm on a few cells, distribution at the periphery remains clearly dominant. Conversely, particles of smaller size (1.36 µm) were observed to be distributed across the entire cell surface. This may be due to their higher surface area-to-volume ratio, allowing interaction with more binding

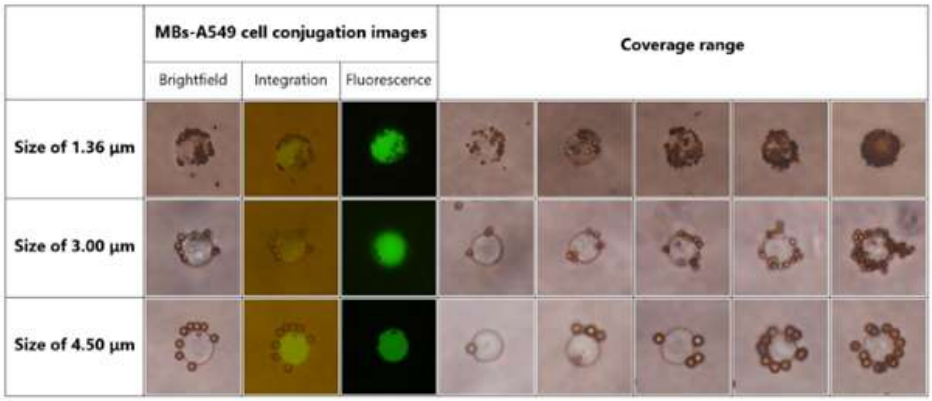

Figure 4.11: Results of magnetic particle-A549 cell binding with different particle sizes (1.36 µm, 3.0 µm, 4.5 µm).

sites, while stronger Brownian motion facilitates their diffusion and access to different regions of the cell membrane. However, there still appears to be a tendency for greater concentration in peripheral regions, evidenced by the fact that in cases where cells bind to only a small number of particles, these particles mainly accumulate at the outer edges rather than at the center, suggesting that initial binding is likely to occur at the periphery.

To quantify the degree of particle coverage on the cell surface—a key parameter reflecting the potential to generate sufficient magnetic force for separation—a coverage ratio index was calculated. This parameter was determined by the ratio of the total surface area occupied by magnetic particles to the total surface area of the cell under investigation. A diverse set of individual cell samples (approximately 100 samples per type) was analyzed to ensure the statistical reliability of the results. Due to the large number and dense distribution of 1.36 µm particles attached to a single cell, manual counting became impractical and inaccurate. Therefore, a Machine learning model was developed as an automation tool to assist in area calculations. Specifically, image thresholding based on pixel intensity differences was applied to create a binary mask, which removed the background and cell structure, leaving only the image region corresponding to the magnetic particles for analysis. The area of the region of interest was then determined using the analyzed particle function. Image size synchronization was also performed to ensure that area measurements were accurate and comparable between samples.

Results of magnetic beads-cells binding evaluation using Machine learning

The average accuracy of both the Object Detection and Segmentation models for both types of beads is high, demonstrating the effectiveness of the models when applied to cells and beads. With the input image size after detection normalized to 640×640 pixels, the YOLOv8 segmentation model performed well with a mAP@0.5 of 99.5% for both classes. Segmentation results for the two object types are presented with annotations indicating

the corresponding class for each color: pink pixels represent the Cells class, while red pixels represent the Beads class. Figure 4.12 (A) shows the segmentation image of cancer cells attached to 3.0 µm MBs, and Figure 4.12 (B) shows the segmentation image of cancer cells attached to 4.5 µm MBs. Overall, the segmentation model accurately segments both cells labeled with 3.0 µm MBs and cells labeled with 4.5 µm MBs, without misclassifying beads as cells or missing cells at the image edges.

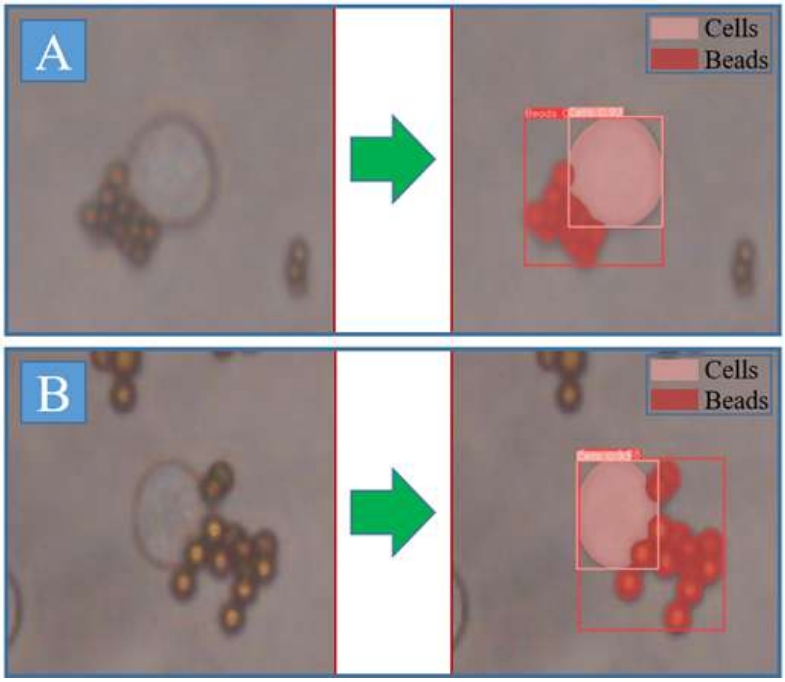

Figure 4.12: Yolov8 segmentation prediction. (A) Segmentation model with 3.0 µm MB, (B) Segmentation model with 4.5 µm MB.

The dataset prepared for training included 146 images of 4.5 µm Cell-Beads and 155 images of 3.0 µm Cell-Beads, captured using a microscope with a resolution of 1280×1280 pixels (Table 4.1). These images were manually labeled and underwent multiple data augmentation techniques before being fed into the YOLOv8 object detection model. After labeling, the total number of cells in the 4.5 µm Cell-Beads dataset was 1,885 and in the 3.0 µm Cell-Beads dataset was 2,197. Each image could contain a minimum of 2 cells and a maximum of 30 cells.

Table 4.1: Statistics on the amount of raw data collected

Sample Type	Number of images	Total number of cells
Cells - particles from 4.5 µm	146	1,885
Cells - particles from 3.0 µm	155	2,197

To evaluate the algorithm's performance, two metrics—Intersection over Union (IoU)

and mean Average Precision (mAP)—are used. The IoU metric measures the degree of overlap between the bounding box predicted by the model and the bounding box of the ground truth data, while mAP evaluates the overall accuracy of the model by estimating the area under the precision–recall curve. Based on the IoU metric, it is possible to determine the degree of similarity between two objects—the actual location of the object and the location predicted by the model—thereby selecting a threshold to decide whether a bounding box is accurate or not, while also determining the values of TP (True Positive), FP (False Positive), FN (False Negative), and TN (True Negative) values in the model's classification matrix. The Precision value is then calculated as TP/(TP+FP), and the Recall value is calculated as TP/(TP+FN).

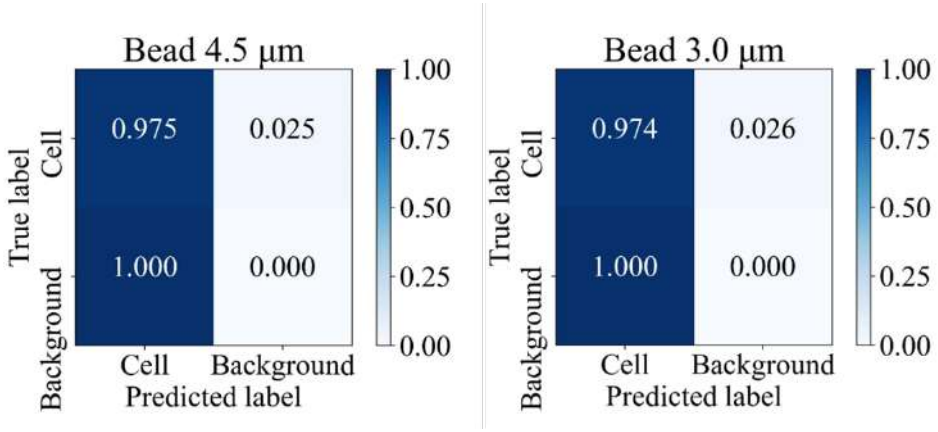

Figure 4.13: The confusion matrix of the Object Detection model for the two particle types shows excellent model performance. For the 4.5 µm particle, the model achieves a True Positive (TP) rate of 0.975, a False Positive (FP) rate of 0.025, and a True Negative (TN) rate of 1. For the 3.0 µm particles, the model achieved a True Positive (TP) rate of 0.974, a False Positive (FP) rate of 0.026, and a True Negative (TN) rate of 1. These results show that both models work effectively in accurately identifying cases with cells and do not miss any cell objects.

Since the coverage of cells by the two types of microparticles of different sizes is relatively similar, the two cell detection models—one for 3.0 µm MBs and one for 4.5 µm MBs—show nearly equivalent accuracy. However, the error matrix of the detection model for cells with 4.5 µm MBs shows slightly higher accuracy. This difference stems from the fact that 4.5 µm MBs are larger and, when attached to cells, cause less interference and cover the cell edges less than the 3.0 µm type. Therefore, the model for 4.5 µm MBs yields a slightly more accurate confusion matrix (Figure 4.13). Detailed information on mAP, Precision, and Recall for both MB types is presented in Table 4.2.

Table 4.2: Performance statistics table

Model	Precision	Recall	mAP@0.5
Object detection – 3.0 µm MBs	0.96	0.978	0.987
Object detection – 4.5 µm MBs	0.932	0.964	0.985
Segmentation – 3.0 µm MBs	0.981	0.936	0.98
Segmentation – 4.5 µm MBs	0.981	0.992	0.995

Table 4.2 details the highest average accuracy along with the precision and recall metrics of the model. For the Segmentation task, the model's performance when processing 4.5 µm MBs is higher than that of 3.0 µm MBs. The size ratio between beads and cancer cells plays an important role in adjusting the resolution for both cells and beads. Therefore, the edges of 4.5 µm MBs, which are closer in size to cells, become sharper, leading to higher accuracy of the segmentation model for cells attached to 4.5 µm MBs.

Coverage performance is illustrated through statistical plots in Figure 4.14. The x-axis represents coverage area in pixels, ranging from 0 to 150,000 pixels, while the y-axis represents the corresponding number of cells covered by MBs. The plots show the distribution of coverage results along the x-axis. The appearance of average values in certain regions indicates a trend toward concentration, but the large standard deviation reflects significant variability in the data. This observation shows that the degree of MBs binding varies markedly between cells: some cells bind few MBs, while others bind larger quantities. 4.16 C provides a visual comparison between the two types of MBs, showing their concentration levels and coverage efficiency. It should be noted that factors such as the aptamer density on the MBs and the surface properties of both the MBs and the cells can influence their interactions. However, an important factor explaining the difference in binding ability between beads of different sizes is the surface-area-to-volume ratio (SA/V). Since MBs are spherical particles, their SA/V is inversely proportional to their radius. Theoretically, smaller beads will have a higher SA/V value, meaning more binding sites on cell surface receptors. Therefore, small beads typically exhibit higher binding efficiency than large beads, which is consistent with the results obtained in the study.

Magnetic separation results in microfluidic channel structures

To investigate the actual capture efficiency of cell-magnetic particle complexes, a separation experiment was conducted. A mixture of target cells A549 (labeled with magnetic particles and stained green with calcein green AM) and reference cells MRC-5 (unlabeled, stained red) was introduced into the microchannel system. The experimental results are presented in Figure 4.15. The green fluorescent signal in the trapping cavities confirms

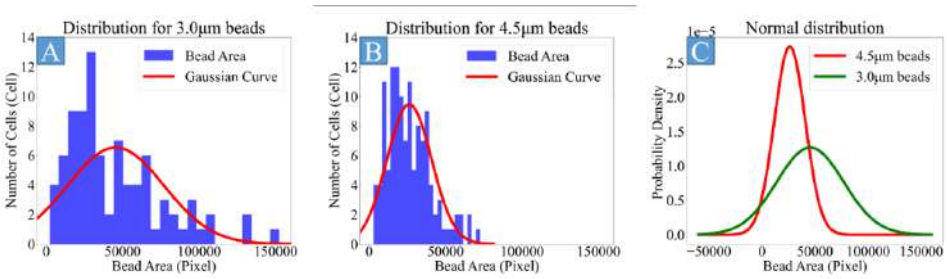

Figure 4.14: The binding efficiency of MBs during A549 cell recognition, represented as statistical graphs through the distribution of percentage coverage area values. (A) Distribution of the area of 3.0 µm MBs adhering to each cell. (B) Distribution of the area of 4.5 µm MBs adhering to each cell. (C) Gaussian curve illustrating the probability distribution of MBs in both cases.

the successful capture of A549 cells. These cells were mainly retained in the first trapping cavities and gradually decreased in number in the subsequent cavities. This is a typical kinetic model, consistent with the sequential filling mechanism: the trapping sites with the highest affinity (where the magnetic field gradient is strongest) will be filled first, and the cells arriving later will be captured at the subsequent sites. The specificity of the aptamer–cell binding process is confirmed by the absence of MRC-5 cells (red dots) in the capture region, demonstrating that magnetic force is the dominant mechanism governing this process.

A notable counterintuitive observation is that the total number of cells trapped is higher when using smaller magnetic particles, which seems to contradict simulation results (which typically predict stronger magnetic forces for larger particles). However, this contradiction is convincingly explained by the deposition of large complexes at the inlet of the microchannel. Due to the significant size difference between the sample tube and the microfluidic channel, a dead volume is formed, creating resistance and vortex flow. In this region of low flow velocity, the balance of forces is altered. Gravitational force, which is proportional to the mass (and thus size) of the complex, becomes dominant over the drag force of the flow. As a result, larger (and thus heavier) cell–MB complexes settle and accumulate at the inlet, unable to enter the separation zone efficiently.

To provide a more comprehensive and accurate view, capture efficiency is broken down into three indices: overall capture, accumulation rate at the inlet, and effective capture. This approach allows for the isolation and quantification of different factors affecting the final result. The results show that as particle size increases, overall capture efficiency decreases (73.4% for 1.36 µm particles, 60.1% for 3.00 µm particles, and 50.5% for 4.50 µm particles). This trend is due to a sharp increase in the accumulation rate at the inlet (5.4%, 26.7%, and 42.9%, respectively). Conversely, the effective capture efficiency—an index reflecting the actual capture capability within the channel—increased gradually with particle size (77.6%, 82.0%, and 88.4%, respectively), fully consistent with the prediction

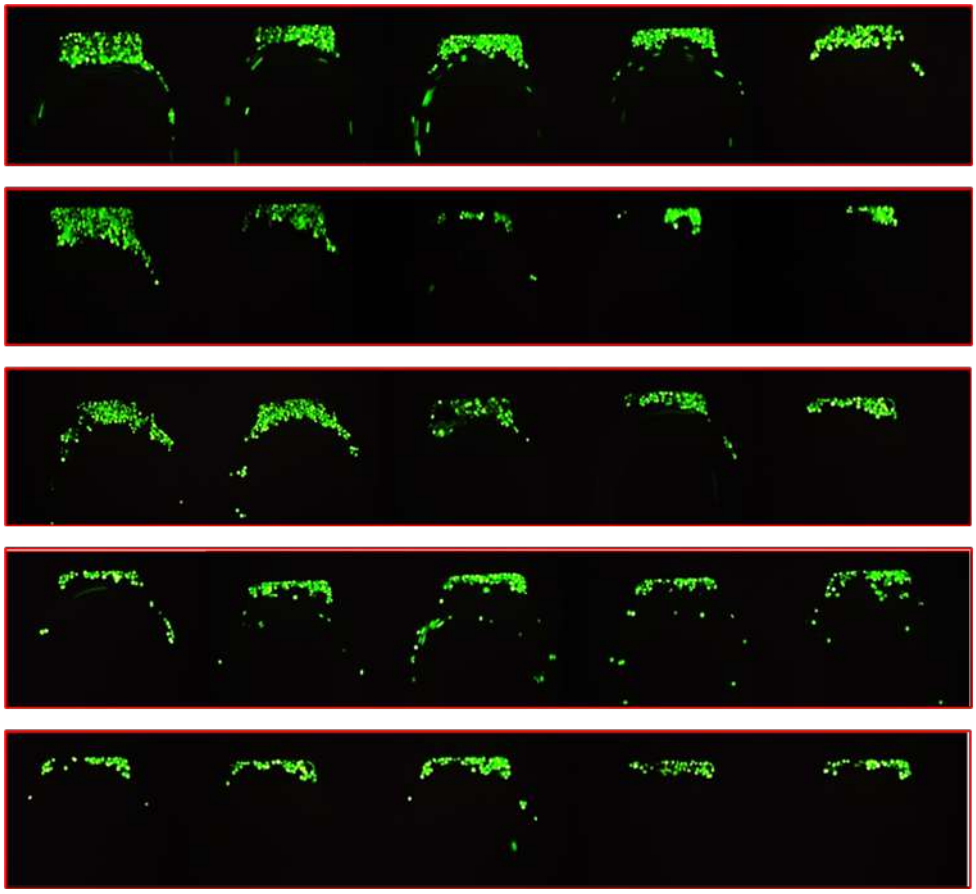

Figure 4.15: Results of A549 cells (stained green) being captured in the microfluidic channel.

of stronger magnetic forces on larger particles. This analysis emphasizes that ignoring hydrodynamic factors at the inlet can lead to misleading conclusions.

To assess purity, another experiment was conducted with a mixture of A549 and HeLa cells. Results in Table 4.3 show that the average purity across all 10 channel cycles reached approximately 99.1%. This extremely high purity has significant practical implications, particularly in diagnostic applications requiring nearly contamination-free samples, such as genetic analysis or proteomics of circulating tumor cells (CTCs). Further experiments investigated the effect of magnetic particle concentration (corresponding to particle solution volumes of 3 µl, 5 µl, and 10 µl). The results revealed a delicate trade-off: too few magnetic particles (3 µl) led to low efficiency due to insufficient binding, while too many particles (10 µl) could cause free magnetic particle accumulation, saturating the initial trap sites and potentially reducing efficiency over time. These results emphasize that optimizing both magnetic particle concentration and microchannel geometry design is crucial for achieving the highest separation efficiency.

Table 4.3: Cell coverage in the microchannel and purity of the filtration system

Channel loop	**A549 coverage (Pixel)**	**Hela coverage (Pixel)**	**Purity (%)**
1	32320	569	98.27
2	16,685	135	99.2
3	61,519	1359	97.84
4	63,515	375	99.41
5	38,157	64	99.83
6	53,370	148	99.72
7	63,300	939	98.54
8	43,565	171	99.61
9	56,071	788	98.61
10	54,494	55	99.90

On average across all 10 channels, the system achieved a purity of approximately 99.1%. This indicates that the system is capable of removing nearly all non-magnetically labeled HeLa cells while effectively retaining the target A549 population. The stability of the results across multiple channels demonstrates the repeatability and reliability of the method. Thus, by fluorescent staining and quantitative analysis using ImageJ, it can be confirmed that the capture process occurs almost exclusively for A549 cells that have attached magnetic particles. This retention mechanism is entirely due to the magnetic force of the external magnet acting on the magnetic particles attached to the cells, rather than random interactions or mechanical adhesion within the microchannel.

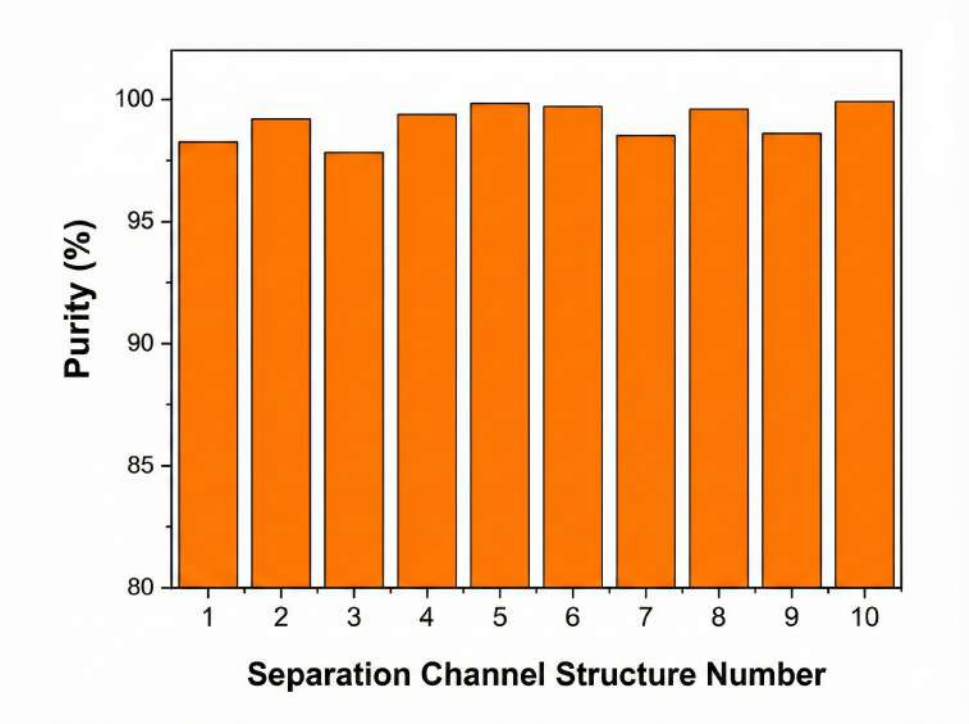

Figure 4.16: Purity distribution at the channel loops.

The performance of the small structures inside the microchannel was also evaluated over time using UV imaging quantification. UV images of 10 structures were captured after the solution entered the channel for 45 minutes. The separation efficiency of each structure in order from one to ten was recorded and shown in Figure 4.16. The results showed that after 45 minutes, the fourth channel structure had the highest separation efficiency across the entire microchannel with a value above 6%. This is explained by the fact that A549 cells and free magnetic particles retained in the first three channel structures completely filled the space in the microchannel, and subsequent cells were retained in the subsequent channel structures. Consequently, the separation efficiency of channel structures 4 to 6 was higher than that of the first three channels. Concurrently, the free magnetic particles retained in the first three channels caused the separation efficiency of the channel to decrease significantly compared to the first 15 minutes, with the separation efficiency of the first three channel structures at approximately 5% and at 45 minutes, the efficiency was approximately 4%. In the rear channel structures, the separation efficiency remained stable at around 4%, except for channel 9 at 4.8%.

The research team continued to investigate the separation efficiency of solutions containing A549 cells bound to different amounts of magnetic particle solution. A549 cells were bound to 5 µl of magnetic particle solution and 3 µl of magnetic particle solution to investigate the effect of the number of magnetic particles in the solution on the separation efficiency in each microchannel structure. The results of the magnetic separation experiment after 45 minutes are shown in Figure 4.17. The separation efficiency of the

A549 cell sample bound with 5 µl of magnetic particle solution was superior to that of the sample using 3 µl.

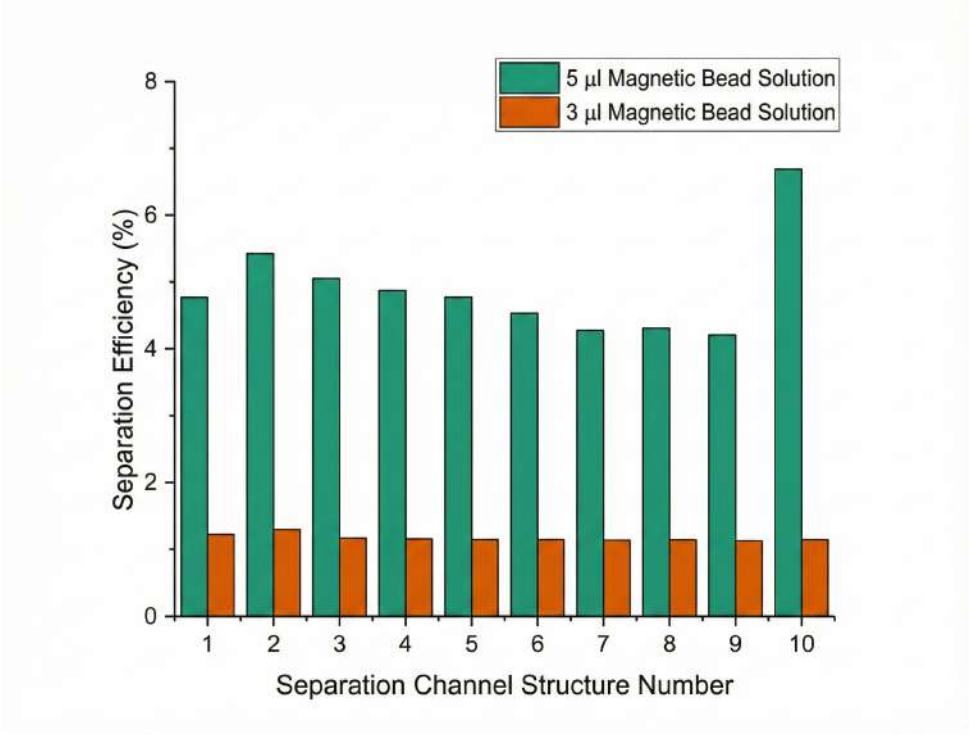

Figure 4.17: Magnetic separation results at the small separation channel structures of the two samples using 5 µl and 3 µl of magnetic particle solution.

The separation efficiency of the sample using 3 µl of magnetic particle solution was very low across all 10 channel structures. This result indicates that the ability to attach magnetic particles to A549 cells is ineffective when using a small amount of magnetic particle solution, as only a small number of cells are retained by the magnetic force of the magnet. In contrast, the sample using 5 µl of magnetic particle solution showed significantly higher separation efficiency, with separation efficiency exceeding 4% across all 10 channel structures, particularly in the final channel structure, where separation efficiency reached nearly 7%. The first channel structures had a higher average efficiency than the other channels in this sample, with separation efficiency gradually decreasing down to the ninth channel structure. These results indicate that with a small amount of magnetic particle solution, the channel structure does not affect separation efficiency. In the remaining two solution samples, the first channel structures had the highest filtration efficiency initially and gradually decreased over time due to the accumulation of free magnetic particles inside the microchannels. After 45 minutes, the efficiency of the subsequent channel structures gradually increased because cells not retained in the first channel structures were retained in the subsequent structures of the microchannels. The sample solution using 5 µl of magnetic particle solution was more effective because it had fewer free magnetic particles than the sample using 10 µl. It can be seen that the separation efficiency in the

first channel structures is higher than in the channels in the latter half, except for the last channel. The results confirm that the volume of the magnetic particle solution is a determining factor in the efficiency of cell separation in the microfluidic system. Furthermore, microfluidic channel structures play a role in coordinating flow and cell retention regions, where the rational distribution of separation channels can contribute to optimizing the overall performance of the system. These results lay the foundation for optimizing the amount of magnetic particles used and channel geometry design to improve the accuracy and efficiency of separation systems in biological and precision medicine applications.

4.3.2 Cell encapsulation in droplets and cell counting results

Cell encapsulation results in droplets

Figure 4.18 shows the droplet formation process, indicating that droplets were successfully formed according to the Reynolds number. By using droplet displacement to track droplets in consecutive frames, the results show that the pumping speed of the two variable channels affects the droplet velocity in the output channel. Simultaneously, particle size and packing ability also change. Here, droplet velocity is converted to pixels/s, and droplet size is calculated based on the perimeter of the droplet boundary, which is the total distance between the pixels forming the boundary.

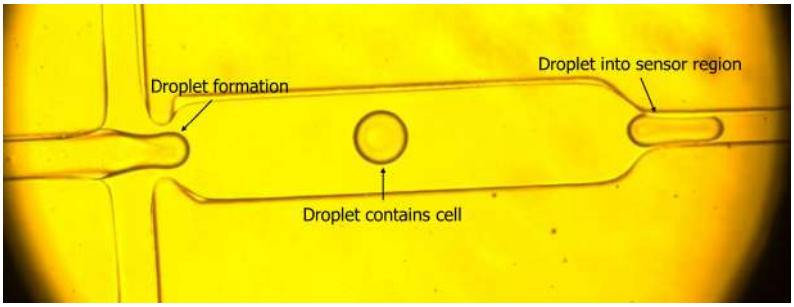

Figure 4.18: Results of droplet formation by the T-channel.

Figure 4.19 Statistics of 10 droplets tracked during the oil channel pumping speed change. For each tracked droplet, information about its speed and size is recorded. It can be seen that droplet Id10 has the smallest size of approximately 220 pixels and the highest speed of approximately 260 pixels/s. Conversely, droplet Id1 has the largest size at 340 pixels but the smallest speed at approximately 165 pixels/s. In general, as the oil channel speed increases, the speed of the droplets also increases and the droplet size decreases. Additionally, when the velocities of both channels stabilize, the generated droplets also stabilize. This demonstrates that droplet size is flexible according to the pumping speed of both channels and can be fully utilized to achieve the desired size.

Monitoring with more droplets created, Figure 4.20 statistics on the number of cell packed in each droplet. With 35 droplets used for statistics, 12 droplets, accounting for

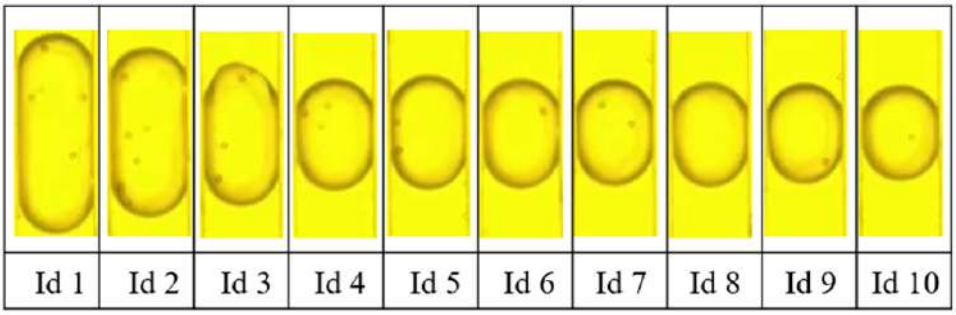

Figure 4.19: The sizes of the microdroplets created.

35%, packed a single cell. Most droplets have a size of 220-250 pixels, equivalent to the droplet size range in droplet sample Id6 to droplet sample Id10. This is the basis for later creating droplets with the highest probability of packaging a single cell.

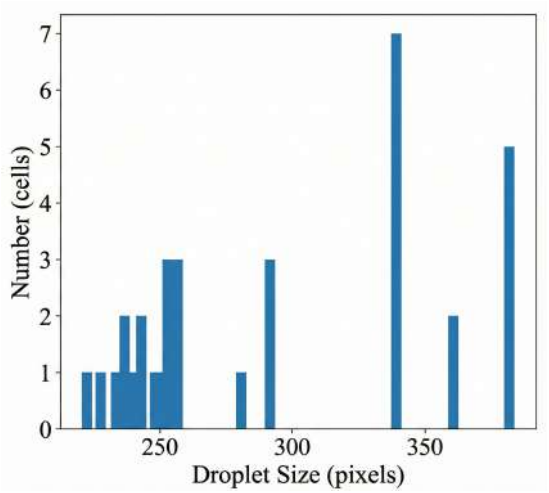

Figure 4.20: Statistics on the number of cells packed with different droplet sizes.

Results of the machine learning model for cell counting in droplets

After creating droplets for cell encapsulation and adjusting their size, the detection model was applied to the obtained dataset. In Figure 4.21, it can be seen that the model's detection accuracy is quite high, allowing a confidence threshold of up to 80% to be set to eliminate false positives.

Based on the IoU (Intersection over Union) metric, which calculates the consistency between two objects—the actual location of the object and the predicted location—a threshold is selected to determine whether a given location accurately represents the object. The metrics TP (True Positive), FP (False Positive), and FN (False Negative) are defined. TP refers to cases where the predicted class and location match the actual label and actual location. FP relates to the false alarm rate, meaning cases where the object's location is incorrectly detected or the location is correct but the class is misclassified. This

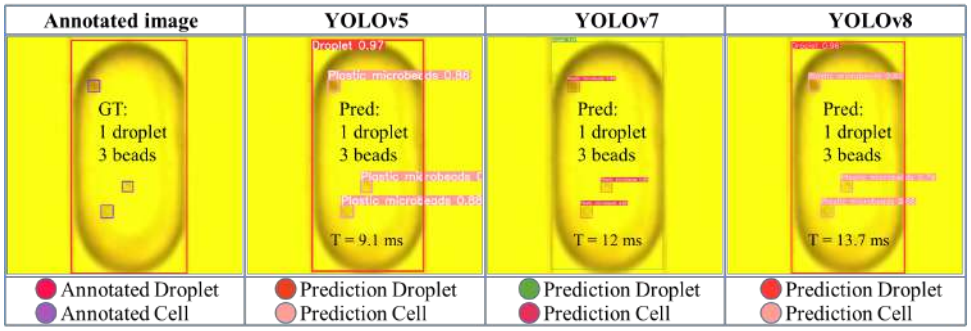

Figure 4.21: Object detection results on several samples.

can be easily observed in cases where objects are detected where there is nothing or where the class is misclassified. FN relates to the false negative rate, meaning positions where objects exist but are not predicted. For object detection problems, TN is not evaluated because this value is not meaningful in the assessment; it represents the number of cases where nothing exists and the model does not predict anything. From these parameters, we can establish the system's error matrix as follows (Figure 4.22): .

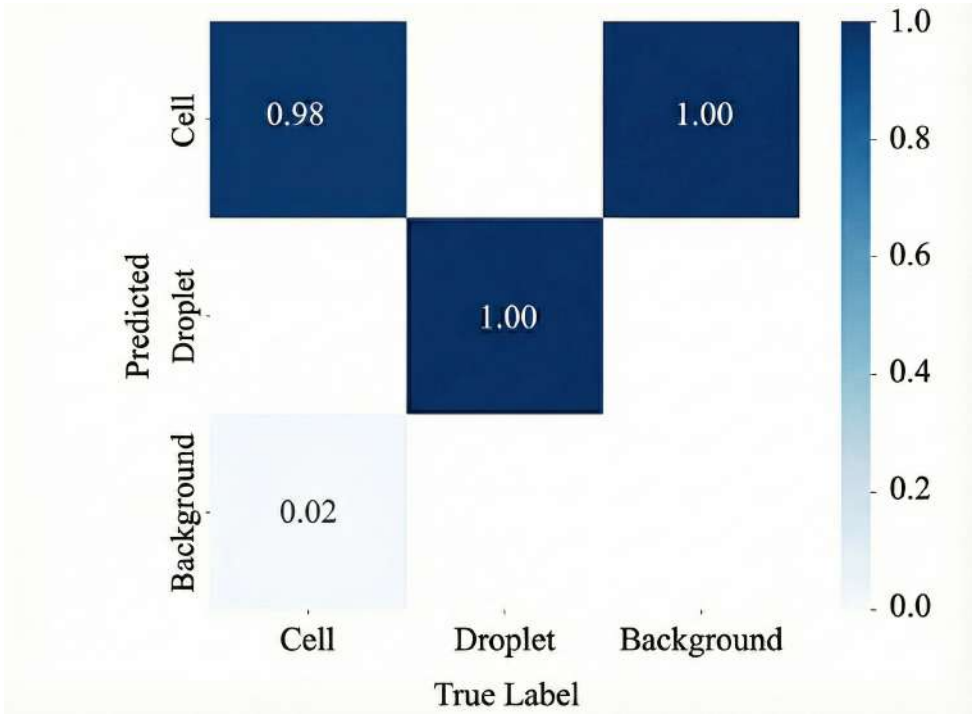

Figure 4.22: Confusion matrix for object detection.

The matrix has been normalized over the total number of tested objects. The number of tested objects for the droplet and particle classes is 500 and 600, respectively. The model has only two classes, but the diagram includes an additional background object to represent the FN parameter, which represents missed cases and is considered background. Looking at the main diagonal, the TP parameter of the two objects is very high with a detection accuracy rate of 100% for droplets. In addition, the accurate detection rate

of particles is 98%, in which 2% of particles are missed. These are cases that cause confusion when labeling because there is no clarity between having particles and not having particles. The 100% value at positions 1 and 3 of the matrix indicates that 100% of the mispredictions are mistaking particles for background, meaning cases where a region of space is predicted to be a particle but nothing is present. Overall, the error matrix shows that the model's ability to detect objects with the two defined classes is quite good.

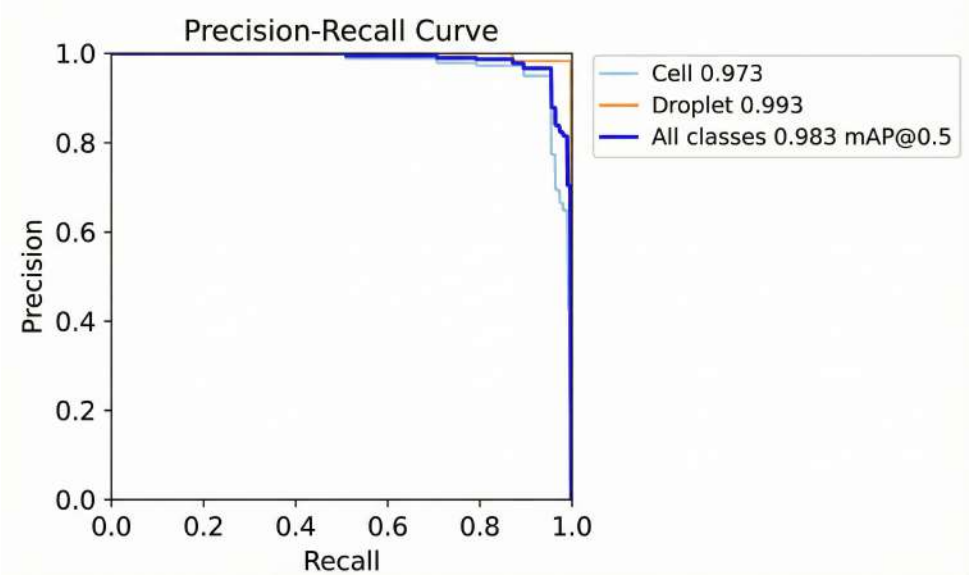

Figure 4.23: Precision-Recall curve of the YOLO model.

In the figure 4.23 shows the classification performance of the model at different thresholds through two parameters: Precision and Recall, which are linked by different threshold values.

$$precision = \frac{TP}{TP + FP} \tag{4.4}$$

$$recall = \frac{TP}{TP + FN} \tag{4.5}$$

Precision is a value related to accuracy based on the model's predictions, and Recall is accuracy based on the actual labels assigned initially. The sum of TP and FP is the number of predictions the model makes for all samples submitted for testing. The sum of TP and FN is the number of objects that actually exist in the test sample based on labeling. Typically, we want both of these values to be high, but they are constrained by the IoU (Intersection of Union) threshold parameter. If this value is high, the detected regions must almost completely match the true label region of the object to be considered a correct prediction of the location. This results in very few false detections, but sometimes it discards parts that actually contain objects because the prediction confidence is not high enough. Conversely, when this value is low, even a region with low confidence is

considered to contain a real object, leading to many predictions and consequently many false positives. Thus, the Precision and Recall curves help us choose an appropriate threshold to balance both the accuracy of false positives and the false negative rate. The threshold value decreases as Recall increases from 1 to 0. In the diagram Figure 4.23 shows that the classification performance of both object classes is very good, with an average value of 98.3% at the threshold of 0.5. This is an acceptable value and can be used in practice. The particle object studied has Precision and Recall values of 97.5% and 93.5%, respectively, at the 0.5 threshold. This value indicates excellent particle object classification capability.

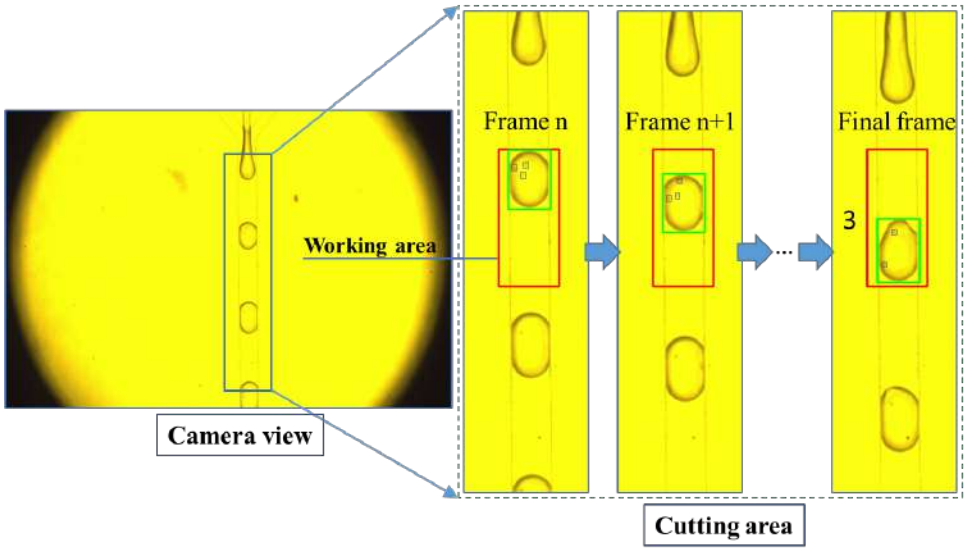

Figure 4.24: Some results of counting the number of particles in a droplet.

The final goal of droplet detection is to count how many particles are in the droplet. In Figure 4.24, several results extracted from a 40-second test video demonstrate the model's excellent particle counting capability. The predicted particle count is for the droplet that just passed through the working area. The system demonstrates real-time capability with an average processing time of 35ms per frame. Based on statistics from 80 droplets appearing in the video, there were 3 miscounted droplets. These cases involved particles being hidden within the inner wall of the throughout the droplet's passage through the working position, the droplet's appearance time in the working area being too brief, etc. Thus, it can be concluded that the accuracy of particle counting reaches 96.25%.

However, despite the high accuracy achieved, relying on image-based analysis for cell enumeration within droplets presents inherent limitations regarding system throughput. The requirement for high-speed video recording, coupled with the computational load of real-time algorithmic processing (35 ms per frame), creates a bottleneck that restricts the maximum flow rate the system can handle effectively. Furthermore, optical methods remain susceptible to errors caused by focal plane deviations or visual occlusion. To address

these constraints and facilitate high-throughput analysis, an alternative approach utilizing integrated impedance sensors is proposed. This technique enables the direct detection and counting of cells encapsulated within droplets based on electrical conductivity differences, offering a robust, label-free solution capable of operating at significantly higher speeds without the latency associated with image processing.

4.3.3 Cell counting using impedance sensor results

Cell Detection and Counting

To address the processing speed bottlenecks and throughput constraints associated with image-based analysis, the utilization of integrated impedance sensors is proposed as a robust alternative. This approach allows for the direct and rapid detection of encapsulated cells, independent of camera frame rates. Figure 4.25 illustrates a droplet passing through the impedance sensor region, where the presence of a cell within the droplet alters the local electrical properties, resulting in a measurable change in impedance. As the droplet traverses the sensor area, the system captures these impedance variations, which are then processed to identify and count individual cell events.

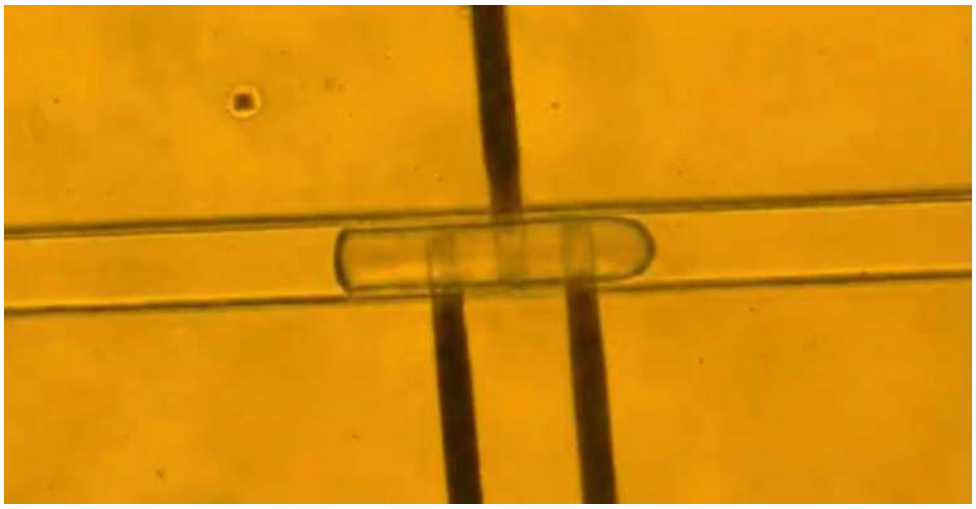

Figure 4.25: Droplet through the impedance sensor region.

To quantify the accuracy of the impedance measurement system, a multi-step data processing and validation procedure is performed, starting with the acquisition of raw signals. As illustrated in Figure 4.26, the physical system consists of electrodes and conductive channels (Figure 4.26.a) that acquire an initial electrical signal (raw data) via a data acquisition (DAQ) system. This signal has an oscillating waveform and contains a lot of noise (Figure 4.26.b). To extract useful information, this raw signal is passed through a band-pass filter. This filtering process removes unwanted carrier frequencies and background noise , retaining only the characteristic spikes caused by cells passing through the sensor region. The result is a clean filtered signal sequence, where each cell

event is represented as a distinct pulse (Figure 4.26.c). For verification and quantification, these pulses are amplified and analyzed in detail (Figure 4.26d). A peak detection algorithm is applied to automatically identify and count the number of these signal pulses, corresponding to the number of cells detected by the electronic system. The accuracy of the system is then quantified by directly comparing this electronic count with a "ground truth" standard. This standard is established by analyzing video segments recorded from the microscope throughout the experiment, in which cells passing through the detection region (SPOT) are counted manually.

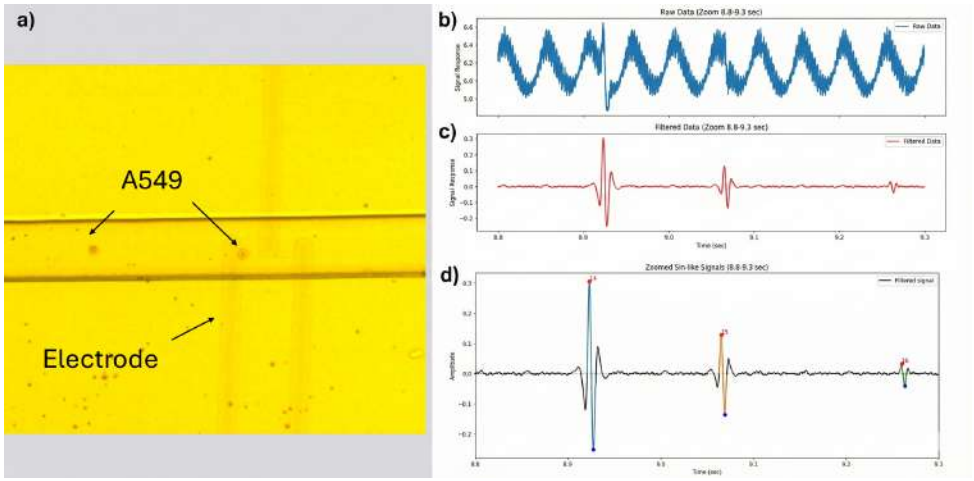

Figure 4.26: (a) Cell counting system comprising electrodes and channel mold. (b) Raw data collected by the DAQ system. (c) Data after bandpass filtering. (d) Filtered data magnified.

In this experiment, the research team used a microchannel with a width of 30 µm and a height of 30 µm to investigate and evaluate the cell counting capability of the integrated circuit. A549 cell lines were passed through the microchannel, and the electronic signals obtained from the circuit were processed using a digital filter and a peak detection algorithm. The automatic counting results from the circuit were then compared with the number of cells counted manually from the video recording of the sample pumping process. The objective of the survey was to determine the degree of discrepancy between the number of cells counted by the circuit and the actual data, thereby evaluating the accuracy and reliability of the system. After the A549 cells pass through the detection region in the microchannel, the electronic signal is received in the form of short-term oscillations with a distinct amplitude change from the baseline. Essentially, as the cells pass through, changes in the dielectric constant and impedance in the microchannel alter the signal current, creating a characteristic electrical pulse. However, the raw signal simultaneously contains many noise components, including thermal noise from the components, noise from the external environment, and background oscillations due to the buffer solution. For accurate processing and analysis, the raw signal is passed through a high-order Butterworth digital filter. This filter is capable of removing high-frequency

noise while preserving the characteristic waveform of the cell passage event. After filtering, the signal becomes "cleaner," clearly showing the peaks or troughs associated with each cell event. Figure 4.27 shows a magnified section of the signal between 10 and 10.4 seconds. A prominent electrical pulse with a large amplitude, exceeding the set detection threshold, can be observed, indicating a cell passing through the microchannel.

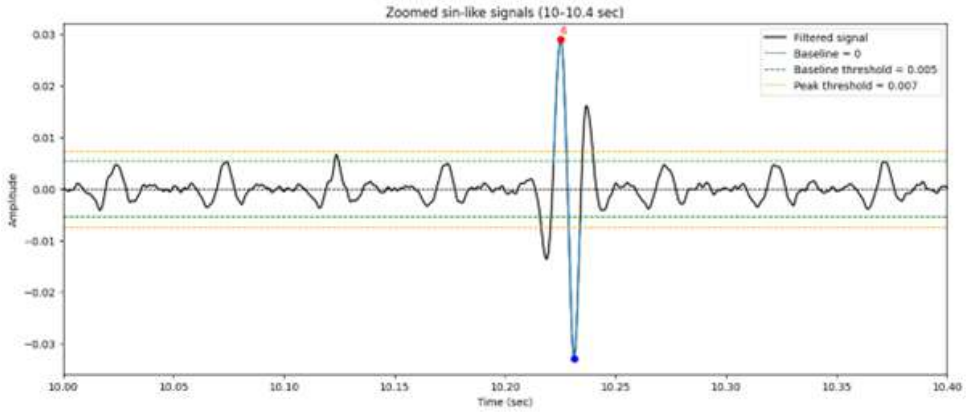

Figure 4.27: Cell signal shape after filtering.

To assess the duration of an event, the research team analyzed the peak width at half maximum amplitude (full width at half maximum – FWHM). Quantitative analysis showed that the average amplitude of the acquired pulses was 0.0296, significantly higher than the background fluctuation (~0.01), thereby achieving a sufficiently high signal-to-noise ratio (SNR) for the circuit to clearly distinguish real events from noise. At the same time, the average duration of an event (calculated as the pulse width at half maximum amplitude – FWHM) is 0.009912 seconds. This means that the system is capable of detecting and processing approximately 1 / 0.009912 ≈ 101 events/second, corresponding to more than 6000 cells per minute under stable operating conditions.

Notably, determining event timing not only quantifies counting speed but also provides indirect information about flow velocity and cell interaction with the microfluidic channel. Small differences in pulse width may reflect changes in cell size or mechanical properties, suggesting the system's potential for not only counting but also analyzing cell characteristics. Detailed analysis of the waveform at the single-event level shows that the integrated circuit not only has high sensitivity and accuracy in detecting cells, but also possesses real-time response capabilities sufficient to process continuous cell flow at high speeds. This is an important basis for proving the system's applicability in biological research and diagnostics.

To investigate the system's accuracy, the research team conducted surveys under various conditions when running A549 cells in microchannels, specifically as follows:

Study 1 – PBS 1x, 5 V, 300 kHz

In the first survey, signals were recorded under conditions of 1x PBS buffer solution, 5 V stimulation voltage, and 300 kHz frequency. Raw data was processed using a digital

filter (Butterworth band-pass filter) to remove background noise and retain the signal band containing information specific to the passing cells.

Figure 4.28 shows the signal after digital filtering, where the x-axis represents time (s) and the y-axis represents signal amplitude. The blue line represents the filtered signal, the yellow dashed line represents the baseline, and the two horizontal orange and green lines correspond to the threshold values (baseline threshold and peak threshold). Signal peaks exceeding the threshold are marked with red dots and numbered sequentially for tracking.

The results show that the system detected 30 signal peaks (corresponding to 30 cell passage events). When compared with the manual count from the video, the actual number of cells observed was 32. Thus, the accuracy reached 93.75%.

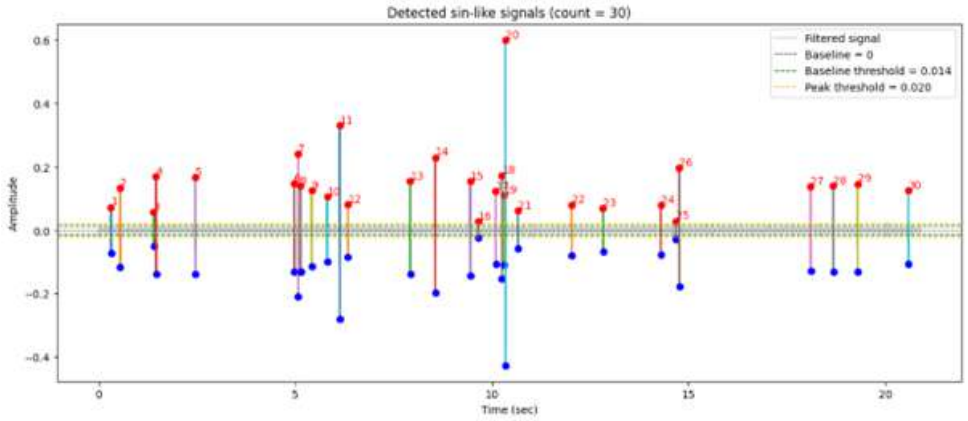

Figure 4.28: Butterworth-filtered signal of A549 cells in microchannels under 5 V – 300 kHz conditions.

The discrepancy between the results can be explained by several factors:

- Low signal amplitude: Some signals have amplitudes smaller than the fixed threshold, so they are not recorded. This is a common limitation when applying fixed threshold algorithms, especially in cases of uneven signals.
- Local background noise: Observations show that some signal segments have large background fluctuations, reducing the signal-to-noise ratio (SNR). These fluctuations can mask or distort the amplitude of some small pulses, causing the circuit to miss events.
- Manual counting errors: When analyzing video, some cells move quickly or overlap, making it difficult to accurately identify each cell.

Therefore, video results may also contain certain errors, although they are often considered the "reference standard." Overall, the survey results show that the system is capable of counting cells quite accurately. However, the use of a fixed threshold in conditions of clearly varying signals carries the risk of cell omission, especially for weak signals.

Survey 2 – PBS 1x, 3 V, 100 kHz

In the second survey, the stimulation voltage was reduced to 3 V and the frequency was adjusted to a lower range (100 kHz). First, the raw signal was filtered using a Butterworth digital filter to remove noise outside the region of interest. Figure 4.29 shows the processed signal, in which the characteristic oscillations can be clearly observed each time a cell passes through the microchannel. Unlike the previous study, the research team here applied a dynamic threshold setting method: baseline threshold = 1 × standard deviation of the background noise level, peak threshold = 1.2 × noise level. This allows the threshold to adaptively change according to the signal noise level, rather than being fixed.

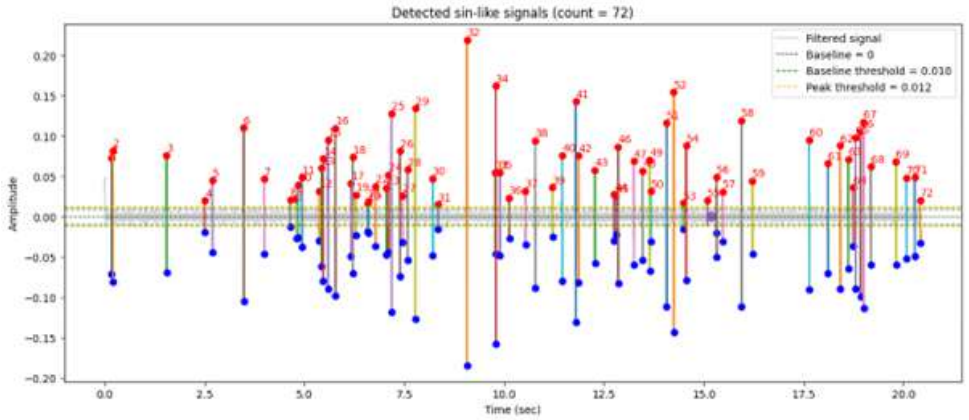

Figure 4.29: Digitally filtered (Butterworth) signal of A549 cells in microchannels under 3 V – 100 kHz conditions.

The results show that the system detected 72 cells, while the number of cells counted from the video was 76 cells, achieving an accuracy of 94.7%. The signal peaks in Figure 4.29 are fairly evenly distributed, with clear amplitudes and fewer omissions compared to Figure 4.28. It can be seen that the dynamic threshold helps identify even low-amplitude signals, which might be omitted when applying a fixed threshold.

The remaining discrepancy (4 cells) may be due to:

- Signal overlap: When two cells pass through the microchannel nearly simultaneously, the recorded signal may appear as a single peak.
- Very low amplitude: Even with a dynamic threshold, some pulses are too small to exceed the detection threshold.
- Cell velocity variation: When cells move quickly, the signal duration is short, leading to reduced pulse amplitude and increased likelihood of being missed.

The survey results confirm that the integrated circuit system is capable of counting A549 cells with high accuracy under experimental conditions. Further optimization of

stimulation parameters (amplitude, frequency) combined with improvements to the peak detection algorithm promises to further enhance the accuracy and reliability of the system in practical applications.

Machine learning model for impedance signal results

Four standard metrics were used to evaluate the performance of the machine learning models used in this study: Accuracy, Precision, Recall, and F1-score. These metrics comprehensively evaluate each model's ability to distinguish between real cell signals and noise. Accuracy measures the overall correctness of the model and is defined as:

$$Accuracy = \frac{TP + TN}{TP + TN + FP + FN} \tag{4.6}$$

where TP is True Positive, TN is True Negative, FP is False Positive, and FN is False Negative. Precision reflects the proportion of positive cases that are correctly predicted, indicating the model's reliability:

$$Precision = \frac{TP}{TP + FP} \tag{4.7}$$

Recall (or Sensitivity) measures the model's ability to accurately identify all relevant cases of the positive class:

$$Recall = \frac{TP}{TP + FN} \tag{4.8}$$

The F1-Score is the harmonic mean of Precision and Recall, providing a balanced metric when dealing with imbalanced datasets:

$$F1\text{-}Score = 2 \times \frac{Precision \times Recall}{Precision + Recall} \tag{4.9}$$

By applying these metrics, the study ensures a thorough evaluation of the performance of machine learning models on both one-class and two-class classification approaches. Accuracy highlights overall correctness, while Precision and Recall provide detailed information about false positives and false negatives, respectively. The F1-Score is a balanced metric, particularly valuable for imbalanced datasets like the one used in this study.

Data collection and segmentation model performance

The dataset used in this study comprises over 1,000,000 data points collected from experimental records, segmented into a total of 1,473 labeled instances for training and testing purposes. To rigorously evaluate the performance and generalizability of the machine learning models, a stratified 5- -fold cross-validation technique was used. Specifically, the dataset was divided into five equal-sized subsets, ensuring balanced representation of cellular and non-cellular signals in each subset. In each iteration, four subsets were used for model training, while the remaining subset served as the validation set, with this

process repeated five times. The final performance metrics, including accuracy, precision, recall, and F1 score, were calculated as the average across these five folds. The statistical significance of the differences between models is assessed using paired t-tests, with a significance threshold set at $p < 0.05$. The segmentation model achieved Precision of 85.33% and Recall of 96.76% on this dataset. The results indicate that the segmentation step effectively collects most cellular signals while minimizing false positives. Further analysis reveals that most cases missed in this stage have minimal peak voltage values around 0.1 V. These findings highlight the model's strong performance while emphasizing the challenge of accurately identifying signals with minimal voltage changes.

Classification model performance

The performance of one-class classification models, presented in Table 4.4, demonstrates that IsolationForest achieves the highest Accuracy of 0.882. However, OneClassSVM outperforms IsolationForest in terms of Precision (0.785) and Recall (0.795), resulting in a higher F1-score of 0.790 compared to 0.720 for IsolationForest. This result suggests that while IsolationForest collects a broader set of cases, it may include more false positives, as indicated by its lower Precision. Conversely, OneClassSVM demonstrates a better balance between accurately identifying cellular signals and minimizing noise, making it more reliable for this dataset. However, the overall performance of the single-class models remains suboptimal, which can be attributed to insufficient convergence of the identified features. The limited distinction between actual cellular signals and noise may hinder the ability of clustering models to classify signals accurately.

Table 4.4: Single-layer model performance

Model	**Accuracy**	**Precision**	**Recall**	**F1-score**
Isolation Forest	0.882	0.715	0.735	0.720
One-Class SVM	0.842	0.785	0.795	0.790

To evaluate the classification machine learning models, the labeled dataset was divided into a training set and a testing set, with the model performance on the testing set summarized through confusion matrices (Figure 4.30). Confusion matrices provide a comprehensive overview of the performance of six machine learning models: Decision Tree, Random Forest, Logistic Regression, SVC, K-Nearest Neighbors Classifier, and Gradient Boosting in a two-class classification task. Ensemble-based methods, such as Random Forest , and Gradient Boosting, along with SVC, demonstrate superior performance with fewer.

Characteristics of the impedance signal generated when a cell moves through the sensor area

Scatter plot in Figure 4.31 illustrates the distribution of two main signal characteris-

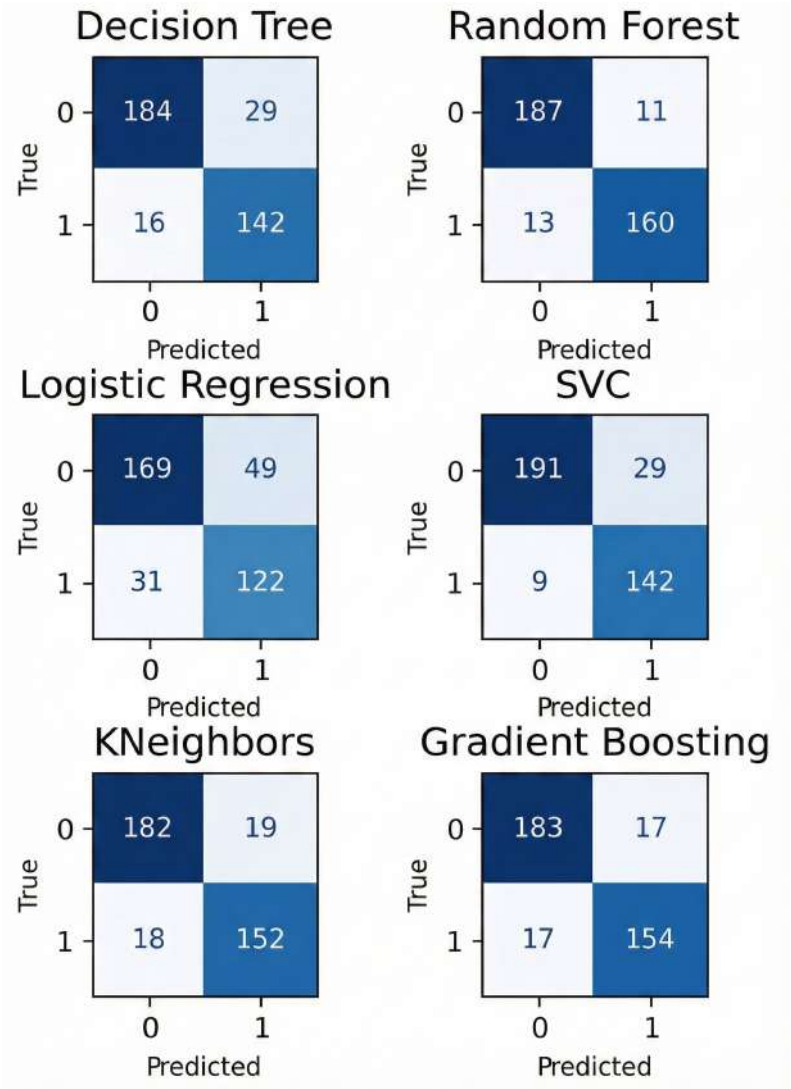

Figure 4.30: Confusion matrix of the 6 classification models.

tics: segment width, representing signal duration, and PP-NP ratio, reflecting the amplitude ratio between positive peaks and negative peaks. These features provide important detailed information about the size and distribution of the cell population within the sample. Most data points are concentrated in regions with average segment width and low PP-NP ratio values, indicating that most cells in the population exhibit similar sizes and relatively balanced signal peaks. However, a subset of data points with higher PP-NP ratios and varying segment widths suggests the presence of larger cells or cells unevenly positioned relative to the electrodes. This distribution highlights the heterogeneity within the cell population and the potential of these features to distinguish unique cells based on their signal characteristics, thereby improving the accuracy of single-cell analysis.

It would be beneficial to consider comparative studies involving deep learning models, such as Convolutional Neural Networks (CNNs) and Long Short-Term Memory networks (LSTMs), for identifying distinct cellular features within the same population. Given the ability of deep learning methods to capture complex, high-dimensional patterns in sequential and spatial data, the use of CNNs or LSTMs may yield improved accuracy and deeper insights into subtle variations between cells that traditional machine learning models may not fully capture. This comparative evaluation can establish additional robust methodologies for single-cell analysis, capable of discovering new biomarkers and improving diagnostic precision in complex biological systems.

The focus of this chapter is the design and development of capacitive sensors capable of direct integration with the liquid-based technology platform. Gold microelectrode structures, chosen for their biocompatibility and excellent conductivity, were fabricated via photolithography and wet etching. For measurement, a custom impedance measurement circuit was designed, capable of analyzing both the real and imaginary components of the total impedance. This system relies on the lock-in detection method to eliminate noise and separate voltage components, ensuring high accuracy even in highly noisy environments.

Theoretically and in simulations, the change in impedance Z was calculated as the A549 cell moved through the sensor region. Simulation results show maximum changes in resistance and impedance of approximately 1,000 kΩ and 325 kΩ, respectively. In cell counting experiments, the system demonstrated real-time response capability, detecting and processing approximately 101 events per second, equivalent to over 6,000 cells per minute. When assessing accuracy, the system achieved 94.7% accuracy under PBS 1x, 3 V, 100 kHz conditions by applying a dynamic thresholding method.

To enhance the reliability of cell signal recognition, machine learning models [83] were applied, using features such as segment width and SP-EP deviation, demonstrating effectiveness in distinguishing cell signals from background noise. Among the one-class classification models, One-Class SVM achieved the highest F1 score of 0.790, demonstrating a good balance between accurately identifying cell signals and minimizing noise.

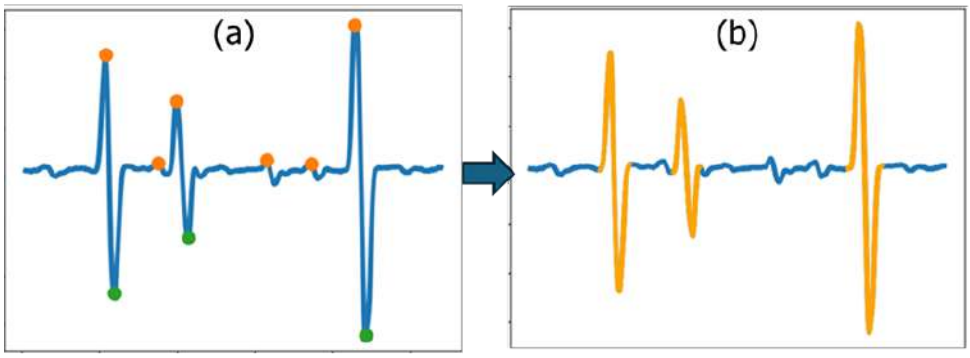

Figure 4.31: The distribution of cell signal segment width and the ratio of positive peaks to negative peaks.

These results highlight the potential utility of integrated impedance sensor technology in applications for accurate cell detection in microfluidic environments.

Performance evaluation of the impedance counter

To evaluate the performance of the impedance counting system in the LoC system, experiments were conducted sequentially with two cell lines, MRC5 and A549, under the same microfluidic channel conditions, flow rates, and environments to ensure objective comparability. The electrical parameters were systematically investigated with voltage amplitudes ranging from 1 to 3 V and frequency ranges of 100, 150, and 200 kHz. The two cell lines differed in morphology and size, making them suitable for verifying the resolution capability of the system.

Table 4.5: Comparison of SNR between A549 and MRC5 under different conditions

Threshold voltage (V)	**Signal-to-noise ratio (SNR) Stimulus frequency (kHz)**					
	100		**150**		**200**	
	A549	MRC5	A549	MRC5	A549	MRC5
1	1.5125	4.9	2.267	5.05	4.375	7.45
2	4.3	4.7375	3.9375	11.11	5	12.75
3	3.7375	10.68	8.575	9.8	7.275	12.34

Performance is evaluated based on two key parameters: signal peak amplitude, reflecting the system's sensitivity in detecting impedance variations as cells pass through the measurement channel, and signal-to-noise ratio (SNR), indicating the stability and reliability of the signal under different operating conditions (Table 4.5). This approach allows simultaneous determination of both cell discrimination capability and output signal

quality, thereby guiding the selection of optimal operating parameters for the impedance counting system.

The average peak amplitude measurement results show that the impedance counting system can clearly distinguish between the two cell lines, MRC5 and A549 (Figure 4.32). At a frequency of 100 kHz and a threshold voltage of 3V, the signal amplitude of A549 reached 0.0299 V while MRC5 reached 0.1495 V, corresponding to an absolute difference of 0.1196 V and an MRC5 signal approximately 5 times higher than A549. When the frequency was increased to 150 kHz, the A549 amplitude reached 0.0343 V and the MRC5 reached 0.196 V, an absolute difference of 0.1617 V with a difference ratio of 5.71 times. At 200 kHz, the amplitude of A549 increased to 0.0585 V while MRC5 reached 0.2468 V, creating an absolute difference of 0.1883 V and a signal ratio of 4.22 times.

These figures show that the system maintains stable discrimination capability across the entire surveyed frequency range, with the MRC5 signal consistently outperforming A549 by 4 to nearly 6 times. In terms of absolute difference, the optimal condition is at 200 kHz ($\Delta V = 0.1883$ V), as the largest signal gap supports more accurate electronic identification. Conversely, when considering the relative ratio, the 150 kHz frequency demonstrates a notable advantage, with the MRC5 signal being 5.71 times higher than A549.

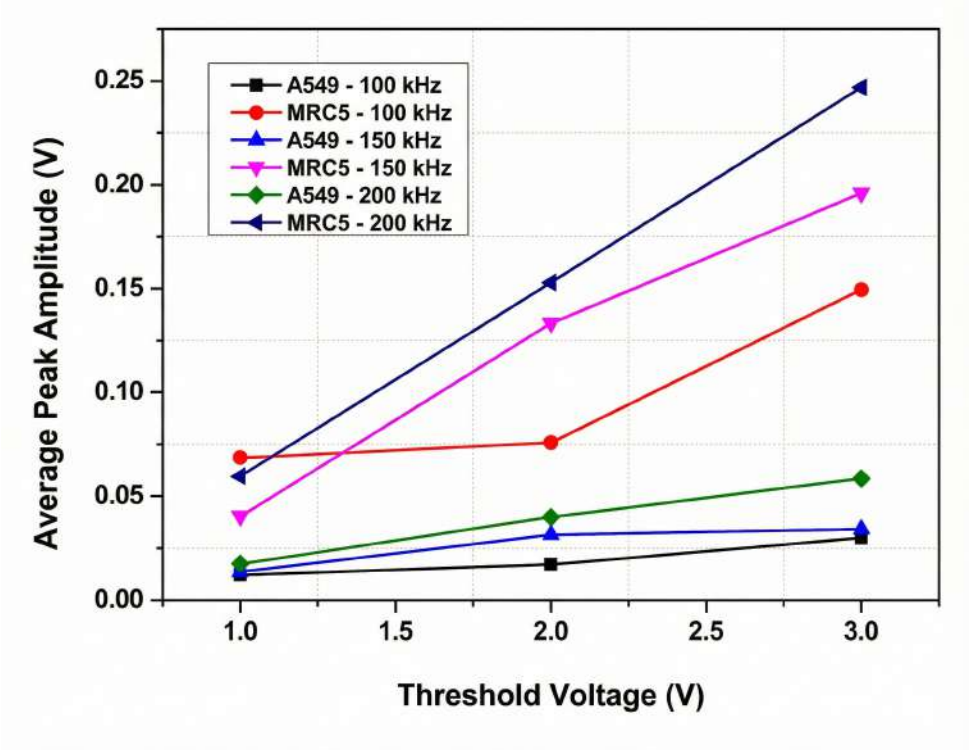

Figure 4.32: Comparison chart of the average peak amplitude of A549 and MRC5.

Overall, the results confirm that the impedance counting system has high performance in distinguishing two cell lines with different morphological characteristics. Specifically,

operation at high frequencies (150–200 kHz) and a threshold voltage of 3 V provides a good balance between sensitivity and resolution, thereby establishing optimal operating conditions for the system.

Table 4.6: Comparison of SNR between A549 and MRC5 under different conditions

Threshold voltage (V)	**Signal-to-noise ratio (SNR) Stimulus frequency (kHz)**					
	100		**150**		**200**	
	A549	MRC5	A549	MRC5	A549	MRC5
1	1.5125	4.9	2.267	5.05	4.375	7.45
2	4.3	4.7375	3.9375	11.11	5	12.75
3	3.7375	10.68	8.575	9.8	7.275	12.34

When evaluating the performance of the impedance counter based on SNR values (Table 4.6), the results show a clear difference between the two cell types, A549 and MRC5. At the voltage thresholds of 1V, all SNR values remain low; however, MRC5 consistently exhibits higher values than A549 at the same frequency. Specifically, at 200 kHz, the SNR of A549 reached about 4.4 while MRC5 reached 7.5, which was the highest pair of values in this cluster. This shows that even at low voltages, the signal from MRC5 still had the ability to maintain better stability than A549.

When the voltage threshold is increased to 2V, the differentiation effect becomes most pronounced. This cluster has the highest SNR values in the entire experiment. At 100 kHz, A549 and MRC5 have relatively similar values (approximately 4.3–4.7), indicating limited differentiation capability. However, at 150 kHz and 200 kHz, the SNR of MRC5 surged, reaching 11.11 and 12.75, while A549 remained significantly lower. Notably, the value of 12.75 at 200 kHz is the highest point in the entire data set, confirming the superiority of MRC5.

At the 3V voltage threshold, the trend remains similar to the 2V group, with MRC5's SNR continuing to outperform A549 at high frequencies. At 100 kHz and 200 kHz, MRC5 achieves 10.68 and 12.34, both significantly higher than A549. An interesting point is that at 150 kHz, the SNR of MRC5 (9.8) is lower than at the 2V threshold, suggesting that increasing the voltage does not always improve signal quality but may be related to saturation or changes in cell impedance characteristics.

The data show that MRC5 consistently achieves higher SNR than A549, particularly evident at frequencies of 150–200 kHz and threshold voltages of 2–3V. These results demonstrate that the impedance counter can effectively distinguish between cell types, with MRC5 producing higher-quality, more easily identifiable signals than A549. This

indicates that the system's performance is not uniform for all cell types but depends on the unique electrophysiological characteristics of each cell line, thereby confirming the applicability of the method for cell classification and identification based on impedance.

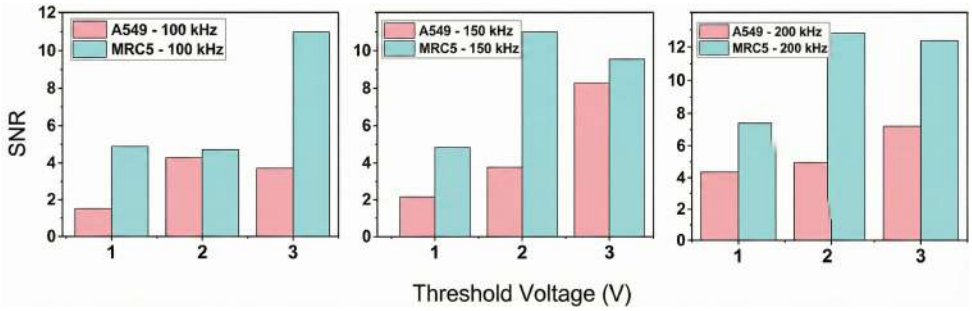

Figure 4.33: SNR values for A549 and MRC5.

This indicates that the performance of the counter is not uniform across cell lines but is closely dependent on electrophysiological characteristics such as size, membrane structure, and intracellular composition. MRC5, with its distinct morphological characteristics, produces a greater change in impedance when passing through the measurement channel, leading to higher signal amplitude and SNR. Conversely, A549 produces a lower signal, reflecting reduced sensitivity during detection (Figure 4.33).

Overall, the data confirms that the microfluidic impedance measurement system is not only capable of detecting stable signals but also demonstrates clear discrimination between the two cell lines. The identification of the optimal range of conditions (2–3V, 150–200 kHz) contributes to reinforcing the practical application of this method in cell biology research and biomedical screening. Notably, the results open prospects for expanding the system to clinical applications such as classifying cancer cells versus normal cells, early detection of cellular abnormalities, or developing rapid point-of-care (PoC) diagnostic devices.

4.3.4 Results of droplet separation using DEP

Results of droplet steering and separation using DEP

Mineral oil and deionized water are used for the continuous phase and dispersed phase, respectively. These solutions are injected into the microchannel inlets via a dual-phase syringe pump (GEMINI 88 Plus, KD Scientific, USA), and the flow rate ratio between the water phase and oil phase is maintained at 1:3 (60 μL·h^{-1} and 180 μL·h^{-1}) to stabilize the droplet size produced. Droplet samples can be collected from two outlets, specifically the 'Waste Outlet' and the 'Collecting Outlet'. In the experiments, a DC voltage generator supplied an electrical signal to four electrodes, with the voltage value varying from 0 to 320 V, to analyze the effect of electrostatic force on the droplets at each voltage level. A high-speed camera with a speed of 7 gigapixels per second (Phantom VEO-710 L-72G-C,

USA) connected to a 10X optical microscope was used to observe and record the results of droplet manipulation. Finally, droplet classification results were tracked using Python-based software programs with the OpenCV 4.8 library, and droplet deformation at each voltage was estimated using ImageJ software.

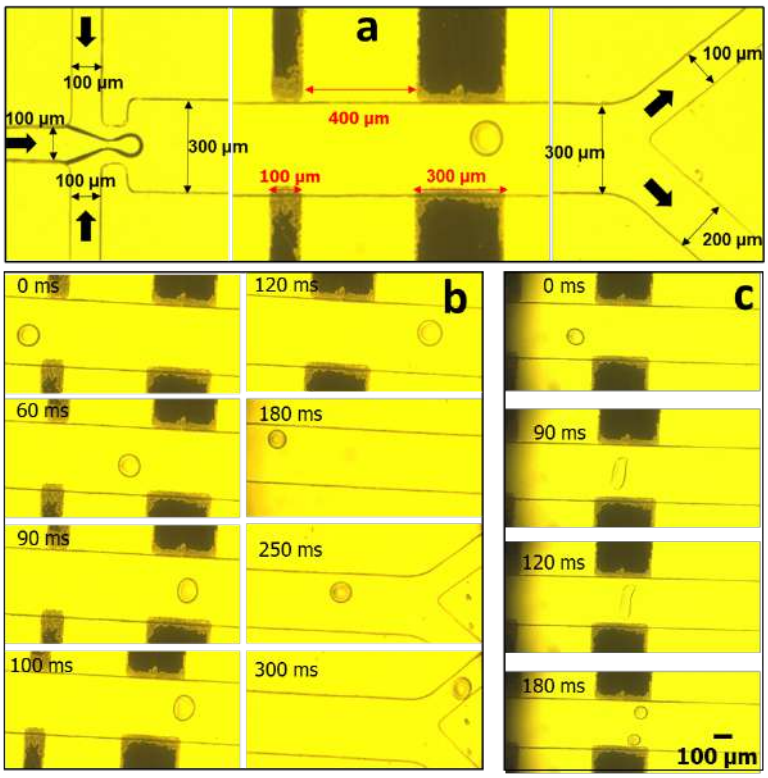

Figure 4.34: The microfluidic chip and gold electrodes were fabricated and experimentally tested using oil and water. a) Actual-size images of the channel and electrodes, b) Time-dependent movement of the droplet as it moves toward the collection channel, and c) Time-dependent movement of the droplet separation phenomenon.

Figure 4.34 shows the fabricated microchannel combined with gold electrodes, where the dimensions of the channel and electrodes were precisely fabricated according to the design model used in the simulation (Figure 4.34 (a)). Droplets, approximately 100 µm in size, are generated within the 300 µm wide main channel, providing sufficient space for the droplets to exhibit sorting or separation effects. Figure 4.34 (b) shows the droplet manipulation phenomenon as the droplet passes through the electrodes and deviates from its initial trajectory toward the collection channel. From 60 ms to 100 ms, the droplet's shape is slightly distorted due to EHD effects, but as it exits the electrode region, the droplet returns to its original spherical shape. As the voltage applied to the electrodes increases, the droplet undergoes significant deformation when passing through the large electrodes, leading to its breakup into two smaller droplets. Detailed experimental parameters and further studies are presented in the subsequent sections.

During the experiment, droplet control phenomena were observed, and the contribu-

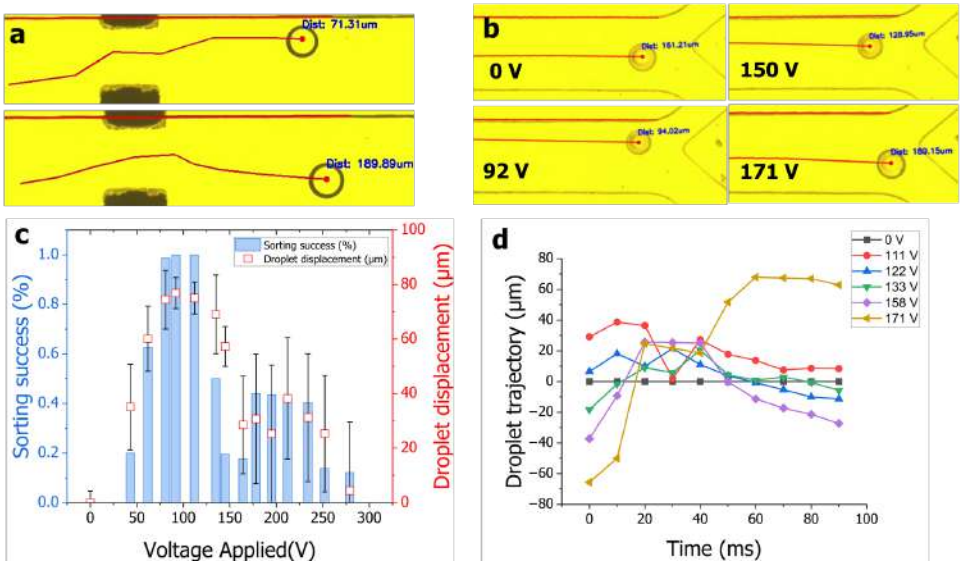

Figure 4.35: Analysis of droplet steering motion in a DC electric field and the effectiveness of droplet classification. (a) Experimental illustration of droplet manipulation in the electrode region. (b) Experimental images showing the displacement of droplets toward the remaining outlet at different DC voltage levels. The label "Dist" denotes the distance between the droplet center and the upper channel wall. (c) The effectiveness of droplet classification into the collection outlet is represented by the classification success rate, defined as the percentage of accurately classified droplets out of the total number of droplets at different voltage levels. Droplet displacement indicates the change in droplet position measured in micrometers (µm) relative to their original path in the absence of a DC electric field. (d) The deflected trajectory of droplets in the electrode region over time, where the droplet trajectory denotes the path of the droplet as it moves through the electric field.

tion of electrostatic forces to the classification mechanism was thoroughly investigated to provide deeper insights. Notably, the electrodynamic force (DEP) acting on polarized droplets was identified as an important factor affecting the efficiency of the classification process. Before entering the electric field region created by the electrodes, the droplet retains its original shape and moves in a straight trajectory at the center of the main channel. However, upon entering the non-uniform electric field region created by the small and large electrodes, the droplet deforms and deviates from its original trajectory. Figure 4.35 (a) shows the altered trajectory of the droplet as it passes through the electric field created by the electrodes. The trajectory is measured and analyzed using ImageJ software, and the results are displayed on the channel image using Python. When no voltage is applied to the electrodes, the deviation of the droplets is minimal, and all droplets are directed into the collection channel. Increasing the voltage, creating a stronger electric field for all electrodes, causes a significant change in the trajectory of the droplets. At different voltage levels, the droplets were driven and guided into the designated collection channel (Figure 4.35 (b)). Using a 300 μm wide channel and droplets with a diameter of 100 μm, the sorting efficiency reached a maximum of 100% at voltages ranging from 92 V to 112 V (Figure 4.35 (c)). At 92 V, the average distance from the droplet center to the channel wall is 91.25 μm, causing the droplet to move into the collection channel. At this voltage, the droplet's trajectory is also more stable, with a standard deviation of 5.69 μm after passing through the electrodes. This finding indicates that the change in droplet motion during sorting is minimal. However, at voltages of 111 V and above, the droplets are overly affected by the electric force, leading to deformation and making their trajectories difficult to control. As the voltage applied to the electrodes increases from 111 V to 171 V, the trajectory of the droplets in the electrode region becomes unstable, causing them to deviate from the desired path for effective classification (Figure 4.35 (d)). This phenomenon occurs when the droplets are significantly deformed and unstable; however, the electric field strength is insufficient to cause separation, causing the droplets to move in an unpredictable direction. Further increasing the voltage leads to a stronger electric field, thereby increasing the deformation of the droplets. The degree of droplet deformation is an important factor that affects the trajectory of the droplets as they move through this non-uniform electric field region.

The result of droplet separation into two parts by DEP force

Drop deformation is studied as it passes through electrodes under high voltage conditions, using drops with a diameter of 100 μm in a channel 300 μm wide (Figure 4.36). The droplet spacing parameters, illustrated in Figure 4.36 (a), become apparent when the droplet is placed between two electrodes. Under the influence of the electric field force, the shape of the droplet changes to an ellipse as it is pulled toward the two ends of the electrodes. This deformation is primarily governed by the voltage applied to the

electrodes. Under normal conditions, the droplet maintains a spherical shape with equal diameters in the vertical (d_1) and horizontal (d_2) directions. However, when it passes through electrodes with lower voltage, the droplet deforms, and at higher voltage, it stretches to its maximum extent and forms two new droplets.

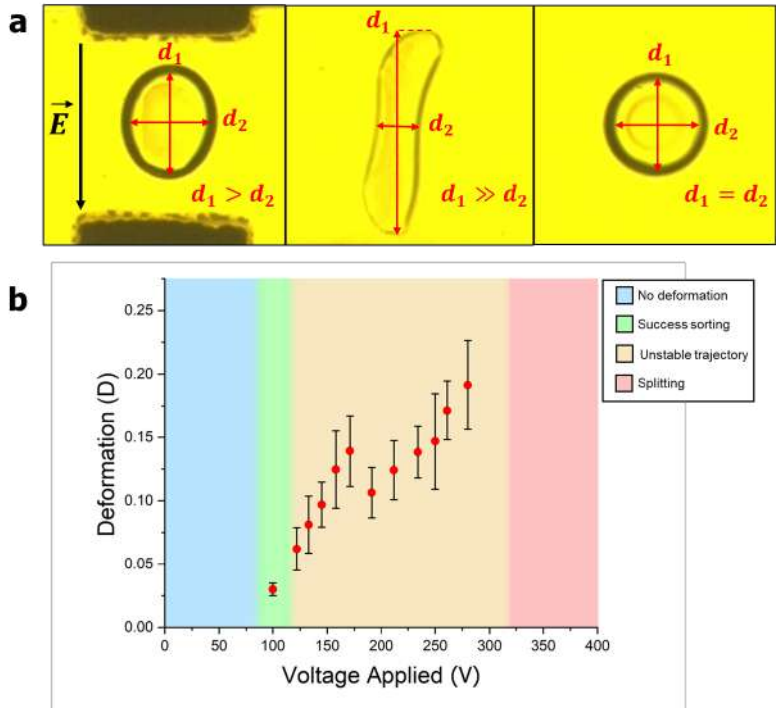

Figure 4.36: (a) Experimental image illustrating the deformation of an EHD droplet under the influence of a DC electric field. The dimensions d_1 and d_2 represent the vertical and horizontal dimensions of the deformed droplet. (b) A graph describing the droplet deformation ratio D, showing the relative elongation and contraction of the vertical and horizontal dimensions of the droplet under different voltages.

Figure 4.36 (b) illustrates the deformation of the water droplet under different voltage levels applied to the electrodes. Deformation is quantified based on the vertical ($d_{(1}$)) and horizontal (d_2) dimensions of the water droplet, measured using ImageJ software as follows:

$$D = \frac{d_1 - d_2}{d_1 + d_2} \tag{4.10}$$

At voltages ranging from 0 V to below 70 V, droplet deformation is negligible and the electric driving force (DEP) is insufficient to effectively control the droplet, resulting in low sorting efficiency. As the voltage increases to approximately 92 V to 112 V, sorting efficiency reaches its peak. Within this range, droplet deformation becomes noticeable but remains controllable, ensuring a stable and predictable droplet trajectory. As the voltage continues to increase to below 320 V, the increased deformation begins to significantly affect the droplet's trajectory, causing instability in its control behavior within the channel. The higher the voltage, the greater the observed deformation. When the voltage

exceeds the critical threshold of 320 V, droplet splitting occurs. This phenomenon is due to the combined effect of strong deformation and shear forces exerted by the liquid flow, ultimately leading to the formation of two daughter droplets. With higher stress in the electric field created by the electrodes, droplet deformation occurs earlier (Figure 4.37) than at lower voltage levels. The droplet stress caused by deformation is more significant both vertically and horizontally as the droplets approach the center of the two large symmetrical electrodes. The observed deformation phenomenon results from the combined forces within the microchannel, including Maxwell stress, continuous flow resistance, and electric force. When the total force exceeds the surface tension of the droplet, the initial droplet breaks into two daughter droplets. From the moment the droplet begins to approach the sorting electrode region (0 ms to 60 ms), the parent droplet tends to move toward the negative electrode due to the influence of the non-uniform electric field created by the proposed operating electrode structure. At 90 ms, the parent droplet enters the electric field region created by the sorting electrode pair, where the high electric field intensity initiates droplet deformation. The large electrodes allow the parent droplet to remain under the influence of the electric field long enough for deformation to lead to separation into two daughter droplets (Figure 4.37, inset image from 120 ms to 180 ms).

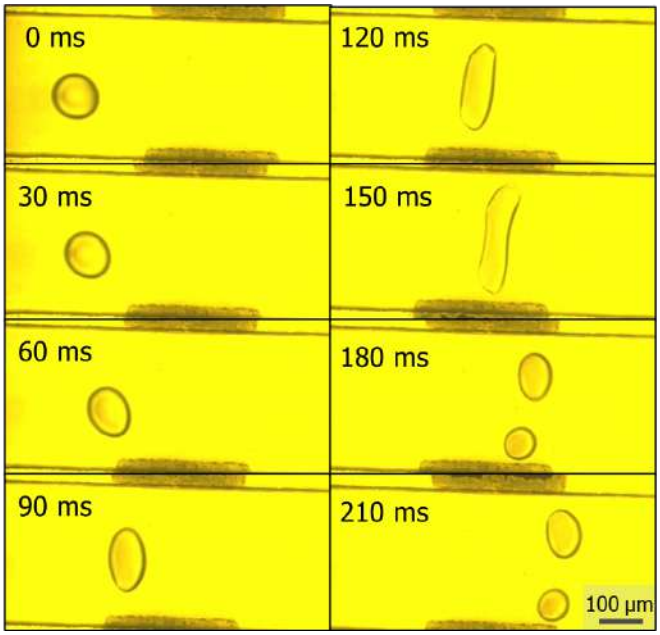

Figure 4.37: Time-lapse images showing EHD deformation and droplet separation in the electrode classification zone at a flow rate of 300 μL/h and a voltage of 320 V.

The performance of the proposed microfluidic device for droplet classification and separation is influenced by several experimental parameters, including electrode configuration, electrode size, flow rate, and droplet size, among others. Detailed investigation of these parameters could significantly enhance the applicability of this device in droplet classification and separation processes. In this study, the main channel has a width of

300 µm, and two outputs are integrated to evaluate the classification performance of each droplet. The optimal voltage range for effective classification was found to be relatively narrow; outside this range, the trajectory of the droplets became unpredictable. To expand this effective voltage range, adjustments such as increasing the size of the main channel and adjusting the voltage difference between the small and large electrodes could be explored. These adjustments could extend the device's functionality from single-drop classification to multi-drop classification across multiple outputs. Similarly, for droplet classification, the current setting leads to unequal sizes of the droplet fragments, and their subsequent trajectories remain undefined and uncontrolled. By continuing to study the voltage and flow rate applied to optimize the shear force, the size ratio of the droplets can be precisely controlled, enhancing the usefulness of droplet separation for applications requiring adjusted droplet flow rates. Future studies focusing on optimizing the experimental parameters of the proposed method are expected to yield significant advances in its application for lab-on-a-chip systems.

4.4 Summary of Chapter 4

This chapter has presented a comprehensive set of modeling and experimental results that collectively validate the operation of the proposed multifunctional Lab-on-a-Chip (LoC) platform. Numerical simulations clarified the roles of magnetic, hydrodynamic, and electrohydrodynamic forces in the magnetic filtration cavities, impedance sensing region, and DEP-based droplet manipulation zone, guiding the selection of geometrical parameters and operating windows for high-efficiency separation, sensing, and droplet control.

Experimentally, the aptamer–magnetic bead strategy achieved robust binding of A549 cells and high effective capture and purity in the microfluidic filtration module, while image-based machine learning models enabled accurate quantitative assessment of bead coverage and separation performance. In the droplet module, controlled T-junction generation produced size-tunable droplets with a high probability of single-cell encapsulation, and YOLO-based object detection provided reliable bead and cell counting inside droplets. To overcome the throughput limitations of purely optical methods, an integrated impedance cytometry module was developed, demonstrating stable real-time counting of A549 and MRC5 cells with high accuracy and clear discrimination in peak amplitude and SNR, which was further enhanced by dedicated machine learning classifiers.

Finally, DEP-based droplet steering and controlled splitting in the output section achieved near-perfect sorting efficiency within a well-defined voltage window and enabled voltage-dependent partitioning of droplets into daughter droplets. Taken together, these results confirm that the proposed LoC system can selectively capture target cells, encapsulate them into droplets, route and split droplets on demand, and perform high-throughput

electrical counting and classification on-chip. These successful validations are consistent with and have been disseminated in the candidate's peer-reviewed works [P1], [P2], [P3], [P4], [P5], and [P6].

Conclusions and Future Work

This dissertation has presented a comprehensive study on the development of a microfluidic system for the isolation and analysis of Circulating Tumor Cells (CTCs). A novel microfluidic device integrating advanced separation techniques was successfully designed and fabricated. The system demonstrated high efficiency in isolating CTCs from blood samples, achieving high recovery rates and purity.

Numerical simulations provided valuable insights into the particle behavior within the microfluidic channels, validating the experimental results. The proposed method offers a label-free and low-cost alternative to existing commercial systems, making it suitable for potential clinical applications.

The main contributions of this dissertation can be summarized as follows:

1. A multifunctional microfluidic Lab-on-a-Chip system was integrated and successfully fabricated for the detection and counting of lung cancer cells. This platform incorporates magnetically assisted and inertial microfluidic separation, droplet-based single-cell encapsulation, impedance-based cell counting, and machine-learning-based signal processing, enabling automated, high-throughput analysis on a single chip.

2. New methods for cell detection, classification, and separation were proposed and experimentally validated, based on the combined use of electromagnetic techniques and image processing with machine learning models. These methods harness magnetic forces, non-uniform electric fields, impedance cytometry, and deep-learning-based image analysis to improve the sensitivity, selectivity, and reliability of lung cancer cell analysis.

While the results obtained in this study are promising, there are several avenues for future research to further improve the system and expand its applications. First, further optimization of the channel geometry and electrode configuration could enhance the throughput and sensitivity of the system.

Second, large-scale clinical trials with patient samples are necessary to validate the clinical utility of the device for cancer diagnosis and prognosis. Third, integrating the isolation module with downstream analysis capabilities, such as single-cell sequencing or drug screening, would provide a more comprehensive tool for cancer research. Finally,

developing a fully automated and portable version of the system would facilitate its use in point-of-care settings.

References

[1] H. Sung et al., "Global cancer statistics 2020: Globocan estimates of incidence and mortality worldwide for 36 cancers in 185 countries," *CA: A Cancer Journal for Clinicians*, vol. 71, no. 3, pp. 209–249, 2021. DOI: 10.3322/caac.21660

[2] F. Bray et al., "Global cancer statistics 2022: Globocan estimates of incidence and mortality worldwide for 36 cancers in 185 countries," *CA: A Cancer Journal for Clinicians*, vol. 74, no. 3, pp. 229–263, 2024. DOI: 10.3322/caac.21834

[3] M. Cristofanilli et al., "Circulating tumor cells, disease progression, and survival in metastatic breast cancer," *New England Journal of Medicine*, vol. 351, no. 8, pp. 781–791, 2004. DOI: 10.1056/NEJMoa040766

[4] S. Nagrath et al., "Isolation of rare circulating tumour cells in cancer patients by microchip technology," *Nature*, vol. 450, no. 7173, pp. 1235–1239, 2007. DOI: 10.1038/nature06385

[5] IARC, *Globocan 2020 vietnam*, 2020.

[6] K. Pantel and C. Alix-Panabières, "Liquid biopsy and minimal residual disease — latest advances and implications for cure," *Nature Reviews Clinical Oncology*, vol. 16, pp. 409–424, 2019. DOI: 10.1038/s41571-019-0187-3

[7] Z. Zhao, L. Xu, X. Shi, W. Tan, X. Fang, and D. Shangguan, "Recognition of subtype non-small cell lung cancer by dna aptamers selected from living cells," *Analyst*, vol. 134, no. 9, pp. 1808–1814, 2009. DOI: 10.1039/b907534g

[8] T. R. Ashworth, "A case of cancer in which cells similar to those in the tumours were seen in the blood after death," *Australian Medical Journal*, vol. 14, pp. 146–147, 1869.

[9] Y. Chen et al., "Rare cell isolation and analysis in microfluidics," *Lab on a Chip*, vol. 14, no. 4, pp. 626–645, 2014. DOI: 10.1039/C3LC50989A

[10] C. W. Shields, C. D. Reyes, and G. P. López, "Microfluidic cell sorting: A review of the advances in the separation of cells from debulking to rare cell isolation," *Lab on a Chip*, vol. 15, no. 5, pp. 1230–1249, 2015. DOI: 10.1039/C4LC01246A

[11] J. M. Jackson, M. A. Witek, J. W. Kamande, and S. A. Soper, "Materials and microfluidics: Enabling the next generation of healthcare devices," *ACS Nano*, vol. 8, no. 4, pp. 3084–3091, 2014. DOI: 10.1021/nn502087u

[12] S. Riethdorf, L. O'Flaherty, C. Hille, and K. Pantel, "Clinical applications of the cellsearch platform in cancer patients," *Advanced Drug Delivery Reviews*, vol. 125, pp. 102–121, 2018. DOI: 10.1016/j.addr.2018.01.011

[13] M. E. Warkiani et al., "Ultra-fast, label-free isolation of circulating tumor cells from blood using spiral microfluidics," *Nature Protocols*, vol. 11, no. 1, pp. 134–148, 2016. DOI: 10.1038/nprot.2016.003

[14] C. Lei and et al., "High-throughput imaging flow cytometry by optofluidic time-stretch microscopy," *Nature Protocols*, vol. 13, no. 7, 2018. DOI: 10.1038/s41596-018-0008-7

[15] S. L. Stott et al., "Isolation of circulating tumor cells using a microvortex-generating herringbone-chip," *Proceedings of the National Academy of Sciences*, vol. 107, no. 43, pp. 18 392–18 397, 2010. DOI: 10.1073/pnas.1012539107

[16] W. Sheng, T. Chen, W. Tan, and Z. H. Fan, "Multivalent dna nanospheres for enhanced capture of cancer cells in microfluidic devices," *ACS Nano*, vol. 7, no. 8, pp. 7067–7076, 2013. DOI: 10.1021/nn4023747

[17] D. Shangguan et al., "Aptamers evolved from live cells as effective molecular probes for cancer study," *Proceedings of the National Academy of Sciences*, vol. 103, no. 32, pp. 11 838–11 843, 2006. DOI: 10.1073/pnas.0602615103

[18] Y. Wan et al., "Capture, isolation and release of cancer cells with aptamer-functionalized glass beads," *Lab on a Chip*, vol. 12, no. 22, pp. 4693–4701, 2012. DOI: 10.1039/C2LC40514A

[19] S. Kim and et al., "Aptamer-conjugated magnetic beads for efficient capture of circulating tumor cells," *Sensors and Actuators B: Chemical*, vol. 288, pp. 721–729, 2019.

[20] S. Miltenyi, W. Müller, W. Weichel, and A. Radbruch, "High gradient magnetic cell separation with macs," *Cytometry*, vol. 11, no. 2, pp. 231–238, 1990. DOI: 10.1002/cyto.990110203

[21] B. D. Plouffe, S. K. Murthy, and L. H. Lewis, "Fundamentals and application of magnetic particles in cell isolation and enrichment," *Reports on Progress in Physics*, vol. 78, no. 1, p. 016 601, 2015. DOI: 10.1088/0034-4885/78/1/016601

[22] K. H. Han and A. B. Frazier, "Continuous magnetophoretic separation of blood cells in microdevice format," *Journal of Applied Physics*, vol. 96, no. 10, pp. 5797–5802, 2004. DOI: 10.1063/1.1803628

[23] Z. Çağlayan, Y. D. Yalçın, and H. Külah, "A prominent cell manipulation technique in biomems: Dielectrophoresis," *Micromachines*, vol. 11, no. 11, p. 990, 2020. DOI: 10.3390/mi11110990

[24] K. Ahn, C. Kerbage, T. P. Hunt, R. M. Westervelt, D. R. Link, and D. A. Weitz, "Dielectrophoretic manipulation of drops for high-speed microfluidic sorting devices," *Applied Physics Letters*, vol. 88, no. 2, p. 024 104, 2006. DOI: 10.1063/1.2164911

[25] D. R. Link et al., "Electric control of droplets in microfluidic devices," *Angewandte Chemie International Edition*, vol. 45, no. 16, pp. 2556–2560, 2006. DOI: 10.1002/anie.200503540

[26] L. Mazutis, J. Gilbert, W. L. Ung, D. A. Weitz, A. D. Griffiths, and J. A. Heyman, "Single-cell analysis and sorting using droplet-based microfluidics," *Nature Protocols*, vol. 8, no. 5, pp. 870–891, 2013. DOI: 10.1038/nprot.2013.046

[27] D. J. Collins, A. Neild, A. deMello, A. Q. Liu, and Y. Ai, "The poisson distribution and beyond: Methods for microfluidic droplet production and single cell encapsulation," *Lab on a Chip*, vol. 15, no. 17, pp. 3439–3459, 2015. DOI: 10.1039/C5LC00614G

[28] D. Di Carlo, D. Irimia, R. G. Tompkins, and M. Toner, "Continuous inertial focusing, ordering, and separation of particles in microchannels," *Proceedings of the National Academy of Sciences*, vol. 104, no. 48, pp. 18 892–18 897, 2007. DOI: 10.1073/pnas.0704958104

[29] J. Zhang et al., "Fundamentals and applications of inertial microfluidics: A review," *Lab on a Chip*, vol. 16, no. 1, pp. 10–34, 2016. DOI: 10.1039/C5LC01159K

[30] K. Zhang et al., "Hand-held and integrated single-cell pipettes," *Journal of the American Chemical Society*, vol. 136, no. 31, pp. 10 858–10 861, 2014. DOI: 10.1021/ja5053279

[31] L. Wang and D. S. Dandy, "High-throughput inertial focusing of micrometer- and sub-micrometer-sized particles separation," *Advanced Science*, vol. 4, p. 1 700 153, 2017.

[32] S. Gawad, L. Schild, and P. Renaud, "Micromachined impedance spectroscopy flow cytometer for cell analysis and particle sizing," *Lab on a Chip*, vol. 1, no. 1, pp. 76–82, 2001. DOI: 10.1039/b103933b

[33] T. Sun and H. Morgan, "Single-cell microfluidic impedance cytometry: A review," *Microfluidics and Nanofluidics*, vol. 8, no. 4, pp. 423–443, 2010. DOI: 10.1007/s10404-010-0580-9

[34] C. Honrado, P. Bisegna, N. S. Swami, and F. Caselli, "Single-cell microfluidic impedance cytometry: From raw signals to cell phenotypes using data analytics," *Lab on a Chip*, vol. 21, no. 1, pp. 22–54, 2021. DOI: 10.1039/d0lc00840k

[35] K. C. Cheung et al., "Microfluidic impedance-based flow cytometry," *Cytometry Part A*, vol. 77, no. 7, pp. 648–666, 2010. DOI: 10.1002/cyto.a.20910

[36] C. Petchakup, K. Li, and H. Hou, "Advances in single cell impedance cytometry for biomedical applications," *Micromachines*, vol. 8, no. 3, p. 87, 2017. DOI: 10.3390/mi8030087

[37] D. Spencer, G. Elliott, and H. Morgan, "A label-free impedance-based microcytometer for high-throughput analysis of hematologic cells," *Cytometry Part A*, vol. 89, no. 11, pp. 978–988, 2016. DOI: 10.1002/cyto.a.22935

[38] H. E. Ayliffe, A. B. Frazier, and R. D. Rabbitt, "Electric impedance spectroscopy using microchannels with integrated metal electrodes," *Journal of Microelectromechanical Systems*, vol. 8, no. 1, pp. 50–57, 1999. DOI: 10.1109/84.749402

[39] R. Rodriguez-Trujillo, O. Castillo-Fernandez, M. Garrido, M. Arundell, A. Valencia, and G. Gomila, "High-speed particle detection in a micro-coulter counter with two-dimensional adjustable aperture," *Biosensors and Bioelectronics*, vol. 24, no. 2, pp. 290–296, 2008. DOI: 10.1016/j.bios.2008.04.005

[40] S. Gawad, K. Cheung, U. Seger, A. Bertsch, and P. Renaud, "Dielectric spectroscopy in a micromachined flow cytometer: Theoretical and practical considerations," *Lab on a Chip*, vol. 4, no. 3, 2004. DOI: 10.1039/b313761a

[41] C. Küttel and et al., "Label-free detection of babesia bovis infected red blood cells using impedance spectroscopy on a microfabricated flow cytometer," *Acta Tropica*, vol. 102, no. 1, pp. 63–68, 2007. DOI: 10.1016/j.actatropica.2007.03.002

[42] C. Iliescu, D. P. Poenar, M. Carp, and F. C. Loe, "A microfluidic device for impedance spectroscopy analysis of biological samples," *Sensors and Actuators B: Chemical*, vol. 123, no. 1, pp. 168–176, 2007. DOI: 10.1016/j.snb.2006.08.009

[43] G. Benazzi, D. Holmes, T. Sun, M. C. Mowlem, and H. Morgan, "Discrimination and analysis of phytoplankton using a microfluidic cytometer," *IET Nanobiotechnology*, vol. 1, no. 6, p. 94, 2007. DOI: 10.1049/iet-nbt:20070020

[44] Z. Zhu and et al., "Using microfluidic impedance cytometry to measure c. elegans worms and identify their developmental stages," *Sensors and Actuators B: Chemical*, vol. 275, 2018. DOI: 10.1016/j.snb.2018.07.169

[45] J. Panwar and R. Roy, "Integrated field's metal microelectrodes based microfluidic impedance cytometry for cell-in-droplet quantification," *Microelectronics Engineering*, vol. 215, 2019. DOI: 10.1016/j.mee.2019.111010

[46] H. Mikami and et al., "Virtual-freezing fluorescence imaging flow cytometry," *Nature Communications*, vol. 11, no. 1, 2020. DOI: 10.1038/s41467-020-14929-2

[47] H. Kobayashi and et al., "Intelligent whole-blood imaging flow cytometry for simple, rapid, and cost-effective drug-susceptibility testing of leukemia," *Lab on a Chip*, vol. 19, no. 16, 2019. DOI: 10.1039/c8lc01370e

[48] Y. Zhou and et al., "Intelligent classification of platelet aggregates by agonist type," *eLife*, vol. 9, 2020. DOI: 10.7554/eLife.52938

[49] Y. Zhang and et al., "Recent advances in aptamer-based biosensors for detection of cancer biomarkers," *Biosensors*, vol. 12, p. 123, 2022.

[50] X. Fang and W. Tan, "Aptamers generated from cell-selex for molecular medicine: A chemical biology approach," *Accounts of Chemical Research*, vol. 43, no. 1, pp. 48–57, 2010. DOI: 10.1021/ar900101s

[51] C. Tuerk and L. Gold, "Systematic evolution of ligands by exponential enrichment: Rna ligands to bacteriophage t4 dna polymerase," *Science*, vol. 249, no. 4968, pp. 505–510, 1990. DOI: 10.1126/science.2200121

[52] A. D. Ellington and J. W. Szostak, "In vitro selection of rna molecules that bind specific ligands," *Nature*, vol. 346, no. 6287, pp. 818–822, 1990. DOI: 10.1038/346818a0

[53] Y. Song et al., "Selection of dna aptamers against epithelial cell adhesion molecule for cancer cell imaging and circulating tumor cell capture," *Analytical Chemistry*, vol. 85, no. 8, pp. 4141–4149, 2013. DOI: 10.1021/ac400366b

[54] T. C. Su, H. Vu-Dinh, S. H. Lin, L. Do Quang, T. Chu Duc, and C. P. Jen, "The effect of magnetic bead size on the isolation efficiency of lung cancer cells in a serpentine microchannel with added cavities," *Biomedical Microdevices*, 2024.

[55] Q. Vu-Dinh and et al., "Immunomagnetic separation in a novel cavity-added serpentine microchannel structure for the selective isolation of lung adenocarcinoma cells," *Biomedical Microdevices*, vol. 23, no. 4, p. 51, 2021. DOI: 10.1007/s10544-021-00589-6

[56] N. Pamme, "Magnetism and microfluidics," *Lab on a Chip*, vol. 6, no. 1, pp. 24–38, 2006. DOI: 10.1039/B513005K

[57] M. A. M. Gijs, F. Lacharme, and U. Lehmann, "Microfluidic applications of magnetic particles for biological analysis and catalysis," *Chemical Reviews*, vol. 110, no. 3, pp. 1518–1563, 2010. DOI: 10.1021/cr9001929

[58] M. Zborowski and J. J. Chalmers, "Rare cell separation and analysis by magnetic sorting," *Analytical Chemistry*, vol. 83, no. 21, pp. 8050–8056, 2011. DOI: 10.1021/ac200550d

[59] K. Hoshino et al., "Microchip-based immunomagnetic detection of circulating tumor cells," *Lab on a Chip*, vol. 11, no. 20, pp. 3449–3457, 2011. DOI: 10.1039/C1LC20270G

[60] C. Liu, C. Xue, J. Sun, and G. Q. Hu, "A generalized formula for inertial lift on a sphere in microchannels," *Lab on a Chip*, vol. 16, pp. 884–892, 2016.

[61] P. Paiè, F. Bragheri, D. Di Carlo, and R. Osellame, "Particle focusing by 3d inertial microfluidics," *Microsystems & Nanoengineering*, vol. 3, pp. 1–8, 2017. DOI: 10.1038/micronano.2017.27

[62] D. Di Carlo, "Inertial microfluidics," *Lab on a Chip*, vol. 9, no. 21, pp. 3038–3046, 2009. DOI: 10.1039/B912547G

[63] J. M. Martel and M. Toner, "Inertial focusing in microfluidics," *Annual Review of Biomedical Engineering*, vol. 16, pp. 371–396, 2014. DOI: 10.1146/annurev-bioeng-121813-120704

[64] A. A. S. Bhagat, S. S. Kuntaegowdanahalli, and I. Papautsky, "Continuous particle separation in spiral microchannels using dean flows and differential migration," *Lab on a Chip*, vol. 8, no. 11, pp. 1906–1914, 2008. DOI: 10.1039/B807107A

[65] S. S. Kuntaegowdanahalli, A. A. S. Bhagat, G. Kumar, and I. Papautsky, "Inertial microfluidics for continuous particle separation in spiral microchannels," *Lab on a Chip*, vol. 9, no. 20, pp. 2973–2980, 2009. DOI: 10.1039/B908271A

[66] S. Y. Teh, R. Lin, L. H. Hung, and A. P. Lee, "Droplet microfluidics," *Lab on a Chip*, vol. 8, no. 2, pp. 198–220, 2008. DOI: 10.1039/b715524g

[67] P. Garstecki, M. J. Fuerstman, H. A. Stone, and G. M. Whitesides, "Formation of droplets and bubbles in a microfluidic t-junction—scaling and mechanism of break-up," *Lab on a Chip*, vol. 6, no. 3, pp. 437–446, 2006. DOI: 10.1039/B510841A

[68] A. R. Abate, C. H. Chen, J. J. Agresti, and D. A. Weitz, "Beating poisson encapsulation statistics using close-packed ordering," *Lab on a Chip*, vol. 9, no. 18, pp. 2628–2631, 2009. DOI: 10.1039/B909386A

[69] J. Park and et al., "Droplet microfluidics for single-cell analysis," *Analytical Chemistry*, vol. 89, pp. 1234–1245, 2017.

[70] W. H. Coulter, "High speed automatic blood cell counter and cell size analyzer," *Proceedings of the National Electronics Conference*, vol. 12, pp. 1034–1040, 1956.

[71] R. Gomez et al., "Microfluidic biochip for impedance spectroscopy of biological species," *Biomedical Microdevices*, vol. 3, pp. 201–209, 2001.

[72] D. Holmes et al., "Leukocyte analysis and differentiation using high speed microfluidic single cell impedance cytometry," *Lab on a Chip*, vol. 9, no. 20, pp. 2881–2889, 2009. DOI: 10.1039/B910053A

[73] T. Sun, D. Holmes, S. Gawad, N. G. Green, and H. Morgan, "High speed multi-frequency impedance analysis of single particles in a microfluidic cytometer using maximum length sequences," *Lab on a Chip*, vol. 7, no. 8, pp. 1034–1040, 2007. DOI: 10.1039/B703546B

[74] N. Haandbæk, S. C. Bürgel, F. Heer, and A. Hierlemann, "Characterization of subcellular morphology of single yeast cells using high frequency microfluidic impedance cytometer," *Lab on a Chip*, vol. 14, no. 2, pp. 369–377, 2014. DOI: 10.1039/C3LC50866H

[75] H. A. Pohl, "The motion and precipitation of suspensoids in divergent electric fields," *Journal of Applied Physics*, vol. 22, no. 7, pp. 869–871, 1951. DOI: 10.1063/1.1700065

[76] T. B. Jones, "Electromechanics of particles," *Cambridge University Press*, 1995, ISBN: 978-0521431965.

[77] R. Pethig, "Review article—dielectrophoresis: Status of the theory, technology, and applications," *Biomicrofluidics*, vol. 4, no. 2, p. 022 811, 2010. DOI: 10.1063/1.3456626

[78] J. C. Baret et al., "Fluorescence-activated droplet sorting (fads): Efficient microfluidic cell sorting based on enzymatic activity," *Lab on a Chip*, vol. 9, no. 13, pp. 1850–1858, 2009. DOI: 10.1039/B902504A

[79] H. D. Xi et al., "Active droplet sorting in microfluidics: A review," *Lab on a Chip*, vol. 17, no. 5, pp. 751–771, 2017. DOI: 10.1039/C6LC01435F

[80] S. K. Fan and F. M. Wang, "Multiphase optofluidics on an electro-microfluidic platform powered by electrowetting and dielectrophoresis," *Lab on a Chip*, vol. 14, no. 15, pp. 2728–2738, 2014. DOI: 10.1039/c4lc00317a

[81] R. U. Hassan, S. M. Khalil, S. A. Khan, J. Moon, D. H. Cho, and D. Byun, "Electric field and viscous fluid polarity effects on capillary-driven flow dynamics between parallel plates," *Heliyon*, vol. 9, no. 6, e16395, 2023. DOI: 10.1016/j.heliyon.2023.e16395

[82] B. J. Jung, J. Kim, J. A. Kim, H. Jang, S. Seo, and W. Lee, "Pdms-parylene hybrid, flexible microfluidics for real-time modulation of 3d helical inertial microfluidics," *Micromachines*, vol. 9, p. 255, 2018.

[83] H. A. Phan et al., "Assessment of magnetic bead conjugated lung tumor cell binding efficiency based on a deep learning approach," *2023 1st International Conference on Health Science and Technology (ICHST)*, pp. 1–4, 2023.

List of Publications Concerning the Dissertation

1. **Hoang Anh Phan**, Anh Thi Nguyen, Loc Do Quang, Tung Bui Thanh, Chun-Ping Jen, Trinh Chu Duc, "Image-based machine learning quantitative evaluation of bead-cell binding interaction", (2025), *Sensors and Actuators A: Physical*, Vol. 367, 116123. ***(Q1 Journal)***

2. **Hoang Anh Phan**, Kien Nguyen, Phong Tuan Pham, Loc Do Quang, Hang Bui Thu, Dang Bao Lam, Chun-Ping Jen, Tung Bui Thanh, Trinh Chu Duc, "On-demand electrostatic droplet sorting and splitting", (2025), *Sensors and Actuators A: Physical*, Vol. 385, 116311. ***(Q1 Journal)***

3. **Hoang Anh Phan**, Nguyen Dang Pham, Loc Quang Do, Tung Thanh Bui, Hai Hoang Nguyen, Trinh Duc Chu, "Machine learning-based bead enumeration in microfluidics droplets enhances the reliability of monitoring bead encapsulation toward single-cell sorting applications", (2024), *Microfluidics and Nanofluidics*, Vol. 28, No. 8 (Article 71). ***(Q2 Journal)***

4. **Hoang Anh Phan**, Loc Quang Do, Thanh Tung Bui, Thang Nguyen Van, Hoang Hai Nguyen, Trinh Chu Duc, "Automated detection and enumeration of bead encapsulation in microfluidic droplets based on deep learning", (2024), *International Journal of Nanotechnology*, Vol. 21, No. 7-12, 609–621. ***(Q4 Journal)***

5. **Hoang Anh Phan**, Anh Nguyen Thi, Nguyen Pham Dang, Hien Vu-Dinh, Bao Lam Dang, Tung Thanh Bui, Chun-Ping Jen, Loc Do Quang, Hai Hoang Nguyen, Trinh Chu Duc, "Magnetic Bead Conjugated Lung Tumor Cell Binding Efficiency Assessment Based on Deep-Learning Approach", (2023), *2023 1st International Conference on Health Science and Technology (ICHST)*, 1-6. ***(Scopus Conference)***

6. **Hoang Anh Phan**, Nguyen Van Phu, Tung Le Thanh, Van Tan Duong, Anh Phuc Dao, Van Dai Pham, Loc Do Quang, Thanh Tung Bui, Duc Trinh Chu, "Machine Learning-based Single-cell Analysis Using Microfluidic Impedance Flow Cytometer",

(2025), *VNU Journal of Science: Mathematics - Physics*, Vol. 41, No. 2. ***(VNU Journal)***